

INFORMATION TO USERS

This manuscript has been reproduced from the microfilm master. UMI films the text directly from the original or copy submitted. Thus, some thesis and dissertation copies are in typewriter face, while others may be from any type of computer printer.

The quality of this reproduction is dependent upon the quality of the copy submitted. Broken or indistinct print, colored or poor quality illustrations and photographs, print bleedthrough, substandard margins, and improper alignment can adversely affect reproduction.

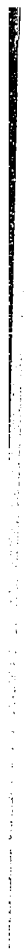
In the unlikely event that the author did not send UMI a complete manuscript and there are missing pages, these will be noted. Also, if unauthorized copyright material had to be removed, a note will indicate the deletion.

Oversize materials (e.g., maps, drawings, charts) are reproduced by sectioning the original, beginning at the upper left-hand corner and continuing from left to right in equal sections with small overlaps. Each original is also photographed in one exposure and is included in reduced form at the back of the book.

Photographs included in the original manuscript have been reproduced xerographically in this copy. Higher quality 6" x 9" black and white photographic prints are available for any photographs or illustrations appearing in this copy for an additional charge. Contact UMI directly to order.

U·M·I

University Microfilms International
A Bell & Howell Information Company
300 North Zeeb Road, Ann Arbor, MI 48106-1346 USA
313/761-4700 800/521-0600



Order Number 9416045

**Dynamic evolution of emerging magnetic flux tubes in the solar
convective envelope**

Fan, Yuhong, Ph.D.

University of Hawaii, 1993

U·M·I
300 N. Zeeb Rd.
Ann Arbor, MI 48106



**DYNAMIC EVOLUTION OF EMERGING MAGNETIC FLUX TUBES
IN THE SOLAR CONVECTIVE ENVELOPE**

**A DISSERTATION SUBMITTED TO THE GRADUATE DIVISION OF THE
UNIVERSITY OF HAWAI'I IN PARTIAL FULFILLMENT OF THE
REQUIREMENTS FOR THE DEGREE OF**

DOCTOR OF PHILOSOPHY

IN

ASTRONOMY

DECEMBER 1993

By

Yuhong Fan

Dissertation Committee:

**George H. Fisher, Chairperson
Edward E. DeLuca
Barry J. LaBonte
David C. Jewitt
David Bercovici**

This work is dedicated to my husband, Doug, and to my parents, Zhenfu Fan and Zhizhou Chen.

ACKNOWLEDGEMENTS

I undertook this dissertation topic with the encouragement of my advisor, Dr. George H. Fisher. Throughout the course of this work, Dr. Fisher has provided me with close guidance and most helpful advice. His scientific insights have on many occasions led to important breakthroughs in this research. He has patiently proofread all my manuscripts, correcting my English and giving helpful comments for improvement. It has been enjoyable and rewarding working with Dr. Fisher. Here I would like to express my sincere thanks and appreciation for the time and energy he has spent during these years.

I owe great thanks to Dr. Sandy McClymont for having offered tremendous support and invaluable scientific input to this work. With a profound understanding of physics, he has been a constant source of help and enlightenment whenever I encountered difficulties in my research.

I would like to thank Dr. Edward DeLuca who, with his wealth of knowledge in solar dynamo and fluid dynamics, has provided me with fresh ideas and insightful suggestions which propelled enormously the progress of this work.

I want to thank all members of the solar group, whom I have enjoyed working with and from whom I have received help and warm friendship during my years as a graduate student here. I am grateful to Dr. Richard Canfield who has contributed enormously to my education in solar physics. I have benefited greatly from discussions with Dr. Barry LaBonte, Dr. Charlie Lindsey and Dr. Edward Lu.

Many thanks to my fellow classmates for having offered me generous help in my graduate study as well as in life during the past few years. Special thanks to Matt Penn and Robert Ronan for providing me with the troff format of their dissertations which saved me a great deal of time in typesetting.

I sincerely thank Dave Jewitt, Jane Luu, Susan Ridgway, Robert Ronan, Reni Kupke, Pui Hin Rhoads, and many others, whose friendship have made my time here as a graduate student much more enjoyable.

I want to express my deepest gratitude to my husband Doug Braun, with whom I have shared all my frustrations and worries, joys and successes, and whose love has supported me at all times. My wholehearted thanks to Marleigh Braun, from whom I have received warm affection and encouragement. I would like to thank my parents back in China for their love, advice and support during my years of education.

Finally, I would like to acknowledge the following federal funding which have at various stages supported this work: Air Force grant AFOSR 90-0116, NSF grants ATM 9106052 and AST-9218085, NASA grants NAGW-864, NAGW-2969 and NAGW-3429.

ABSTRACT

Given the present consensus that the solar cycle dynamo is operating in a thin "overshoot layer" between the convection zone and the radiative interior, this dissertation studies the dynamics of transporting toroidal magnetic flux from the dynamo layer to the Sun's photosphere. I have carried out numerical simulations of the buoyant rise of toroidal magnetic flux tubes through the convection zone in the form of emerging loops, whose footpoints remain anchored in the overshoot layer.

My major conclusions are: 1) As each loop rises due to buoyancy, the Coriolis force transports mass out of the leading leg (leading in the direction of rotation) into the following leg of the loop, and causes the field strength in the loop's leading leg to be twice that in the following. This field strength asymmetry naturally explains the observed more compact and less fragmented morphology of the leading polarity of an active region compared to its following polarity. 2) The Coriolis force induced by the diverging east-west velocity near the apex of a rising loop acts to twist the loop, and produces a tilt angle upon emergence. For reasonable choices of toroidal field strength $3 \times 10^4 \text{ G} \leq B_0 \leq 9 \times 10^4 \text{ G}$, the computed tilt angles are consistent with the sign, magnitude and latitudinal variation of the observed active region tilt angles. The variation of the computed tilt angle α with the characteristic field strength B , latitude θ , and the total flux Φ of the loop can be described by the scaling law: $\alpha \propto \sin \theta B^{-5/4} \Phi^{1/4}$. However, for toroidal fields $B_0 \leq 2 \times 10^4 \text{ G}$, loops emerge with tilts that are opposite from those of most active regions. 3) The latitudes of loop emergence are consistent with the observed butterfly diagram

assuming a dynamo wave propagating from 30° latitude to the equator at the base of the convection zone. In the case of solid-body rotation, a toroidal field $B_0 \geq 6 \times 10^4$ G is required to avoid a significant equatorial gap, but if differential rotation is included, $B_0 \geq 3 \times 10^4$ G leads to an acceptable butterfly diagram.

TABLE OF CONTENTS

ACKNOWLEDGEMENTS	iv
ABSTRACT	vi
LIST OF FIGURES	x
CHAPTER 1. INTRODUCTION	1
1.1 The Solar Cycle and Properties of Bipolar Magnetic Regions	1
1.2 Location of the Solar Dynamo	4
1.3 The Fibril Form of Solar Magnetic Fields	9
1.4 Dynamics of Thin Flux Tubes	11
1.5 Description of this Dissertation	15
CHAPTER 2. THE ORIGIN OF MORPHOLOGICAL ASYMMETRIES	
IN BIPOLAR ACTIVE REGIONS	21
Abstract	21
2.1 Introduction	23
2.2 The Model of Thin Flux Tube Dynamics	28
2.3 Results of the Simulations	37
2.3.1 The Latitude of Flux Emergence	41
2.3.2 The Asymmetry in the Field Strength	44
2.4 Discussions and Conclusions	47
CHAPTER 3. DYNAMICS OF SINGLE EMERGING FLUX LOOPS	67
Abstract	67

3.1 Introduction	69
3.2 Description of the Numerical Simulations	72
3.3 The Critical Length Scale for Flux Emergence	77
3.4 The Latitude of Flux Emergence	82
3.5 Tilt Angles	86
3.5.1 Overview of Results from Simulations	86
3.5.2 A Simple Analysis of the Origin and Variations of Tilt	87
3.5.3 Comparison of Simple Analysis with Simulations	94
3.5.4 Comparison of Simulations with Observations	95
3.5.5 Inverse Tilts of Weak Field Strength Flux Loops	99
3.6 The Effects of Differential Rotation	100
3.7 Summary of Emerging loop Dynamics	105
CHAPTER 4. CONCLUSIONS	137
APPENDIX A: The Numerical Algorithm	146
APPENDIX B: Parallel Flow near the Loop Apex - Diverging or Converging?	149
REFERENCES	152

LIST OF FIGURES

Figure	Page
1.1 A full disk magnetogram of the Sun	18
1.2 Maunder's butterfly diagram	20
2.1 The non-axisymmetric eruption of a toroidal ring	54
2.2 The loop rise time	55
2.3 The latitude of flux emergence	57
2.4 The trajectories in the meridional plane	59
2.5 Drag force in the azimuthal direction	60
2.6 Field strength variation along the emerging loop	61
2.7 Mass distribution along the emerging loop	62
2.8 Ratio of the leading and following field strengths	63
2.9 Ratio of the perturbing and restoring forces along the emerging loop	65
2.10 Radius of the tube cross section along the emerging loop	66
3.1 The emergence of a single flux loop	108
3.2 The variation of field strength along the emerging loop	110
3.3 Evolution with $\lambda < \lambda_c$	111
3.4 The rise time of emerging loops	113
3.5 The variation of rise time with λ	115
3.6 The latitude of flux emergence	116

3.7	A comparison of emerging latitude between the multiple and single emerging loop cases	118
3.8	The dependence of the emerging latitude on the initial latitude	120
3.9	The variation of latitude along the emerging loop	122
3.10	The tilt angle of emerging loops (solid-body case)	123
3.11	The variation of v_{ϕ} along a rising loop	125
3.12	A simplified model for tension induced by tilt	126
3.13	Comparison between the scaling relation and simulations	127
3.14	Inverse tilt angles for loops with weak field strengths	129
3.15	The reversed tilting of an emerging loop with $B_0 = 10$ kG	130
3.16	The effect of differential rotation on flux loop emergence	131
3.17	A comparison of emerging latitude between differential and solid-body rotation cases	133
3.18	The tilt angle of emerging flux loops (differential rotation case)	135

CHAPTER 1

INTRODUCTION

1.1. The Solar Cycle and Properties of Bipolar Magnetic Regions

The Sun's large scale magnetic field at the photosphere (the visible surface of the Sun) is far from being a smooth dipole configuration. Looking at a full disk magnetogram (a map showing spatially the line of sight flux density of the magnetic field) of the solar photosphere (see Figure 1.1), one finds areas of concentrated magnetic flux, called *active regions*, confined to two latitudinal belts which are located nearly symmetrically on the two hemispheres. These active regions are essentially *bipolar* magnetic regions: i.e. each contains two spatial parts of opposite magnetic polarities with magnetic field lines going in and out of the photosphere respectively. The nearly east-west orientation of the axis connecting the two polarities of each active region suggests the existence of strong toroidal (east-west) magnetic fields beneath the surface.

Active regions are so named because they are usually centers of various forms of solar activity (such as solar flares) and are sites of X-ray emitting coronal loops like those seen in the soft X-ray images taken by the Yohkoh satellite. Solar activity affects the terrestrial environment by changing the solar irradiance and enhancing the input of X-rays, ultraviolet radiation, and energetic particles into the Earth's atmosphere.

An active region usually contains sunspots, and then is also called a *sunspot group*. Sunspots are dark spots seen on the solar photosphere. They are dark because they are cooler than their surroundings and coincide with the most intense concentrations of magnetic flux at the Sun's surface. A well developed sunspot has a radius of order of 10^4 km, and a flux density of about 2000 to 3000 G. Although the detailed magnetic morphology varies substantially among individual active regions, the overall behavior of active regions is remarkably organized and they share some intriguing, common features.

It was first discovered by Schwabe in 1834 that the sunspot number at the solar surface appears to oscillate with a period of about 11 years, which is therefore referred to as the *sunspot cycle* or the *solar cycle*. Later observations by Carrington and Spörer discovered that the two belts of sunspot groups or active regions on the two hemisphere migrate steadily toward the equator during each 11-year solar cycle. This phenomena is generally referred to as *Spörer's law* and is best described by the famous *butterfly diagram* first drawn by Maunder (1922), which shows the latitude distribution of sunspot groups as a function of time (see Figure 1.2). One can see from Figure 1.2 that the vast majority of sunspots occur between the equator and latitudes $\pm 35^\circ$, and that the average latitude of sunspots decreases monotonically from the beginning to the end of each solar cycle.

Further discoveries were made by Hale (1908, 1924) who proved the magnetic nature of sunspots and put forward the *Hale's polarity laws* of sunspot groups or active regions. It was found that the leading polarities (leading in the direction of

solar rotation) of nearly all active regions on one hemisphere are the same and are opposite to those on the other hemisphere (see e.g. Figure 1.1). The overall polarity orientation of active regions in each hemisphere remains unchanged during any one 11-year cycle and reverses with the beginning of the next cycle. The reversal of polarities begins with the appearance of active regions of the new cycle at mid-latitudes, while the active regions of the old cycle may still be present near the equator. The magnetic fields at the solar north and south poles are also found to reverse sign every 11 years near sunspot maximum (i.e. near the middle of a sunspot cycle). Therefore, the complete magnetic cycle, which corresponds to the interval between successive appearances at mid-latitudes of active regions with the same polarity arrangement, is in fact about 22 years.

Besides their highly organized behavior during each solar cycle, active regions are found to possess some interesting asymmetries between their leading and following polarities. Observations show that the axis connecting the leading and following polarities of each active region is nearly east-west oriented (or toroidal), but shows a small tilt relative to the east-west direction with the leading polarity of the region being slightly closer to the equator than the following. This observation of active region tilts is originally summarized in Hale et. al (1919), and is generally referred to as *Joy's law*. Another intriguing asymmetry is found in the morphology of the leading and following polarities of an active region. The flux of the leading polarity is mostly concentrated in large well-formed sunspots, whereas the flux of the following polarity tends to be more dispersed and fragmented. Furthermore, the

leading spots of an active region tend to be larger in area, fewer in numbers and have a longer lifetime than following polarity spots (e.g. Bray & Loughhead 1979, pp. 226-236).

1.2. Location of the Solar Dynamo

The cyclic behavior of the Sun's large scale magnetic field with a period of about 22 years is believed to be sustained by some kind of dynamo mechanism operating in the solar interior. Although decades of theoretical effort have been expended on the generation and maintenance of magnetic fields on the Sun, the solar cycle phenomenon remains poorly understood. An early phenomenological model of the solar cycle, which successfully described some essential features of the cycle, such as Spörer's law of sunspot latitudes, Hale's polarity laws, and the reversal of the polar fields, was put forward by Babcock (1961) and Leighton (1964, 1969). The basic picture is that a weak poloidal (north-south) magnetic field that exists below the surface at sunspot minimum is subsequently stretched and amplified into a strong toroidal magnetic field by solar differential rotation. When the strength of the toroidal magnetic field reaches some critical value, loops of toroidal magnetic flux erupt to the surface to form bipolar magnetic regions, and also dissipate the toroidal magnetic field. In the process of rising to the surface, the loops are twisted by the Coriolis force which can lead to the observed tilt angles of bipolar magnetic regions. Because of the tilt of the magnetic regions, a poloidal component of the field is generated which is opposite in direction to the original

poloidal field. Supergranular diffusion then transports the poloidal component of the erupted flux across latitudes and reverses the polar fields. The Babcock-Leighton model, although largely schematic, still holds today as a qualitative explanation of the solar cycle.

The theoretically more rigorous kinematic dynamo that can sustain an oscillatory large scale magnetic field is the *mean-field dynamo theory* initially proposed by Parker (1955) and formally developed in a series of papers by Steenbeck, Krause and Rädler (translated into English by Roberts & Stix 1971; see also reviews by Cowling 1981, and Stix 1981). A kinematic dynamo means that the velocity field is taken as given, and the reaction of magnetic stresses on the flow is neglected. Based on the mean-field dynamo model, the toroidal component of the Sun's large scale magnetic field is amplified by the action of differential rotation (called the ω -effect). The poloidal component is regenerated from the toroidal component by the averaged effect of small-scale helical motions in the convection zone, called the α -effect. The α -effect is represented quantitatively in the dynamo equation by a parameter α which depends on the lifetime and helicity of the small-scale convective motions. Thus the mean-field dynamo model for the Sun is also sometimes referred to as the α - ω dynamo. The mean-field dynamo model operating in the solar convection zone can produce periodic wave solutions (so-called *dynamo waves*) for the large scale magnetic field. The direction of dynamo wave propagation depends on the sign of $\alpha \partial\omega/\partial r$, where $\partial\omega/\partial r$ is the radial gradient of rotation rate ω . Given the sign of α in the bulk of convection

zone, which depends on the sign of helicity (i.e. the preferred sense of rotation correlated with the vertical motions of convective eddies), it is found that the dynamo waves propagate equatorward (in agreement with Spörer's law), provided that $\partial\omega/\partial r < 0$, i.e. the rotation rate increases with depth in the convection zone.

Although the kinematic mean-field dynamo model operating in the convection zone has been successful at producing the cyclic behavior of the Sun's large scale magnetic field and various essential features of the solar cycle (e.g. Spörer's law of sunspot zones, Hale's polarity laws and polar field reversals), many underlying assumptions used in the theory have been shown to be incorrect. Several recent theoretical and observational developments suggest that the solar dynamo operates not in the convection zone, but rather in a thin "overshoot layer" (with a thickness of a few tenths of a pressure scale height) between the convection zone and the radiative interior (see the review by DeLuca & Gilman 1991). There are two major reasons for this shift. First, studies of the Sun's internal rotation rate, as determined from observations of solar p-mode splittings (Brown et al 1989; Dziembowski, Goode, and Libbrecht 1989; Goode et al 1991) show that there is virtually *no* variation of rotation rate with depth in the convection zone; the surface pattern of differential rotation with latitude is apparently preserved throughout the convection zone. The radiative core, on the other hand, rotates nearly rigidly at a rate approximately equal to that at $\pm 30^\circ$ latitudes in the convection. Thus, the significant increase of rotation rate with depth, required by the mean-field dynamo model to produce the equatorward migration of toroidal magnetic field at a rate

consistent with the butterfly diagram, does not exist in the bulk of the convection zone. A way to resolve this difficulty is to place the dynamo in the thin overshoot layer at the base of the convection zone, where the temperature stratification is convectively stable, but turbulent motions are still present because of convective overshooting. The overshoot layer is a transition layer where the solar rotation changes from the latitudinal differential rotation profile of the bulk of the convection zone to solid body rotation in the radiative core. Therefore, in this layer, the rotation rate should vary steeply with depth, with the radial gradient $\partial\omega/\partial r > 0$ in low latitudes, and $\partial\omega/\partial r < 0$ in high latitudes. It is shown that the sign of α (which depends on the sign of helicity) is reversed at the base of the convection zone compared to that in the bulk of the convection zone above (Glatzmaier 1985, Gilman 1983). Thus, the mean-field dynamo model, operating in the overshoot layers, can produce equatorward migrating dynamo waves in low latitudes (roughly between $\pm 30^\circ$ latitudes) of the overshoot region, where $\partial\omega/\partial r > 0$ (see e.g. DeLuca & Gilman 1991).

The second main reason that dynamo action is unlikely to take place in the bulk of the convection zone is the magnetic buoyancy of the toroidal fields (Parker 1975, Spiegel & Weiss 1980, Moreno-Insertis 1986, Chou & Fisher 1989). Parker (1975) pointed out that the nearly east-west oriented bipolar magnetic regions at the surface of the Sun require an extensive subsurface toroidal magnetic field with field strength at least of order 10^2 G. Toroidal fields at this strength will be brought to the surface by magnetic buoyancy in a time much shorter than the solar cycle.

Furthermore, as will be discussed in §1.3, magnetic flux in the convection zone is most likely concentrated into discrete flux tubes of high field strengths (as much as 10^4 G). According to dynamic simulations (e.g. Chou & Fisher 1989), these strong flux tubes erupt to the surface on time scales of only a few months. Parker (1987a,b) suggested one possible mechanism that might help to retain toroidal flux tubes in the deep convection zone. He argued that a cold "thermal shadow" forms above the toroidal magnetic field and presses the field downward against its buoyancy. However, in order for the thermal shadow to be capable of suppressing the buoyancy of 10^4 G field, the diameter of the toroidal flux tube needs to be at least twice the pressure scale height. In an analytical calculation of the stability of toroidal flux tubes, Spruit & van Ballegoijen (1982a,b) showed that there is *no* stable configuration for a toroidal flux tube lying entirely in the convection zone. Thus, due to magnetic buoyancy, dynamo processes do not have sufficient time to operate before magnetic flux is removed from the convection zone. In contrast, because of its stable subadiabatic stratification, the overshoot region is capable of retaining a sufficient amount of magnetic flux with field strength on the order of 10^4 G for a much longer time scale (van Ballegoijen 1982).

For the above reasons, it has become widely believed that the solar dynamo mechanism operates in the thin convective overshoot layer, rather than in the bulk of the convection zone. As a result, toroidal magnetic fields generated by the dynamo process must traverse the entire convection zone before they can emerge to form the observed active regions at the photosphere. The objective of this

dissertation is to obtain a physical understanding of how magnetic flux emerges through the convection zone to the surface of the Sun, where it is observed. We intend to investigate the origin of various observed properties of active regions and to determine how the emergence of active region flux tubes varies with the conditions of the toroidal magnetic fields generated by the dynamo.

1.3. The Fibril Form of Solar Magnetic Fields

High resolution magnetograph observations have shown that solar photospheric magnetic fields are in a fibril state, i.e. in the form of discrete flux tubes of high field strength ($B \geq 10^3$ G), surrounded by nearly field free gas (e.g. Zwaan 1987, Stenflo 1989). Flux tube size scales are distributed over a wide range, varying from sunspots to very small "elementary" flux tubes. The diameter of a single flux tube can be as small as 10^2 km, and yet can still have a flux density as high as several kilogauss. Although observations of photospheric magnetic fields tell us little about the morphology of magnetic fields in the solar interior, it is generally believed that at least throughout the convection zone (and perhaps even in the overshoot layer), magnetic fields are also concentrated into thin tubes surrounded by field free plasma.

One mechanism that can concentrate magnetic flux in a turbulent conducting fluid, such as the solar convection zone, into high field strength flux tubes is a process known as "flux expulsion", i.e. magnetic fields are expelled from the interiors of convecting cells into the boundaries. This process has been studied

through both two-dimensional and three-dimensional numerical simulations of interaction between convection and magnetic fields (e.g. Galloway & Weiss 1981; Galloway & Proctor 1983; Nordlund et al. 1992). In particular, the three-dimensional simulations by Nordlund et al. (1992) strongly support the formation of magnetic flux tubes in the convection zone by flux expulsion. The magnetic flux tubes thus formed should have a field strength of the equipartition value B_{eq} , at which the magnetic pressure balances the kinetic energy density of the convective motions, i.e.

$$\frac{B_{eq}^2}{8\pi} = \frac{1}{2}\rho v^2, \quad (1.1)$$

where ρ is the density of convection zone plasma and v is the velocity of convective motions.

In addition, Parker (1984) put forward an interesting argument that supports the fibril nature of magnetic fields in the solar convection zone. He pointed out that the total energy of the atmosphere (thermal + gravitation + magnetic) is reduced by adopting a fibril state of the field which avoids the magnetic inhibition of the convective overturning. Assuming an idealized polytropic atmosphere, he was able to derive the filling factor of magnetic fields that corresponds to the minimum total energy state of the atmosphere. By applying an appropriate polytropic index for the solar convection zone, he computed the filling factor which yielded fibril magnetic fields of about 1–5 kG, roughly in agreement with the observed fibril fields at the solar surface.

Since both observational evidence and theoretical arguments support the fibril picture of solar magnetic fields, the concept of an isolated magnetic flux tube has been developed and widely used in solar magnetic field modeling (see e.g. Parker 1979a p.123). It is generally believed that the formation of active regions at the solar photosphere results from the buoyant rising of toroidal magnetic flux tubes from the base of the convection zone. Studying the dynamic evolution of magnetic flux tubes, therefore, is essential to understanding the physical process of magnetic flux transport from the dynamo layer to the surface.

1.4. Dynamics of Thin Flux Tubes

In ideal magnetohydrodynamics (MHD), a flux tube is defined as a tube of concentrated magnetic field lines, embedded in a fluid of infinite electric conductivity. The magnetic flux through any cross section of the tube remains constant and the tube is separated from the ambient un-magnetized plasma by a surface current around the tube. If the tube is *thin*, i.e., the diameter of the cross section of the tube is small in comparison with the length scale of variation along the tube, e.g. the radius of curvature of the tube and the scale height of the surrounding fluid, then one can apply the *thin flux tube approximation* (Parker 1979a p.123; Spruit 1981) to simplify the model. Under this approximation, all physical quantities inside the tube, such as field strength, pressure, density, can be averaged over the cross section of the tube so that they vary along the tube only.

The model for the dynamic evolution of thin magnetic flux tubes was formulated by Spruit (1981). Starting from the ideal MHD equations, he derived the equation of motion for a thin untwisted magnetic flux tube embedded in a non-magnetic compressible fluid in the presence of gravity. Using this model, many authors have carried out studies of the dynamic properties of magnetic flux tubes in the solar convection zone and the overshoot region, through both analytic calculations and numerical simulations.

Spruit & van Ballegoijen (1982a,b) explored analytically the instability of a thin toroidal flux tube against undulational perturbations, for various magnetic field strengths and different atmospheric temperature stratifications. They found that horizontal flux tubes in a plane parallel convection zone are unstable to perturbations with wavelengths above a certain critical value. If the curvature of stellar convective envelopes is taken into account, toroidal flux tubes will have unstable modes provided that $H/r_0 < 0.25$, where r_0 is the radius of the toroidal tubes, and H is the local pressure scale height of the surrounding plasma. For the Sun, $H/r_0 \leq 0.1$, so there are unstable modes which correspond to undulational perturbations of azimuthal order $m = 0$ through 4.

Various numerical simulations of the buoyant rising of thin magnetic flux tubes in the solar convection zone have also been carried out. Moreno-Insertis (1986) and Chou & Fisher (1989) performed two-dimensional numerical simulations to study the emergence of magnetic flux tubes in a plane parallel solar convection zone. They ignored the Coriolis force due to solar rotation so that the motion of

the rising flux tubes was confined to the vertical plane. They found that unstable eruption of flux loops occurs if the perturbation wavelength is greater than a certain critical value. The rise time is found to vary with the field strength and flux of the initial horizontal tubes: greater field strengths and larger values of flux cause a faster rising of the tube.

Simulations of the evolution of toroidal flux rings in a spherical convective envelope, with the inclusion of the Coriolis force, were first carried out by Choudhuri and collaborators (Choudhuri & Gilman 1987; Choudhuri 1989; Choudhuri & D'Silva 1990; D'Silva & Choudhuri 1991, 1993). Choudhuri & Gilman (1987) studied the axisymmetric rising (with respect to the rotation axis) of toroidal flux rings in the solar convective envelope. It was found that for field strengths at the bottom of the convection zone of order 10^5 G or less, the Coriolis force plays a dominant role in the motion of the toroidal rings. Even if the rings start out from low latitudes at the bottom, they follow a trajectory in the meridional plane that is nearly parallel to the rotation axis and emerge at latitudes significantly poleward of the observed sunspot zones.

The toroidal field strength at the bottom of the convection zone is highly uncertain and is a free parameter in the simulations. However, it is argued that the field strengths be at least the equipartition value ($\sim 10^4$ G), in order to avoid complete disruption of rising flux tubes by convection and to explain the storage of flux generated during a solar cycle in the thin overshoot layer (Zwaan 1978; Galloway & Weiss 1981; Parker 1987c; van Ballegooijen 1982). On the other

hand, values of field strength one order of magnitude higher than the equipartition value (e.g. $B > 10^5$ G) are difficult to achieve by a turbulent mean-field dynamo in the overshoot layer (DeLuca & Gilman 1986), since the Lorentz force from such high field strengths will back-react strongly on the velocity field and halt the dynamo action.

Choudhuri (1989) considered the non-axisymmetric rising of a toroidal flux ring in the form of loop structures, and found that although the innermost portions of the toroidal ring may remain anchored beneath the base of the convection zone, the upper parts of the rising loops still tend to move parallel to the rotation axis and emerge at high latitudes that are inconsistent with the sunspot zones. He therefore concluded that generalizing the simulations to include non-axisymmetries does not help to solve the problem of toroidal flux rings (with field strength less than 10^5 G) emerging at latitudes higher than the sunspot zones.

In order to resolve the problem, Choudhuri & D'Silva (1990) and D'Silva & Choudhuri (1991) examined the effects of convective turbulence and Kelvin-Helmholtz instability on the emergence of axisymmetric toroidal rings. They found that in order for these effects to suppress the Coriolis force and make flux tubes of $\sim 10^4$ G field strengths emerge radially, the radii of the tubes must be less than a few hundred kilometers. This limits the maximum flux carried by a flux tube to be on the order of 10^{19} Mx, which is much smaller than the total flux seen in a typical active region (10^{20} to 10^{22} Mx).

Recent calculations by D'Silva & Choudhuri (1993), based on the same numerical code used in Choudhuri (1989), examined the tilt angles produced by the Coriolis force acting on rising flux loops. They found that the theoretically calculated tilts match observations only if the initial magnetic field of the flux loops lies in the range between 6×10^4 G and 1.6×10^5 G. Field strengths greater than 1.6×10^5 G lead to tilt angles too small in magnitude compared to the observed values. On the other hand, field strengths smaller than 6×10^4 G result in very high latitudes of emergence and tilt angles that disobey the Joy's law (Hale et al. 1919).

1.5. Description of this Dissertation

As reviewed in §1.4, previous three-dimensional simulations of flux eruption through the convection zone have focused on the role that the Coriolis force plays in determining the latitude of flux emergence and the tilt angles. In Chapter 2 of this dissertation, we first develop a numerical model to follow the dynamic evolution of a thin, closed magnetic flux tube moving in three dimensions in the solar interior. We then apply our numerical model to simulate the three-dimensional non-axisymmetric eruption of a toroidal flux ring in the form of emerging flux loops. We investigate the effect of the Coriolis force on the evolution of other important physical quantities, such as the magnetic field strength along an emerging loop, which can have important consequences for the subsequent formation of an active region. The new results we obtain from this study (shown in Chapter 2) shed light on the origin of a long-standing observed asymmetry of

bipolar active regions: namely, that the flux of the preceding polarity of an active region is mostly concentrated in large and coherent sunspots, whereas the flux of the following polarity tends to be more dispersed and fragmented. We also find that the inclusion of the aerodynamic drag force (which is ignored in the simulations by Choudhuri 1989) can reduce the emerging latitudes of the loops.

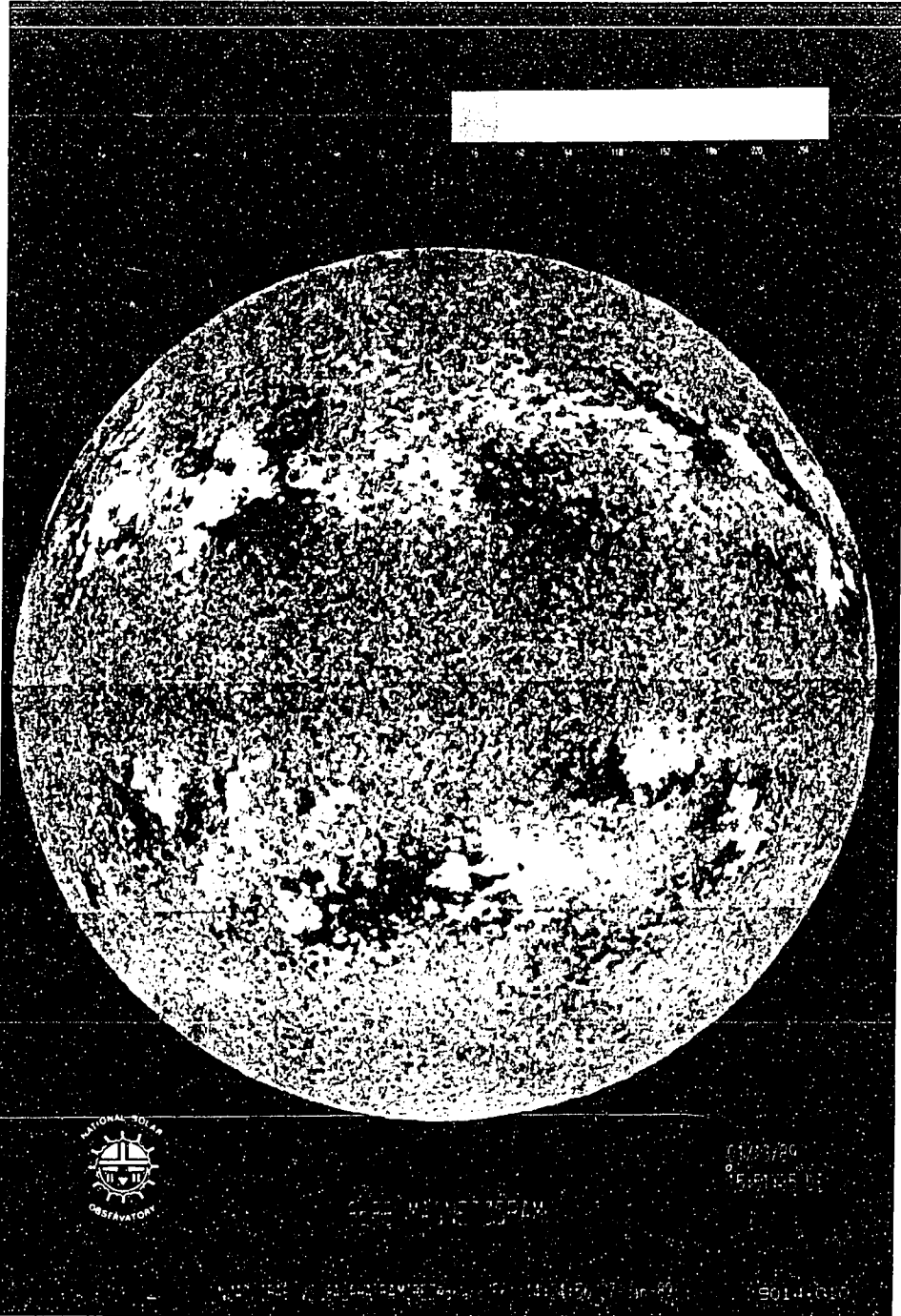
In Chapter 3, we improve the numerical model of flux emergence by modifying the eruption pattern of the initial toroidal ring. All previous simulations of flux emergence in a three-dimensional spherical geometry (e.g. Choudhuri & Gilman 1987, D'Silva & Choudhuri 1993) have assumed that the toroidal ring either rises axisymmetrically or is imposed with a periodic wave pattern so that multiple loops emerge simultaneously. Such coherent eruption patterns for the toroidal ring are very unlikely. The more plausible scenario is that only one segment of the toroidal ring is perturbed into an unstable configuration at any given time, and a single emerging flux loop arises from that segment. Thus, in Chapter 3, we carry out simulations to study the emergence of a magnetic flux loop developed from a single perturbed segment (with varying length scale) of a toroidal flux ring lying slightly beneath the base of the convection zone. From these simulations, we determine both the latitudes of emergence and the tilt angles of the loop, and compare these results with observations. We find that the latitudes of emergence obtained from these simulations of single emerging loops are significantly lower in comparison with those from simulations of multiple emerging loops or axisymmetric eruption. One important question we address is whether an

equatorward propagating dynamo wave generated by, for example, a mean-field dynamo operating in the overshoot layer (DeLuca & Gilman 1986) can lead to the observed butterfly diagram of active region latitudes at the surface through flux eruption. The answer to this question is essential for models of the overshoot layer dynamo.

Furthermore, there has been no quantitative study of the influence of solar differential rotation on the dynamics of rising flux loops. Therefore, in Chapter 3, our modeling of flux loop emergence considers both solid-body rotation and differential rotation consistent with recent results from helioseismology. A comparison between the results from these two cases quantitatively determines the effects of differential rotation on flux emergence.

Finally in Chapter 4, we summarize the conclusions of this dissertation and discuss their implications for models of the solar cycle.

Figure 1.1 A Kitt Peak full disk magnetogram showing the line of sight intensity of the photospheric magnetic field of the Sun. White color indicates field of positive (north) polarity and black indicates field of negative (south) polarity. Regions of concentrated magnetic flux, referred to as *active regions*, are confined to two azimuthal belts located nearly symmetrically on the two hemispheres. Active regions are in fact bipolar magnetic regions. It can be seen in this magnetogram that the leading polarities (leading in the direction of solar rotation) of active regions on the northern hemisphere are negative, and are opposite to those on the southern hemisphere.



© 1980 by the National Optical Astronomy Observatories, which are operated by the Association of Universities for Research in Astronomy, Inc., for the National Science Foundation.

National
Optical
Astronomy
Observatories



01/23/80
5:51:05

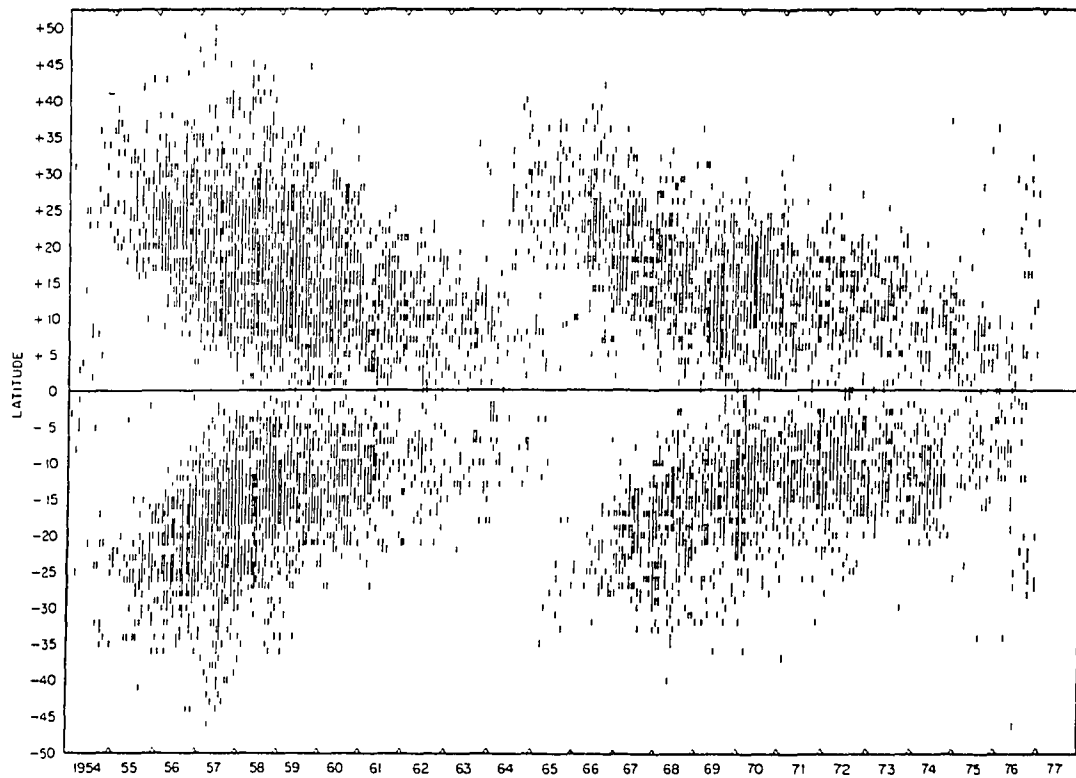


Figure 1.2 Maunder's butterfly diagram, showing the distribution of sunspot-centers in heliographic latitude as a function of time (from Priest 1982).

CHAPTER 2
THE ORIGIN OF MORPHOLOGICAL ASYMMETRIES IN
BIPOLAR ACTIVE REGIONS

Abstract

We have carried out a series of numerical simulations to study the non-axisymmetric eruption of a toroidal magnetic flux ring in the form of emerging flux loops through the solar convective envelope. The innermost portions of the loops are anchored beneath the base of the convection zone by the subadiabatic temperature gradient of the underlying overshoot region. We find that as the emerging loops approach the photosphere, the magnetic field strength of the leading side (towards the direction of rotation) of each rising loop is about twice as large as that of the following side at the same depth. This asymmetry in the field strength develops as a result of the combined action of the Coriolis force and the anchoring of the innermost portions of the emerging loops. As each loop rises, the Coriolis force induces a flow within the rising loop which evacuates plasma out of the leading side through the apex, and deposits it in the following side. The evacuation of plasma out of the leading side of the rising loop results in an enhanced magnetic field strength there compared to the following side. We argue that this result offers a natural explanation for the observed fact that the preceding (leading) polarity of an active region tends to be in the form of large well-formed sunspots, whereas the following polarity tends to have a less organized and more fragmented appearance,

and that the preceding spots tend to be larger in area, fewer in numbers and have a longer lifetime than the following spots. We also find, as a result of our simulations, that loops originally from latitudes less than 30° and with initial field strengths ranging from 3×10^4 G to 9×10^4 G, all emerge at latitudes which are consistent with the observed sunspot zones.

2.1. Introduction

It has become widely accepted that the mechanism responsible for the solar cycle dynamo probably does not operate within the bulk of the convection zone, but is concentrated in a thin “overshoot” layer between the convection zone and the radiative interior (Rosner 1980; Spiegel & Weiss 1980; Golub et al. 1981; Galloway & Weiss 1981; van Ballegoijen 1982; Schmitt & Rosner 1983; DeLuca & Gilman 1986; Gilman, Morrow, & DeLuca 1989; DeLuca & Gilman 1991). Thus the physics of transporting magnetic flux from the base of the convection zone to the surface is an important part of the solar cycle. Observations have shown that photospheric magnetic fields are in a fibril state, i.e. magnetic fields are in the form of discrete flux tubes of high field strength, surrounded by nearly field free plasma (see review by Stenflo 1989). Although these observations tell us little about the structure of subsurface magnetic fields, it is expected that magnetic fields in the convection zone are also in the form of discrete flux tubes. There are a variety of physical arguments for why this should be the case (Galloway & Weiss 1981; Galloway & Proctor 1983; Parker 1984, Schmitt & Rosner 1983, Nordlund et al. 1992). Therefore, studying the dynamics of individual magnetic flux tubes in the solar convective envelope will provide important insights into the nature of magnetic activity of the Sun.

The dynamic model of a thin magnetic flux tube was elucidated by Spruit (1981), in which the “thin flux tube approximation” was introduced. In this approximation, a flux tube can be treated as a space curve with all the physical

quantities varying only along the curve, greatly simplifying the dynamic problem. Based on this model, various numerical simulations of flux tube dynamics have been carried out.

Moreno-Insertis (1986) and Chou & Fisher (1989) carried out two-dimensional numerical simulations of the motion of a thin flux tube in a plane parallel convection zone. In their calculations, the Coriolis force due to solar rotation was ignored, so that the motion of the rising flux tube was confined to the vertical plane. They found that a magnetic flux tube with field strength $B \geq B_{eq}$ (where B_{eq} is the kinetic energy density equipartition field strength), lying originally at the bottom of the convection zone, is unstable against undulatory perturbations with perturbing wavelength larger than a critical value, and that magnetic buoyancy can bring portions of the flux tube to the surface in a time scale of months. The rise time is found to vary with field strength and total magnetic flux, with stronger fields and larger values of flux leading to faster rising of the tube.

Numerical simulations of toroidal flux rings in a rotating spherical geometry, and with the inclusion of the Coriolis force, have been described in a series of papers by Choudhuri & Gilman (1987), Choudhuri (1989), Choudhuri & D'Silva (1990), D'Silva & Choudhuri (1991,1993). With the exception of the most recent paper, which focussed on the tilt angle of active regions, the previous papers concentrated on the deflection of flux tubes by the Coriolis force to very high latitudes. Choudhuri & Gilman (1987) studied the dynamics of toroidal flux rings that are axisymmetric with respect to the rotation axis of the Sun. They found that

for field strengths at the bottom of the convection zone of 10^5 G or less, the Coriolis force deflected the flux ring to emerge at high latitudes, significantly poleward of the observed sunspot zone. The reason for this behavior is that as the circular flux ring begins expanding radially outward due to the buoyancy force, the Coriolis force, or the tendency for the ring to conserve angular momentum, induces a counter-rotating flow inside the ring. The counter-rotating flow then induces a Coriolis force directed inward towards the rotation axis. This inward Coriolis force, when combined with the radially directed buoyancy force, drives the ring to move parallel to the rotation axis. Eventually, the ring reaches the surface at a latitude poleward of the sunspot zone. Choudhuri & Gilman (1987) also found that inclusion of the aerodynamic drag force (hereafter referred to as the drag force) does not change the latitude of emergence of the axisymmetric flux rings.

Choudhuri (1989) dropped the restriction that the toroidal flux ring be axisymmetric. He considered the three-dimensional motions of non-axisymmetric flux rings (with wave-like undulations along their circumferences) in the solar convective envelope. In his calculations, the drag force was ignored. He found that although the lower parts of the flux ring may remain anchored beneath the base of the convection zone, the upper parts of the rising loops still tend to move parallel to the rotation axis and emerge at high latitudes.

The most recent calculations by D'Silva & Choudhuri (1993), based on the same numerical model as Choudhuri (1989), showed that the latitude of emergence of the upper part of the rising loops depends on the initial field strength at the base

of the convection zone, with higher field strength loops emerging at lower latitudes. They found that when the drag force is ignored, for initial field strengths between 6×10^4 G and 1.6×10^5 G, the flux loops emerge radially, and produce tilt angles very close to the observed values as described by the "Joy's Law" (Hale et. al 1919; see also Wang & Sheeley 1989 and Howard 1991a,b). When the drag force was included, they found that drag may help suppress the Coriolis force and reduce the latitude of flux emergence. Flux loops with small magnetic fields, for which the Coriolis force overpowers magnetic buoyancy, can be made to emerge more radially by increasing the drag force. By comparing the results from their simulations with the observed active region tilt angles, they conclude that it is unlikely for the field strength of flux tubes at the base of the convection zone to be either the equipartition fields (about 10^4 G) or very strong megagauss fields.

Choudhuri & D'Silva (1990) and D'Silva & Choudhuri (1991) have examined the roles of turbulence and the Kelvin-Helmholtz instability acting on axisymmetric flux rings to curb the Coriolis force from deflecting flux tubes to high latitudes.

Thus the emphasis of previous work on flux tube dynamics has been to study the latitude of flux emergence. In this chapter, we first describe our three-dimensional numerical model of the dynamics of anchored flux loops in the solar convective envelope. We then concentrate on studying the evolution of physical quantities, such as the magnetic field strength along each rising loop, which may subsequently produce observational signatures within emerging bipolar magnetic active regions. We ignore turbulent motions within the convection zone and assume

solid body rotation of the Sun. As pointed out by van Ballegoijen (1982), the high-degree of regularity in the orientation of magnetic active regions shows that turbulent motions in the convection zone are unimportant in the dynamics of emerging flux loops. We believe that many observed regular properties associated with active regions probably originate from the large scale properties of the solar interior, such as rotation and the temperature gradient, which influence the evolution of rising flux loops. The new results we obtain with the model reveal the origin of one of the well-known asymmetries between the preceding (leading) and the following polarities of a bipolar active region; namely, that the flux of the preceding polarity is mostly concentrated in large and coherent sunspots, whereas the flux of the following polarity tends to be more dispersed and fragmented, and that the preceding spots of an active region tend to be larger in area, fewer in numbers and have a longer lifetime than the following spots (see e.g. Bray & Loughhead 1979, pp. 226-236).

The remainder of this chapter is organized as follows: The equations of flux tube dynamics used in our numerical model are derived in §2.2. Results of our simulations are presented in §2.3, followed by a discussion of these results and a summary of the conclusions in §2.4. In Appendix A, we present the details of the numerical algorithm used to solve the equations derived in §2.2.

2.2. The Model of Thin Flux Tube Dynamics

From the ideal MHD equations, Spruit (1981) formally derived the equations that govern the motion of a thin untwisted magnetic flux tube embedded in a non-magnetic compressible fluid in the presence of gravity. The rotation of the Sun was ignored in his derivations. Choudhuri (1989) extend the study to include the effect of solar rotation. Assuming the Sun rotates rigidly, he derives the equation of motion for a thin flux tube in the frame of reference of the rotating Sun:

$$\frac{d\mathbf{v}}{dt} = -2\boldsymbol{\omega} \times \mathbf{v} + \frac{\rho - \rho_e}{2\rho} \mathbf{g} + \frac{B^2}{8\pi\rho} \mathbf{k} + \left[\frac{\rho - \rho_e}{2\rho} g_l + \frac{1}{\rho} \frac{\partial}{\partial s} \left(\frac{B^2}{8\pi} \right) \right] \mathbf{l} - \frac{C_D}{2\sqrt{\pi}\Phi} \frac{\rho_e \sqrt{B}}{\rho} \mathbf{v}_l \mathbf{v}_l, \quad (2.1)$$

where $\mathbf{v} = d\mathbf{r}/dt$, \mathbf{r} is the position vector of a point on the flux tube, s is the arclength along the flux tube measured in the direction of rotation from some predefined origin to the point considered, ρ is the internal density of the flux tube, ρ_e is the density of the ambient fluid, \mathbf{g} is the gravitational acceleration, g_l is the component of \mathbf{g} that is parallel to the tube, Φ is the total magnetic flux of the tube, B is the magnetic field strength inside the flux tube, and $\boldsymbol{\omega}$ is the angular velocity of the frame corotating with the Sun. The unit tangent vector $\mathbf{l} \equiv \partial\mathbf{r}/\partial s$, and the curvature vector $\mathbf{k} \equiv \partial\mathbf{l}/\partial s = \partial^2\mathbf{r}/\partial s^2$.

The first three terms on the right hand side of equation (2.1) represent the accelerations due to, respectively, the Coriolis force, the buoyancy, and the magnetic tension. The fourth term, when combined with the parallel component (parallel to the tube) of the buoyancy term, is the net acceleration parallel to the

flux tube arising from the imbalance between the pressure gradient and gravity in the \parallel (parallel) direction. The last term is the acceleration due to the drag force, which is neglected in the calculations of Choudhuri (1989). We include this drag term in our calculations.

The drag force experienced by a unit length of a flux tube when moving with respect to the ambient static fluid is (see e.g. Batchelor 1967)

$$\mathbf{F}_D = -C_D \frac{1}{2} \rho_e \mathbf{u}_\perp \mathbf{u}_\perp d, \quad (2.2)$$

where d is the tube diameter, C_D is the drag coefficient, \mathbf{u}_\perp is the perpendicular component of the tube velocity relative to the ambient fluid, and u_\perp is the magnitude of \mathbf{u}_\perp . Thus, the drag force per unit volume of the flux tube is

$$\mathbf{f}_D = -C_D \frac{\rho_e \mathbf{u}_\perp \mathbf{u}_\perp}{\pi d/2}. \quad (2.3)$$

Since the drag force is always perpendicular to the flux tube, taking into account the added inertia due to the presence of the ambient fluid, we have the acceleration due to this force to be

$$\mathbf{a}_D = \frac{\mathbf{f}_D}{\rho + \rho_e} \approx -C_D \frac{\rho_e \mathbf{u}_\perp \mathbf{u}_\perp}{\rho \pi d} = -\frac{C_D}{2\sqrt{\pi\Phi}} \frac{\rho_e \sqrt{B} \mathbf{u}_\perp \mathbf{u}_\perp}{\rho}, \quad (2.4)$$

which leads to the last term of equation (2.1). Here we have used $d = 2(\Phi/\pi B)^{1/2}$, and the approximation, $\rho_e + \rho \approx 2\rho$, since ρ_e and ρ are nearly equal throughout the evolution of the flux tube. The value we use for the drag coefficient C_D is 1, unless otherwise stated.

An important assumption used in the thin flux tube model is the instantaneous pressure balance between the flux tube and the surrounding plasma (Spruit 1981):

$$P + \frac{B^2}{8\pi} = P_e, \quad (2.5)$$

where P is the tube internal gas pressure, $B^2/8\pi$ is the magnetic pressure, and P_e is the external pressure of the ambient plasma.

Assuming zero resistivity, the equations of continuity and induction can be combined and lead to the well-known equation

$$\frac{d}{dt} \left[\frac{\mathbf{B}}{\rho} \right] = \left[\frac{\mathbf{B}}{\rho} \cdot \nabla \right] \mathbf{v}. \quad (2.6)$$

For a thin magnetic flux tube (Spruit 1981), $\mathbf{B} = B\mathbf{l}$, therefore the above equation becomes

$$\frac{d}{dt} \left[\frac{B}{\rho} \right] = \frac{B}{\rho} \left[\frac{\partial v_l}{\partial s} - \mathbf{v} \cdot \mathbf{k} \right], \quad (2.7)$$

where $v_l = \mathbf{v} \cdot \mathbf{l}$, *i.e.* the parallel component of the velocity.

For the energy equation, we assume that there is no heat exchange between the flux tube and its surroundings, *i.e.* the gas inside the tube evolves adiabatically:

$$\frac{dS}{dt} = 0, \quad (2.8)$$

where S is the entropy per unit mass inside the flux tube. The gas inside the flux tube obeys the equation of state $P = \rho RT/\mu$, where R is the gas constant, T and μ are the temperature and the mean molecular weight of the gas inside the tube.

The validity of the adiabatic assumption is discussed in Fisher, Chou, & McClymont (1989). Adiabatic evolution is a good approximation for the type of flux tube motion we consider here, if the dynamic time scale is less than about 1 year.

Because ρ and ρ_e are nearly equal, it is better for numerical accuracy in computing the buoyancy force to follow the evolution of $\Delta\rho \equiv \rho_e - \rho$ rather than ρ itself. Obviously one can obtain the value for ρ easily from ρ_e and $\Delta\rho$ at any point.

Applying the time derivative to equation (2.5), combining it with equation (2.7), and using $dP_e/dr = -\rho_e g$, we obtain, after going through some algebra, the equations which describe the time evolution of $\Delta\rho$ and B :

$$\frac{d\Delta\rho}{dt} = \frac{\nu_r \rho_e g \left[\alpha - \frac{2p_b}{\rho} \left(\frac{d\rho_e}{dP_e} + \alpha \right) \frac{d\rho_e}{dP_e} \right] + 2p_b \left(\frac{\partial v_l}{\partial s} - \mathbf{v} \cdot \mathbf{k} \right) \left[\frac{d\rho_e}{dP_e} + \alpha \right]}{1 + \frac{2p_b}{\rho} \left[\frac{d\rho_e}{dP_e} + \alpha \right]} \quad (2.9)$$

$$\frac{dB}{dt} = B \frac{-\nu_r g \frac{\rho_e}{\rho} \left[\frac{d\rho_e}{dP_e} + \alpha \right] + \left[\frac{\partial v_l}{\partial s} - \mathbf{v} \cdot \mathbf{k} \right]}{1 + \frac{2p_b}{\rho} \left[\frac{d\rho_e}{dP_e} + \alpha \right]}, \quad (2.10)$$

where ν_r is the radial component of the velocity, $p_b = B^2/(8\pi)$, and

$$\begin{aligned} \alpha &\equiv \frac{d\rho}{dP} - \frac{d\rho_e}{dP_e} \\ &= (1 - \nabla_{ad}) \frac{\rho}{P} - (1 - \nabla) \frac{\rho_e}{P_e} \\ &\approx \frac{\rho_e}{P_e} \left[\delta + (1 - \nabla_{ad}) \left[\frac{p_b}{P_e} - \frac{\Delta\rho}{\rho_e} \right] \right], \end{aligned} \quad (2.11)$$

where we have used assumption (2.8), and the facts that $p_b \ll P_e$, $|\Delta\rho| \ll \rho_e$.

Here, $\nabla \equiv d \ln T_e / d \ln P_e$ in the external atmosphere, with T_e being the external temperature, ∇_{ad} is the value of ∇ one obtains by considering locally adiabatic

perturbation of the external atmosphere, and $\delta \equiv \nabla - \nabla_{ad}$. We assume that ∇_{ad} inside the flux tube equals the corresponding value in the external atmosphere at the same depth. In the convection zone, g , ρ_e , P_e , $d\rho_e/dP_e$, ∇ , ∇_{ad} and δ are functions of depth and can be obtained from solar interior models. In this work, we have employed the solar convection zone model developed by Spruit (1974).

For the thin overshoot layer just below the convection zone, we assume constant $\nabla_{ad} = \nabla_{ad,0}$, $\delta = -10^{-4}$ and constant gravity g_0 , where g_0 and $\nabla_{ad,0}$ are values of g and ∇_{ad} at the base of the convection zone. Thus:

$$T_e = T_{e,0} + \frac{\mu g_0 \nabla}{R} (r_0 - r), \quad (2.12)$$

$$\rho_e = \rho_{e,0} \left[1 + \frac{\rho_{e,0} \nabla g_0}{P_{e,0}} (r_0 - r) \right]^{1 - \nabla/\nabla}, \quad (2.13)$$

$$P_e = P_{e,0} \left[1 + \frac{\rho_{e,0} \nabla g_0}{P_{e,0}} (r_0 - r) \right]^{1/\nabla}, \quad (2.14)$$

where $\nabla = \nabla_{ad,0} + \delta$, and $T_{e,0}$, $\rho_{e,0}$, and $P_{e,0}$ are values of T_e , ρ_e , P_e at the bottom of the convection zone. The quantity r is the radial distance from the center of the Sun, and r_0 is the radius of the base of the convection zone (for the overshoot region, $r < r_0$).

Equations (2.1), (2.9), (2.10), plus the obvious relation:

$$\frac{d\mathbf{r}}{dt} = \mathbf{v}, \quad (2.15)$$

together determine the time evolution of variables \mathbf{r} , \mathbf{v} , $\Delta\rho$, and B , once the initial values for them are given. Since we consider closed flux rings, the boundary conditions are naturally periodic.

The time derivative d/dt is the Lagrangian time derivative. Therefore equations (2.15), (2.1), (2.9), and (2.10) govern the time evolution of quantities r , \mathbf{v} , $\Delta\rho$ and B following each Lagrangian point, or mass element. However, as time goes on, motion of the mass elements along the flux tube will change their relative distribution within the tube, leaving some portions of the flux tube under-resolved.

To solve this problem, we choose to follow the time evolution of physical quantities at mesh points that are always maintained at a uniform spacing in arclength as measured along the tube, even as the tube shape is changing. To achieve this, we need to evaluate the time derivatives following the uniformly spaced mesh points, $(\partial/\partial t)|_u$, where u describes the position of each mesh point along the tube in terms of the fractional arclength, i.e. $u \equiv s/L$, with L being the total arclength of the flux tube. Let A be any one of the variables, r , \mathbf{v} , $\Delta\rho$, B . Thus $A = A(u, t)$. Applying the Lagrangian derivative to A yields:

$$\frac{dA}{dt} = \frac{\partial A}{\partial u} \bigg|_t \frac{du}{dt} + \frac{\partial A}{\partial t} \bigg|_u. \quad (2.16)$$

Therefore,

$$\frac{\partial A}{\partial t} \bigg|_u = \frac{dA}{dt} - \frac{\partial A}{\partial u} \bigg|_t \frac{du}{dt}. \quad (2.17)$$

The left-hand side of equation (2.17) is the time derivative we seek. On the right-hand side, dA/dt is known from equations (2.15), (2.1), (2.9) and (2.10), while $\partial A/\partial u$ describes the variation of each variable A along the tube. The derivative $du/dt \equiv d(s/L)/dt$ describes the change of position of each mass element in terms of the fractional arclength along the tube. To calculate du/dt , we start from

equation (2.7). We know that $B/\rho = (\Phi/\delta m)\delta s$, where δm and δs are, respectively, the mass and the length of a single Lagrangian element, and Φ is the magnetic flux carried by the tube. Furthermore, $d\delta m/dt = 0$, and $d\Phi/dt = 0$. Thus equation (2.7) can be written as:

$$\frac{d\delta s}{dt} = \left[\frac{\partial v_l}{\partial s} - \mathbf{v} \cdot \mathbf{k} \right] \delta s. \quad (2.18)$$

Therefore,

$$\frac{ds}{dt} = \int_0^s \frac{d\delta s}{dt} = v_l(u) - v_l(0) - L \int_0^u \mathbf{v} \cdot \mathbf{k} \delta u, \quad (2.19)$$

and:

$$\frac{dL}{dt} = \int_0^L \frac{d\delta s}{dt} = v_l(1) - v_l(0) - L \int_0^1 \mathbf{v} \cdot \mathbf{k} \delta u, \quad (2.20)$$

where $\delta u \equiv \delta s/L$, $v_l(u)$ is the parallel velocity of the mass element at position of fractional arclength u along the tube, and $v_l(0)$ and $v_l(1)$ are the parallel velocities of the mass elements at the beginning ($u=0$) and the end ($u=1$) of the tube.

Knowing ds/dt and dL/dt , we can calculate du/dt :

$$\frac{du}{dt} = \frac{1}{L}(v_l(u) - v_l(0)) - \int_0^u \mathbf{v} \cdot \mathbf{k} \delta u - \frac{u}{L}(v_l(1) - v_l(0)) + u \int_0^1 \mathbf{v} \cdot \mathbf{k} \delta u. \quad (2.21)$$

Here, $v_l(0) = v_l(1)$ due to the periodic boundary conditions.

To summarize, the system of equations we solve is

$$\begin{aligned} \frac{\partial \mathbf{r}}{\partial t} \Big|_u &= \mathbf{v} - \frac{\partial \mathbf{r}}{\partial u} \Big|_t \frac{du}{dt}, \\ \frac{\partial \mathbf{v}}{\partial t} \Big|_u &= -2\boldsymbol{\omega} \times \mathbf{v} + \frac{\rho - \rho_e}{2\rho} \mathbf{g} + \left[\frac{\rho - \rho_e}{2\rho} g_l + \frac{1}{\rho} \frac{\partial}{\partial s} \left(\frac{B^2}{8\pi} \right) \right] \mathbf{l} \end{aligned} \quad (2.22)$$

$$-\frac{C_D}{2\sqrt{\pi}\Phi} \frac{\rho_e \sqrt{B} v_l v_l}{\rho} - \frac{\partial v}{\partial u} \Big|_t \frac{du}{dt}, \quad (2.23)$$

$$\frac{\partial \Delta \rho}{\partial t} \Big|_u = \frac{v_r \rho_e g \left[\alpha - \frac{2p_b}{\rho} \left(\frac{d\rho_e}{dP_e} + \alpha \right) \frac{d\rho_e}{dP_e} \right] + 2p_b \left(\frac{\partial v_l}{\partial s} - \mathbf{v} \cdot \mathbf{k} \right) \left(\frac{d\rho_e}{dP_e} + \alpha \right)}{1 + \frac{2p_b}{\rho} \left(\frac{d\rho_e}{dP_e} + \alpha \right)} - \frac{\partial \Delta \rho}{\partial u} \Big|_t \frac{du}{dt}, \quad (2.24)$$

$$\frac{\partial B}{\partial t} \Big|_u = B \frac{-v_r g \frac{\rho_e}{\rho} \left(\frac{d\rho_e}{dP_e} + \alpha \right) + \left(\frac{\partial v_l}{\partial s} - \mathbf{v} \cdot \mathbf{k} \right)}{1 + \frac{2p_b}{\rho} \left(\frac{d\rho_e}{dP_e} + \alpha \right)} - \frac{\partial B}{\partial u} \Big|_t \frac{du}{dt}, \quad (2.25)$$

where $p_b = B^2/8\pi$, and

$$\alpha = \frac{\rho_e}{P_e} \left[\delta + (1 - \nabla_{ad}) \left(\frac{p_b}{P_e} - \frac{\Delta \rho}{\rho_e} \right) \right], \quad (2.26)$$

$$\frac{du}{dt} = \frac{1}{L} (v_l(u) - v_l(0)) - \int_0^u \mathbf{v} \cdot \mathbf{k} \delta u + u \int_0^1 \mathbf{v} \cdot \mathbf{k} \delta u. \quad (2.27)$$

Thus, once the initial values for \mathbf{r} , \mathbf{v} , $\Delta \rho$, B are known at mesh points which are uniformly spaced in arclength along the tube, we will be able to follow the time evolution of the physical conditions at these uniformly spaced mesh points even as the tube shape is changing. The vector \mathbf{r} is expressed in Cartesian coordinates with the z axis coincident with the solar rotation axis, and the x , y axes lying in the equatorial plane. The numerical algorithm used to solve the equations is described in Appendix A.

We have performed several tests of the numerical model in order to test its reliability. For example, we applied the numerical code to solve for the motion of a shrinking circular flux ring in a uniform background fluid with zero gravity. In this case, the equation of motion includes only the inertial, magnetic tension and drag force terms. Since the tension force and the drag force dominate except during the very short period at the beginning when the flux ring is accelerating from zero velocity, an analytical solution for the motion of the circular ring can be obtained (Fisher, DeLuca, & Patten 1991):

$$R(t) = R_0(1 - t/\tau)^{4/3}, \quad (2.28)$$

where $R(t)$ designates the radius of the circular ring as a function of time, and $R_0 = R(t=0)$. The time scale $\tau = 4/3[C_D R_0^3 / (\pi a_0 v_{A0}^2)]^{1/2}$, where a_0 is the initial radius of the cross section of the ring, and v_{A0} is the initial Alfvén speed. We found that the result from the numerical simulation agrees very well with the analytical solution. We have also tested our numerical code by repeating flux tube dynamic simulations that have been published by other authors, such as the 2-D simulations by Moreno-Insertis (1986), and the simulations done in spherical geometry by Choudhuri & Gilman (1987) and Choudhuri (1989). We found very good agreement with the results of Moreno-Insertis (1986). Comparing our computed rise times with his for a sequence of flux tubes with $\Phi = 10^{21}$ Mx and $\Phi = 10^{22}$ Mx and a range of field strengths from 10^5 to 10^6 G, we found agreement in general to better than 10%. We obtained indistinguishable evolution of the morphology of the tube, the magnetic field strength, the density and the parallel

flow along the tube as shown in Figures 2, 4, 6, 7 of Moreno-Insertis (1986). In our comparison with the simulations done by Choudhuri & Gilman (1987) and Choudhuri (1989), we found that when we matched the assumptions, the initial and atmospheric conditions used in their calculations (to the extent that we can determine them), we found very similar morphologies of the trajectories of emergence. Finally, since our numerical code is not written in a direct mass conservative form, a further test of its accuracy is its ability to conserve mass. We have found that for 201 mesh points along the toroidal flux ring, the mass is conserved to 10^{-3} over the course of the entire simulation, which is within the truncation error expected in using the 2nd order accurate finite differences in u .

2.3. Results of the Simulations

In this section, we first describe the general features of our series of calculations of rising flux loops in the solar convective envelope. Then, in §2.3.1, we discuss the latitude of flux emergence, and in §2.3.2 we present in detail our results on the magnetic field strength asymmetry of the emerging flux loops.

The initial configurations for the toroidal flux rings we study are similar to those of Choudhuri (1989). We start with a toroidal ring located at the base of the convection zone and at an initial latitude θ_0 ranging from N 1° to N 30° . An undulational perturbation with 4 full wavelengths along the circumference of the flux ring is imposed, with the upper portions of the flux ring in the convection zone and the lower portions in the buoyantly stable overshoot region. The initial shape of

the flux ring can be described as:

$$r = r_0 + \delta r \sin(4\phi), \quad (2.29)$$

$$\theta = \theta_0, \quad (2.30)$$

with r_0 being the radius of the base of the convection zone and $\delta r = 1 \times 10^9$ cm. Initially, the flux ring is assumed to be in thermal equilibrium with its surroundings, and $\beta \equiv P_e/p_b$ is assumed uniform along the tube. Thus the plasma inside the flux ring is initially in hydrostatic equilibrium in the direction parallel to the magnetic field. The perpendicular forces however, do not balance, and the flux ring is buoyant in the initial configuration.

The choice of initial field strength and total flux is governed by the following constraints: First, observations show that photospheric active regions generally have a total flux within the range 10^{20} Mx to 10^{22} Mx. Therefore, we choose this flux range for our simulations. For the thin flux tube approximation to be satisfied, the radius of the cross section of a flux tube, a , should be at least one order of magnitude less than the pressure scale height H_p at the base of the convection zone. Thus

$$\frac{a}{H_p} \leq 0.1, \quad (2.31)$$

where $a = (\Phi/\pi B_0)^{1/2}$, and H_p is approximately 5×10^9 cm. Furthermore, as noted previously, the regular orientation of active regions suggests that motions of the flux tube should not be controlled by turbulent convective motions of the ambient fluid, or in other words, the magnetic restoring force of the flux tube should be strong compare to the drag force exerted on the flux tube by turbulent convective motions:

$$\frac{B_0^2}{4\pi R} > C_D \frac{\rho_e v_c^2}{\pi a}, \quad (2.32)$$

where v_c is the velocity of the convective motion and R is the size scale of a convective cell. We need only consider the biggest cell size (which we estimate as $R \approx H_p$), because larger cells perturb the flux tube more effectively than smaller ones. Knowing that $B_{eq}^2/8\pi = \frac{1}{2}\rho_e v_c^2$, relation (2.32) becomes:

$$\left[\frac{B_0}{B_{eq}} \right]^2 > \frac{C_D}{\pi} \frac{H_p}{a}, \quad (2.33)$$

where B_{eq} is the equipartition field strength, i.e. the field strength at which the magnetic energy density balance the kinetic energy density of the turbulent motions. In the deep convection zone, B_{eq} is approximately 3200 G. To satisfy criteria (2.31) and (2.33) simultaneously, the initial field strength B_0 should be larger than 13 kG, 9 kG and 20 kG, for $\Phi = 10^{22}$ Mx, 10^{21} Mx and 10^{20} Mx, respectively. Therefore we choose the initial field strength of our simulations to range from 30 kG to 90 kG. We choose 90 kG as an upper limit because, if the initial field strength of the flux ring is higher than 90 kG, the subadiabatic temperature gradient with $\delta = -10^{-4}$ in the overshoot region is insufficient to keep the innermost portions of the flux ring anchored beneath the base of the convection zone throughout the emerging process. Our choice of the initial latitudes for the simulations are N 1°, N 5°, N 10°, N 20° and N 30°. We concentrate on flux rings which are initially below 30° because results from helioseismology (see e.g. Dziembowski, Goode & Libbrecht 1989; Brown et al. 1989; Goode et al. 1991) indicate that at low latitudes in the overshoot region differential rotation is largest, and hence field amplification

is most effective. Furthermore, overshoot layer dynamo models which have the correct direction of dynamo wave propagation can only operate at latitudes of less than 30° (DeLuca & Gilman 1986; Gilman, Morrow, & DeLuca 1989).

Figure 2.1 shows the evolution of a toroidal flux ring with initial field strength $B_0 = 3 \times 10^4$ G, $\Phi = 10^{22}$ Mx, and initial latitude $\theta_0 = 5^\circ$ N, viewed from 30 degree above the equator. At $t_1 = 0$, the flux ring is released, and the configurations of the flux ring at 4 consecutive times t_1, t_2, t_3, t_4 , with a constant separation of approximately 32 days, are shown with solid curves. The solid curve labeled t_4 shows the final configuration of the flux ring in the simulation. The outer dotted circle marks the photosphere and the inner dotted circle represents the base of the convection zone. It can be seen that the original undulatory perturbation of the flux ring is being amplified with time due to the buoyant instability of the flux tube in the convection zone. Four periodic rising loops are formed along the circumference of the flux ring, while the innermost portions remain anchored in the overshoot region because of its stable subadiabatic stratification. The emerging latitude of the loop apexes is $N 23^\circ$. One of the four rising loops along the flux ring at t_4 is marked with crosses for its leading side (towards the direction of rotation) and squares for its following side. Note that throughout the paper, the terms “leading” and “following” sides are used with respect to the apex of each rising loop.

The rise time of the flux loops varies with the initial field strength and the total flux, as shown in Figure 2.2. Increasing the field strength increases the

magnetic buoyancy, and increasing the flux reduces the drag force per unit mass (see the last term of eq. [2.1]), both of which result in faster emergence of the flux loops. This is consistent with the conclusions from previous simulations (see e.g. Moreno-Insertis 1986, Chou & Fisher 1989).

2.3.1 *The Latitude of Flux Emergence*

Figure 2.3 shows the latitudes at which the apexes of the loops emerge. For all cases shown, the loops emerge at latitudes that are within the observed sunspot zone. We can see that the latitude of emergence decreases with increasing initial field strength B_0 , and it also decreases with decreasing flux Φ . This dependence of emerging latitude on B_0 and Φ is consistent with the result of D'Silva & Choudhuri (1993). The buoyancy force of the flux tube in the deep convection zone is estimated to be $B_0^2/8\pi H_p$ (This can be derived by assuming that the flux tube is in thermal equilibrium with the ambient fluid), where H_p is the external pressure scale height. Therefore, the magnetic buoyancy force scales as B_0^2 . On the other hand, the Coriolis force is proportional to the rising speed v_r , which can be estimated by considering the balance between the buoyancy force and the drag force:

$$\frac{B_0^2}{8\pi H_p} = C_D \frac{\rho_e v_r^2}{\pi d/2}, \quad (2.34)$$

where $d/2 = (\Phi/\pi B_0)^{1/2}$. Thus the Coriolis force scales as $B_0^{3/4}$. Therefore, as B_0 increases, the buoyancy force becomes relatively more dominant, and the effect of the Coriolis force becomes less important. The flux tube rises more radially and emerges at lower latitudes.

We also find that the drag force can reduce the latitude of flux emergence. This is also found in the recent calculations of D'Silva & Choudhuri (1993). We repeat the simulation with $B_0 = 3 \times 10^4$ G, $\Phi = 10^{22}$ Mx and $\theta_0 = 5^\circ$ N as shown in Figure 2.1, but with C_D set to zero instead of 1. Figure 2.4 displays the trajectories of the outermost and the innermost parts of the flux ring, as viewed in the meridional plane. The solid line represents the case with $C_D = 0$ and the dash dot lines represent the case with $C_D = 1$. In this case, the flux ring would emerge at N 30° if the drag force were ignored, rather than at N 23° for $C_D = 1$. In fact, the decrease of the emerging latitude of the loops with decreasing Φ shown in Figure 2.3 is due solely to the increasing importance of the drag force per unit mass (the last term on the right hand side of eq. [2.1]), which is dynamically equivalent to increasing the drag coefficient C_D ; in other words, both will give identical results in the motion of the flux tube.

The reason that the inclusion of the drag force can decrease the latitude of emergence is because the drag force transfers angular momentum to the flux ring. The z component of the torque experienced by each unit length of the flux ring due to the drag force is:

$$\begin{aligned} T_z &= \mathbf{e}_z \cdot (\mathbf{r} \times \mathbf{F}_D) \\ &= \sqrt{x^2 + y^2} F_{D\phi}, \end{aligned} \quad (2.35)$$

where \mathbf{e}_z is the unit vector in the z direction, \mathbf{F}_D is the drag force experienced by a unit length of the flux tube (see eq. [2.2]), $\sqrt{x^2 + y^2}$ is the distance from the flux tube to the rotation axis (or the z axis), and $F_{D\phi} \equiv \mathbf{e}_\phi \cdot \mathbf{F}_D$, i.e. the ϕ component of

the drag force per unit length of the flux tube. For the special case of axisymmetric flux rings discussed in Choudhuri & Gilman (1987), $F_{D\phi}$ is always zero. Therefore, the drag force does not transfer angular momentum to the flux ring, and the inclusion of the drag force does not alter the latitude of emergence of the flux ring. We have also done simulations with axisymmetric flux rings and we reach the same conclusion.

However, for the non-axisymmetric flux rings that we consider here, $F_{D\phi}$ is generally non-zero. For example, Figure 2.5 shows a snap-shot of the ϕ component of the drag force per unit length along a rising loop in the simulation with $B_0 = 3 \times 10^4$ G, $\Phi = 10^{22}$ Mx and $\theta_0 = 5^\circ$. Here only one of the four periodic rising loops along the flux ring is displayed. The solid arrows show the magnitude and the direction of the ϕ component of the drag force per unit length of the flux tube. On the following side of the loop, the drag force is pushing the loop toward the positive e_ϕ direction (or toward the direction of rotation), but on the leading side, the drag force is pushing the loop in the negative e_ϕ direction. We can see from the length of the arrows that the drag force per unit length experienced by the following side dominates that of the leading side. Therefore, the overall result of the ϕ component of the drag force along the flux ring is to push the ring in the direction of rotation, i.e. to apply a torque in the positive z direction. Because of this torque, the flux ring gains more angular momentum and emerges at a lower latitude.

2.3.2 *The Asymmetry in the Field Strength*

Figure 2.6 shows the final magnetic field strength along an emerging loop as a function of the radial distance to the center of the Sun, resulting from the simulation with initial parameters $B_0 = 3 \times 10^4 \text{ G}$, $\Phi = 10^{22} \text{ Mx}$ and $\theta_0 = 5^\circ$. The crosses and squares here correspond to those in Figure 2.1. Here we find the very interesting result that the magnetic field strength of the leading side of a rising loop is generally significantly larger than that of the following side at the same depth. The ratio of the leading side field strength to the following side field strength is about 3:1 in the middle of the convection zone, and this ratio stays basically unchanged all the way to the top of the loop. This also means that the leading side cross section is only 1/3 that of the following side.

This asymmetry of magnetic field strength can be understood qualitatively through the flow of plasma inside the flux tube during its evolution. The internal plasma flow is controlled by 1) the tendency to evolve towards hydrostatic equilibrium inside the tube and 2) the component of the Coriolis force parallel to the flux tube, attempting to preserve the initial angular momentum. Both effects are comparable in magnitude, although the latter is responsible for the development of the asymmetry between the leading and following sides of the loop. As each loop rises, the Coriolis force drives a counter-rotating flow of plasma from the leading side of the rising loop through the apex to the following side. However, the innermost portions (or the troughs) of the loop are anchored beneath the base of the convection zone and do not rise, so the flow driven by the Coriolis force is

suppressed there. While the plasma is being driven out of the leading side of the loop toward the following side through the apex, there is very little plasma flowing into the leading side through its neighboring trough. The net result is an evacuation of plasma out of the leading side and into the following side of each rising loop. This effect is clearly reflected in Figure 2.7 which shows the final mass distribution along the loop as a function of the radial distance to the center of the Sun. The mass distribution is expressed here in terms of mass per unit length, i.e. linear density. We see that the linear density of the leading side is significantly smaller than that of the following side at the same depth. When plasma is being evacuated, the leading side of the loop experiences a lower internal gas pressure than the following side at the same depth. Therefore the loop cross section of the leading side shrinks, so that the magnetic pressure increases to balance the same external pressure, i.e. $P + p_b = P_e$, resulting in a significantly stronger magnetic field strength for the leading side of the loop comparing to the following side at the same depth, as shown in Figure 2.6.

For comparison, we repeat the simulation with exactly the same conditions except that δ for the overshoot region is set to 0 instead of -10^{-4} . By doing this, we remove the anchoring of those portions of the flux ring that are initially perturbed into the overshoot region. Without anchoring, the resulting evolution of the flux ring becomes very similar to the case of axisymmetric rings studied by Choudhuri & Gilman (1987). The flux ring as a whole floats to the surface, and the emerging latitude of the outer parts of the ring is very high, about N 40°.

Furthermore, the degree of field strength asymmetry between the leading and the following side of each loop is much weaker, with the ratio of the leading field strength to the following field strength at the same depth being 1.2 at maximum, and this ratio decreases quickly to 1 for the outer part of the loop. With anchoring however, the ratio is approximately 3 all the way from the middle of the convection zone to the top of the loop as shown previously in Figure 2.6. Therefore, we believe that anchoring portions of the flux ring beneath the base of the convection zone is an essential requirement for obtaining a significant asymmetry in field strength of a rising flux loop.

Our simulations show that despite variations of the initial parameters, the asymmetric field strength is a robust result for rising flux loops whose innermost portions are anchored beneath the base of the convection zone. The final magnetic field configuration of the rising loops all show a degree of asymmetry similar to that seen in Figure 2.6, with the leading side field strength always stronger comparing to the following side at any chosen depth. For each case, we also compute B_l/B_f , where B_l and B_f are the field strengths of the leading and following sides of the loop evaluated at a depth half way between the base of the convection zone and the surface. Generally this ratio persists all the way from the middle of the convection zone to the top of the emerging loop, therefore, it is a good measure of the degree of field strength asymmetry of the loop. The result is shown in Figure 2.8. For all cases, the values of B_l/B_f are higher than 1.3 and reach a maximum of 3.7. We find that the ratio B_l/B_f decreases with increasing

field strength B_0 . The reason is similar to that for the emerging latitude decreasing with increasing B_0 discussed previously in section 3.1. As field strength increases, the buoyancy force becomes more dominant and the effect of the Coriolis force becomes less significant. The variation of B_l/B_f with flux is more complicated however. It appears that as Φ increases, B_l/B_f varies more steeply with B_0 .

We conclude from Figure 2.8 that loops, whose innermost portions are anchored beneath the base of the convection zone, develop an asymmetry in field strength as they rise to the surface, with the field strength of the leading side of each loop larger, by generally a factor of 2, than that of the following side at the same depth. We also find that this result does not rely on the choice of the drag coefficient C_D .

2.4. Discussions and Conclusions

The general picture of the formation of an active region is that a rising loop of concentrated magnetic flux breaks through the photosphere, with its leading and following tubes intersecting the surface to form the two polarities (the preceding and following polarities) of the active region (see e.g. Zwaan, 1985). Although we cannot determine the detailed evolution of the upper part of the loop breaking through the photosphere within the framework of the current simulation (due to the breakdown of many of our assumptions as the tube approaches the surface), we can still infer some properties of the subsequent emerging process and the active region formation using the knowledge of the final state of the loop in our simulations.

We have shown in §2.3.2 that due to the combined action of the Coriolis force and anchoring beneath the base of the convection zone, the loop develops a significant asymmetry in its magnetic field strength while it is rising to the surface. Upon emerging, the leading side of the loop has a field strength generally twice as strong, a cross sectional area half as large, and a linear mass density (mass per unit length) about 1/2 that of the following side at the same depth. With a greater field strength, the leading side of the loop is certainly more stable against the perturbations due to turbulent motions which lead to fragmentation of the tube.

Figure 2.9 shows the ratio of the estimated perturbing force from turbulent convective motions $F_{turb} \equiv C_D (\rho_e v_c^2 / \pi a)$ to the restoring tension force of the tube $F_{tens} \equiv B^2 / 4\pi R$, as a function of the radial distance to the center of the Sun, computed along the final emerging loop resulting from the simulation with initial parameters $B_0 = 3 \times 10^4$ G, $\Phi = 10^{22}$ Mx, and $\theta_0 = 5^\circ$. Here, ρ_e is the external density, v_c is the convective velocity estimated from the mixing length model of Spruit (1974), a is radius of the cross section of the flux tube and R is the mixing length, i.e. the characteristic cell size of convection. This ratio F_{turb} / F_{tens} describes the degree of deformation of the flux tube by the convective turbulent motions. We can see that this ratio for the leading side of the loop is much smaller compared to the following side throughout the convection zone. Therefore the leading side is much less affected by the turbulent motion than the following side. At about 0.98 solar radius, or approximately 1.4×10^9 cm below the surface, the ratio for the following side increases significantly to above 0.6, which means that F_{turb} starts to

become comparable to F_{tens} . Thus the following side of the loop starts to become vulnerable to deformation by turbulent motion above this depth.

Figure 2.10 shows the radius of the cross section of the tube a in comparison with the convective cell size R . Above 0.96 solar radius, a becomes larger than the convective cell size. If the size scale of the perturbing cell is smaller than the cross sectional radius of the tube, and at the same time, F_{turb} is comparable to or bigger than F_{tens} , the turbulent motions will most likely shear the flux tube and cause it to fragment.

According to this picture, the following side of the loop will fragment much more severely compared to the leading side. As an extreme case, the leading side may very possibly survive the turbulent motions and intersect the photosphere as a large single flux tube which encloses all the flux of the preceding polarity. The following side, on the contrary, branches into numerous smaller tubes which intersect the photosphere, with convective motions penetrating into the field free area between these tubes.

As the tubes intersect the photosphere, radiative cooling of plasma within each tube becomes very efficient. Convective heat transport is prohibited by the magnetic field, thus the plasma inside the tube cools and flows down along the field lines. Due to the strong superadiabatic temperature gradient in the upper convection zone, the down-flow of plasma inside the tubes leads to "convective collapse" (Parker 1978, Spruit 1979) which intensifies the flux tubes to high field strength (a few kilogauss) and results in the formation of sunspots, pores and faculae.

For the leading side, the large unfragmented flux tube cools as a whole and forms a large sunspot which encloses all the flux of the preceding polarity. For the following side, the fragmented smaller flux tubes cool individually and form numerous small spots, pores, or simply extended plage. We would expect the cooling process of the large leading flux tube be more efficient compared to the following small tubes, because heating of the single large flux tube by its surrounding hot plasma through radiative diffusion is less effective than the heating of individual small tubes.

The above analysis gives a natural explanation for the well-known observational result that the leading polarity of an active region tends to be in the form of large sunspots, whereas the following polarity tends to be more dispersed and fragmented, and that the leading spots tend to be larger in area, fewer in number, and have a longer lifetime than the following spots. The mean ratio of the effective flux in the preceding and the following spots is about 3:1 (see e.g. Babcock 1961, Bray & Loughhead 1979 pp. 226-236, and Zwaan 1981). In Zwaan (1981), an example of a mature active region was shown (see Figure 6-3 of Zwaan 1981), where most of the leading polarity magnetic flux is concentrated in a large sunspot, but most of the following polarity flux is present in the form of a dense plage without sunspots. In Table 6.2 of Bray & Loughhead (1961), the statistical distribution of spot groups according to magnetic class is presented. It is shown that αp and βp groups predominate over αf and βf groups. It is also shown that the leading spot tends to form earlier (by about a day) than the following spot, and

also outlive the following spot (see Bray & Loughhead pp. 226). All of these properties can be attributed to the stronger magnetic field strength in the leading side of the emerging loop.

Some previous suggestions have resorted to radial differential rotation in the convection zone to explain the predominance of the leading spots. (see e.g. Babcock 1961; Meyer, Schmidt, & Weiss 1977; van Driel-Gesztelyi & Petrovay 1990; Petrovay, et al. 1990). However, these suggestions are largely descriptive and there is yet no consensus on the exact nature of the distortion in the loops which a radial differential rotation might induce. Moreover, the differential rotation profiles used in different models are *ad hoc* and contradict one another. For example, Babcock (1961) explains the morphological asymmetries in terms of a decrease in the rotation rate with depth, while Meyer, Schmidt, & Weiss (1977) invokes a rotation rate which increases with depth. A fully dynamic simulation of the motion of flux tubes subject to the observed differential rotation profile within the convection zone would be necessary to determine the amount of distortion produced on the rising loops and its contribution, if any, to active region asymmetries. However, we wish to emphasize that the observed morphological asymmetry of bipolar magnetic active regions can naturally arise simply from solid body rotation, without even resorting to differential rotation. Thus we believe that the larger field strength of the leading side of an emerging loop, resulting from the combined effects of anchoring and the Coriolis force, is the primary origin of the observed larger and longer lived preceding sunspots in an active region.

The consistency between the results of our simulations and the well known observational asymmetry in active regions adds support to the current consensus that the solar surface magnetic active regions are formed through the emergence of the buoyantly unstable magnetic flux loops from the base of the convection zone where the dynamo mechanism is concentrated; the flux loops which form the surface active regions must also have their innermost portions anchored beneath the base of the convection zone.

The dependence of the latitude of emergence on initial field strength B_0 shown in Figure 2.3 suggests the possibility of reproducing the observed surface butterfly diagram by increasing the amplitude of B_0 with time, while keeping θ_0 and Φ fixed. Consider the $\Phi = 10^{22}$ Mx curve for $\theta_0 = 1^\circ$ in Figure 2.3: If we inject flux tubes at the base of the convection zone with B_0 varying from 30 kG to 70 kG over the course of 11 years, a butterfly diagram may be achievable. An increasing B_0 with time during each solar cycle may be expected for a distribution of flux tubes in the overshoot region which has the same initial field strength, but different initial depths. Stretching the flux tubes by differential rotation will cause the tubes to rise and eventually enter the buoyantly unstable convection zone (Fisher, McClymont, & Chou 1991). Shallower flux tubes are injected into the convection zone earlier and are less amplified compared to initially deeper tubes, thus generating flux tubes that enter the convection zone with increasing field strength, and therefore emerging at decreasing latitudes as the solar cycle progresses. However, the major difficulty with this scenario is that the sign and the amplitude of the toroidal field must

change abruptly from one cycle to the next. It is hard to imagine a scheme for generating such a time varying magnetic field in the overshoot layer.

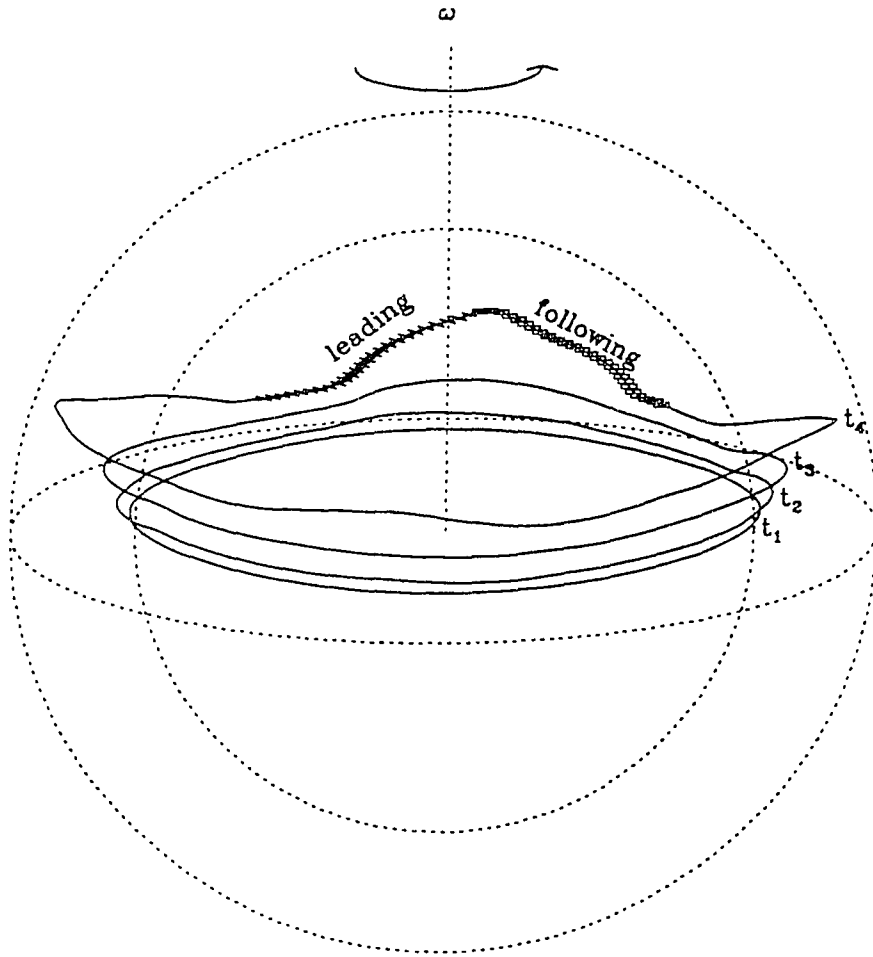


Figure 2.1 The non-axisymmetric eruption of a toroidal flux ring with initial field strength $B_0 = 3 \times 10^4$ G, $\Phi = 10^{22}$ Mx, and initial latitude $\theta_0 = 5^\circ$ N, viewed from 30° above the equator. A wave-like perturbation with 4 full wavelengths along the circumference of the ring is imposed at the beginning. At $t_1 = 0$, the flux ring is released and the configurations of the flux ring at 4 consecutive times, t_1, t_2, t_3, t_4 , with a constant separation of approximately 32 days, are shown with solid curves. The solid curve labeled t_4 shows the final configuration of the flux ring in the simulation. Four emerging flux loops are formed along the ring. One of the four loops along the flux ring of t_4 is marked with crosses for its leading side and squares for its following side. The inner dotted circle represents the base of the convection zone and the outer dotted circle marks the photosphere.

Figure 2.2 The loop rise time as a function of initial field strength at the base of convection zone for loops with different total flux Φ , and different initial latitude θ_0 .

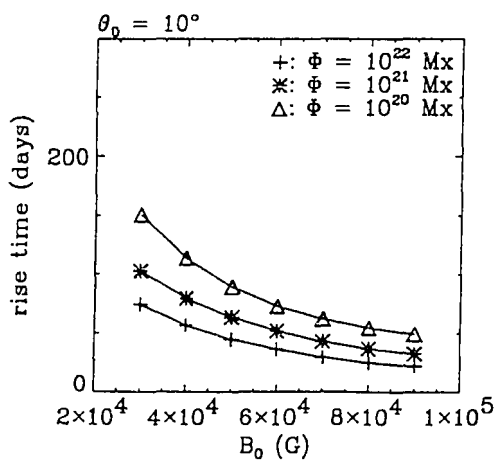
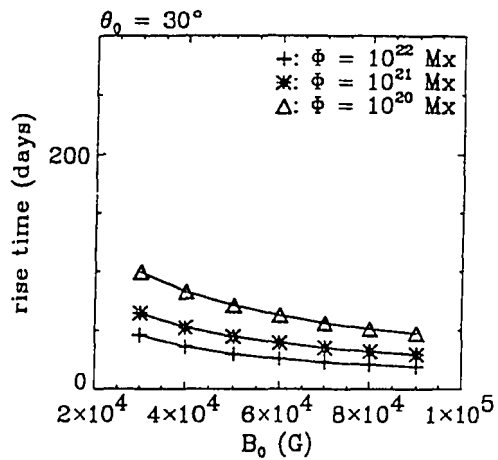
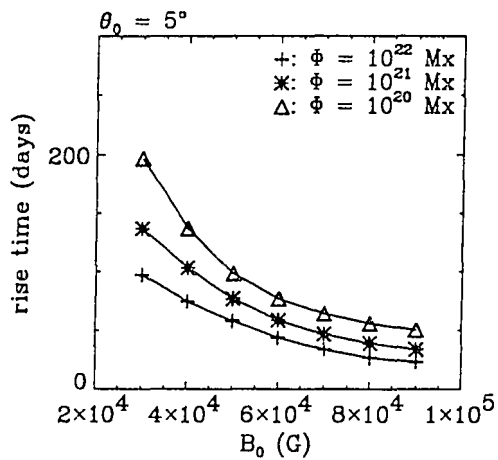
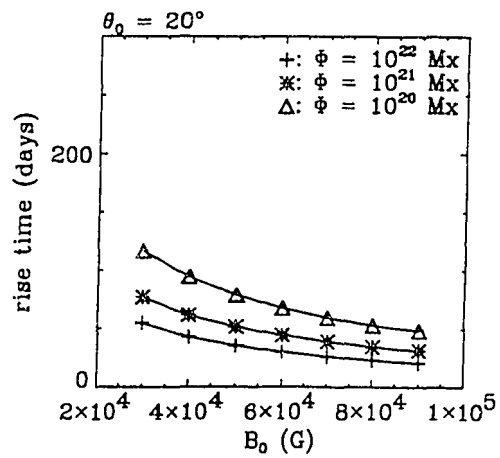
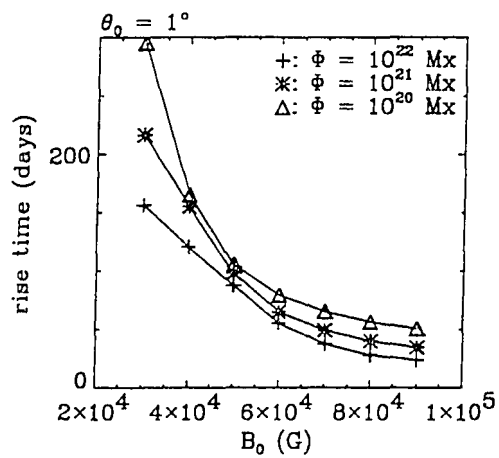
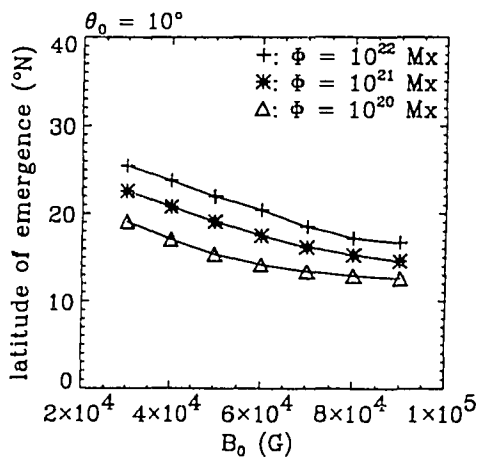
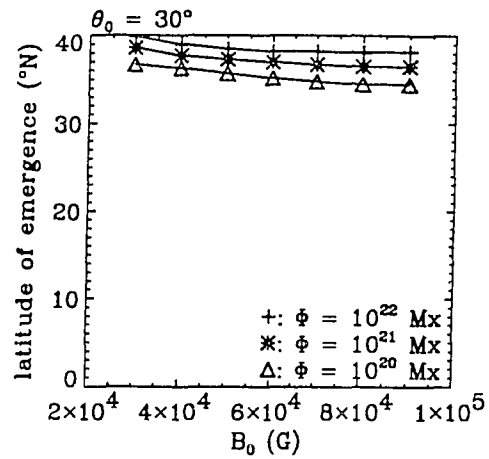
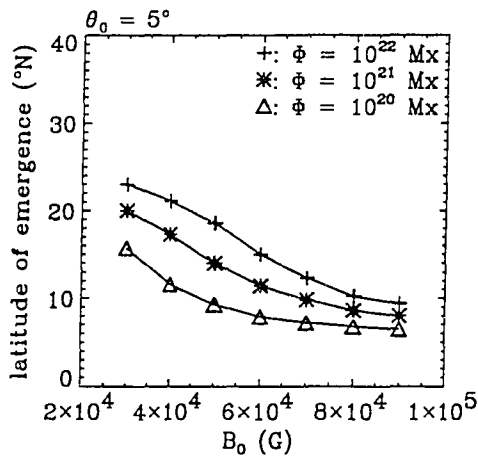
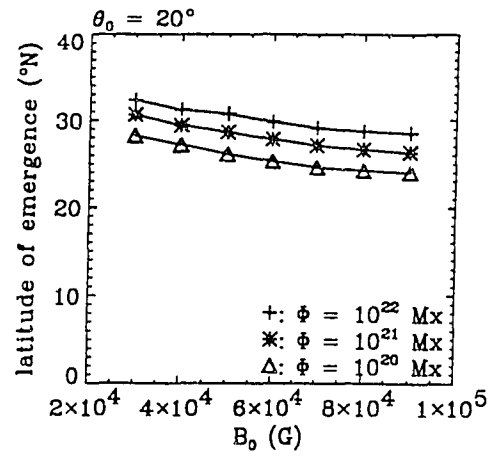
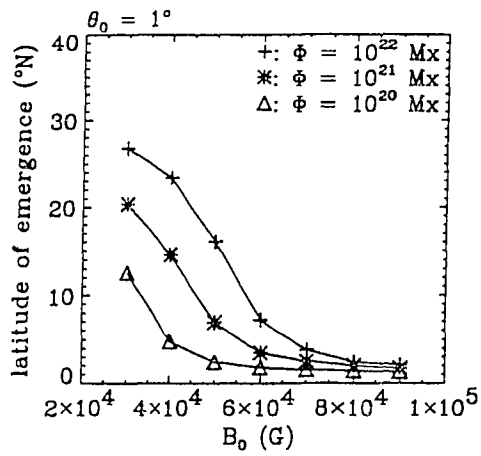


Figure 2.3 The latitude of flux emergence as a function of initial field strength at the base of the convection zone for loops with different total flux Φ , and different initial latitude θ_0 .



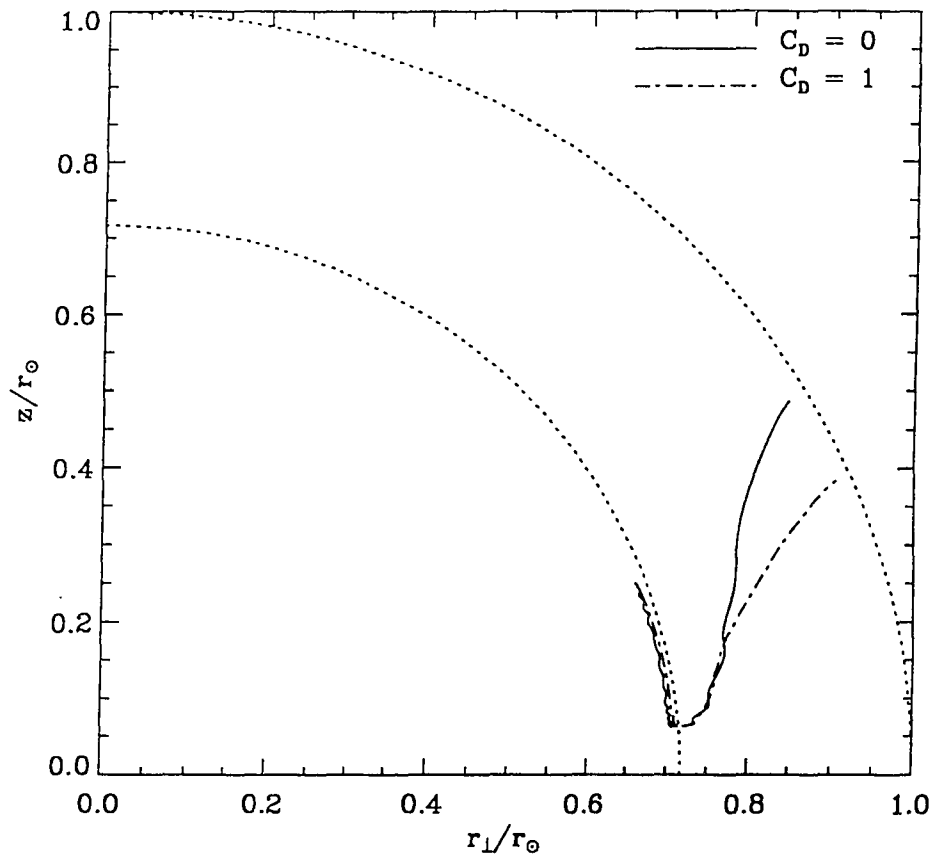


Figure 2.4 The trajectories of the outermost and the innermost parts of the flux ring, as viewed in the meridional plane. The solid lines represent the case with $C_D = 0$ and the dashed dot lines represent the case with $C_D = 1$. In both cases, $B_0 = 3 \times 10^4$ G, $\Phi = 10^{22}$ Mx, and $\theta_0 = 5^\circ$ N.

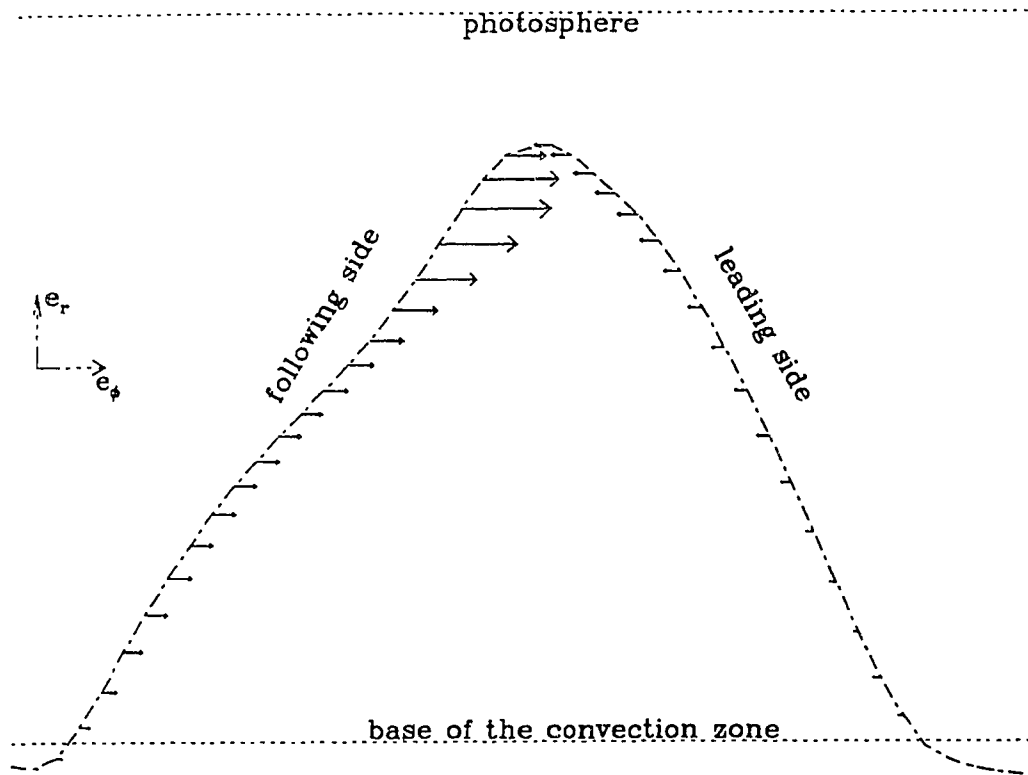


Figure 2.5 A snap shot of the ϕ component of the drag force per unit length $F_{D\phi}$ experienced by one of the rising loops along the flux ring in the simulation with $B_0 = 10^4$ G, $\Phi = 10^{22}$ Mx, $\theta_0 = 5^\circ$ N, and C_D set to 1. The magnitude of $F_{D\phi}$ is proportional to the length of the arrows.

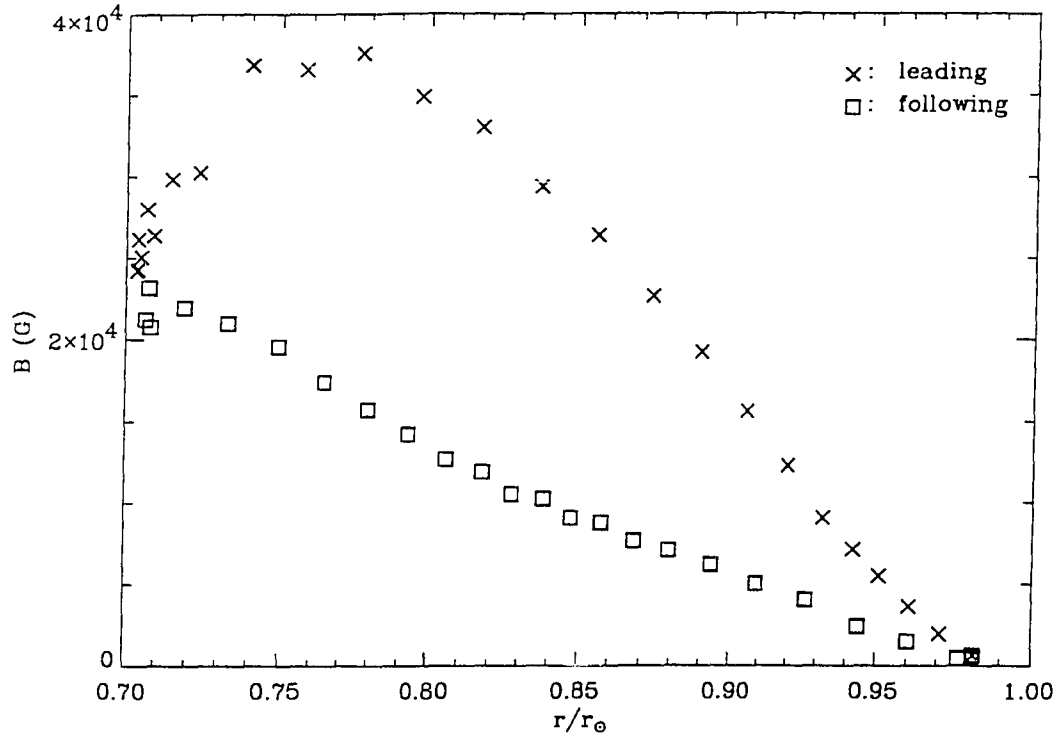


Figure 2.6 The final magnetic field strength along the emerging loop as a function of the radial distance to the center of the Sun, resulting from the simulation with $B_0 = 3 \times 10^4$ G, $\Phi = 10^{22}$ Mx and $\theta_0 = 5^\circ$. The crosses and squares here correspond to those in Figure 2.1.

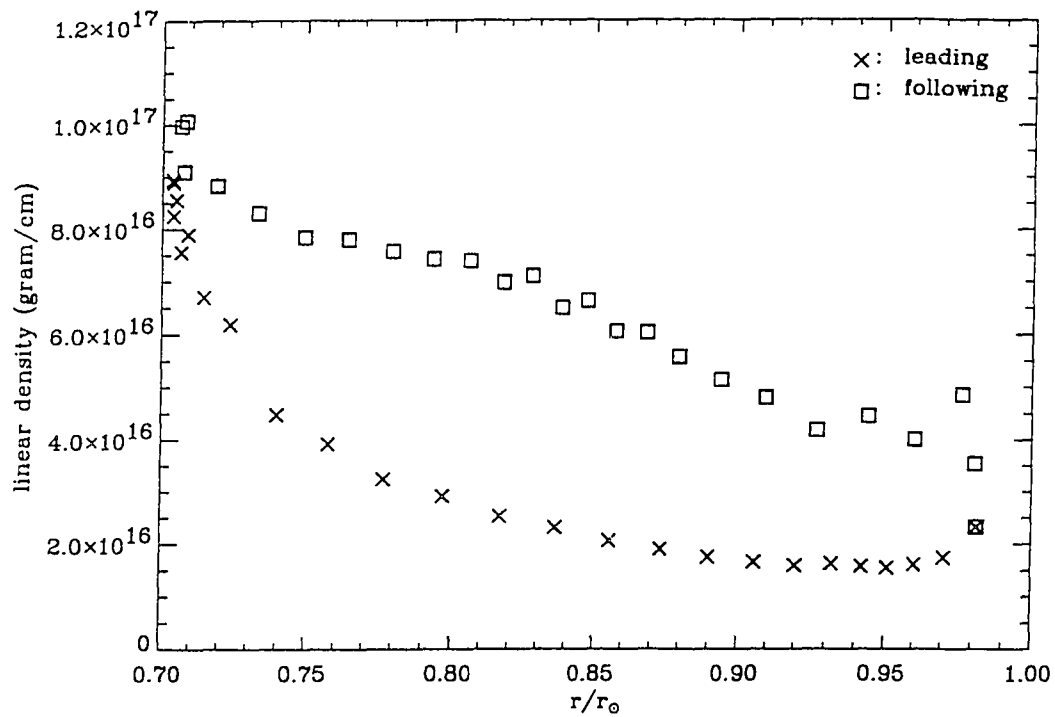
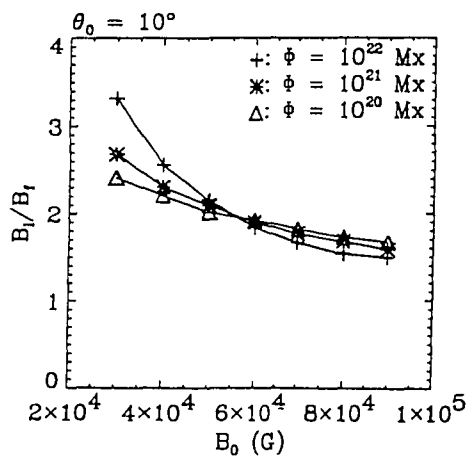
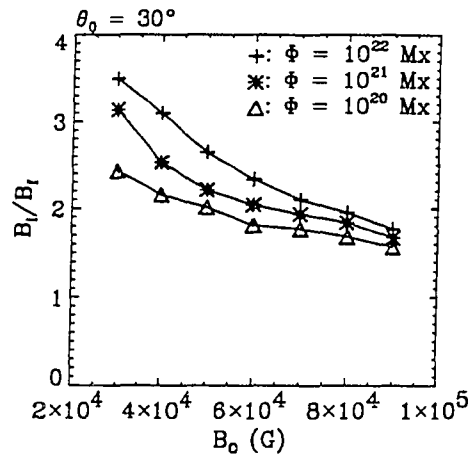
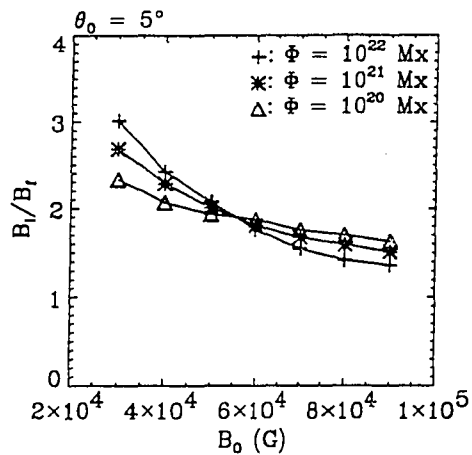
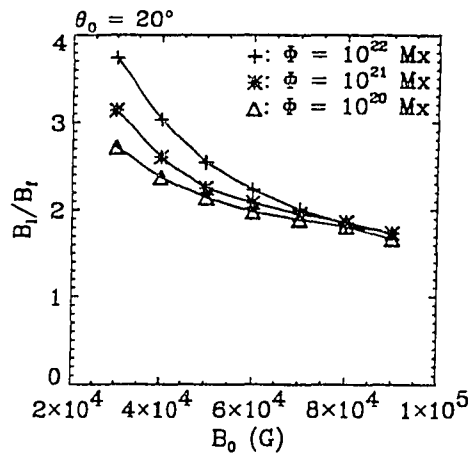
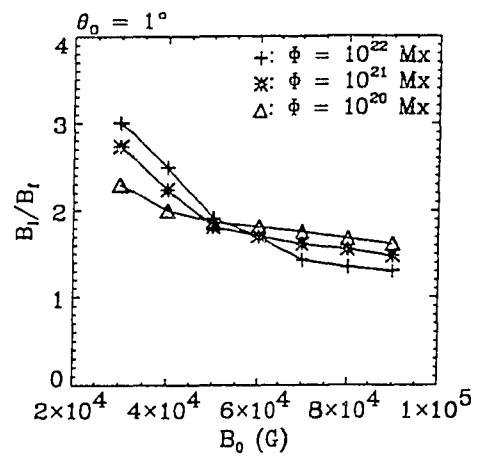


Figure 2.7 The final mass distribution along the emerging loop as a function of the radial distance to the center of the Sun. Like Figure 2.6, the crosses and squares here correspond to those marked on the emerging loop shown in Figure 2.1. The mass distribution is expressed in terms of mass per unit length, i.e. linear density.

Figure 2.8 The ratio B_l/B_f , with B_l and B_f being the magnetic field strength of the leading and the following sides of an emerging loop evaluated at the depth half way between the base of the convection zone and the photosphere, resulting from simulations with different initial field strength B_0 , total flux Φ and initial latitude θ_0 .



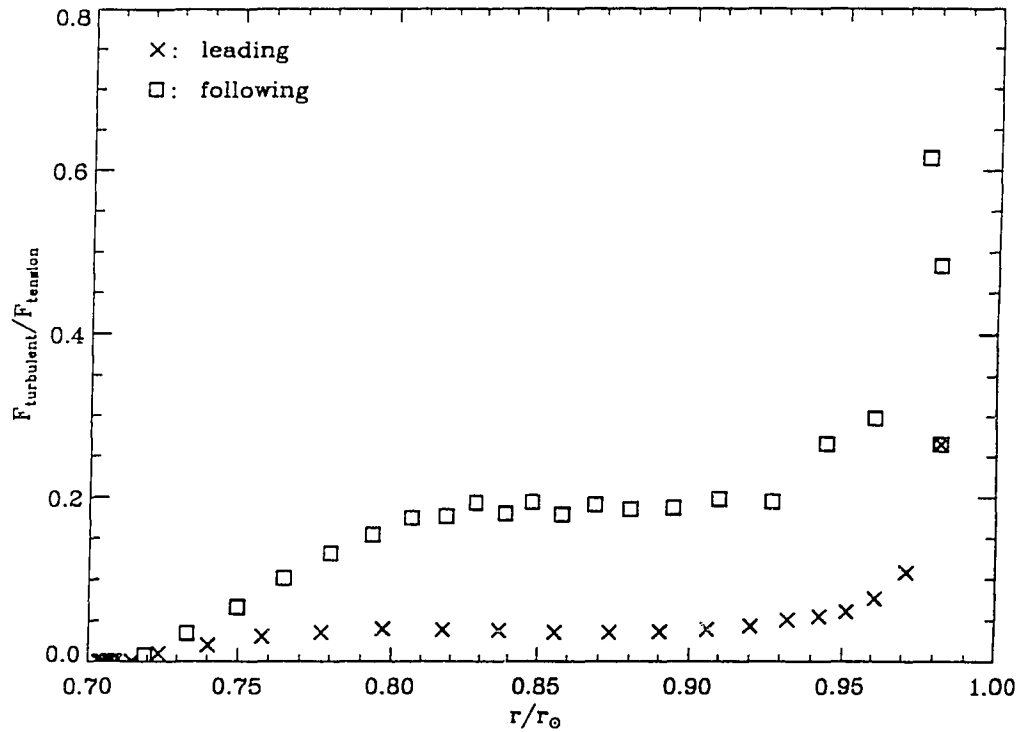


Figure 2.9 The ratio of the perturbing force from turbulent motions $F_{\text{turb}} \equiv C_D(\rho_e v_e^2/\pi a)$ and the restoring tension force of the tube $F_{\text{tens}} \equiv B^2/4\pi R$, as a function of the radial distance to the center of the Sun, calculated along the final emerging loop resulting from the simulation with $B_0 = 3 \times 10^4$ G, $\Phi = 10^{22}$ Mx and $\theta_0 = 5^\circ$ N.

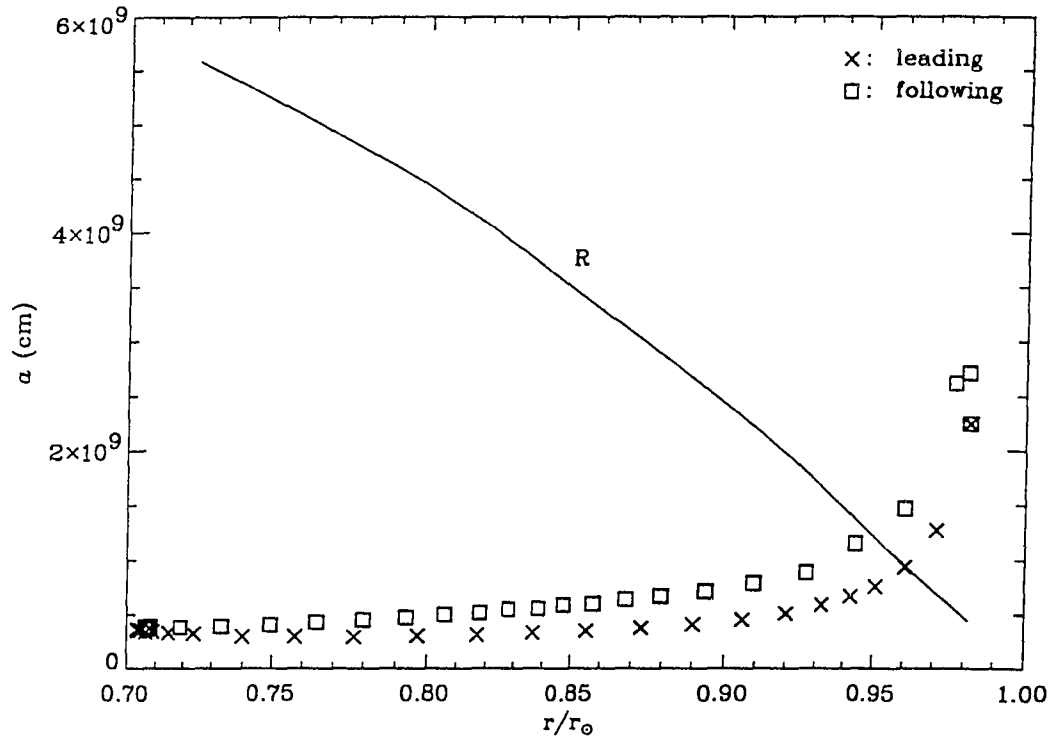


Figure 2.10 The radius of tube cross section a in comparison with the convective cell size R , as a function of the radial distance to the center of the Sun, along the emerging loop resulting from the simulation with $B_0 = 10^4$ G, $\Phi = 10^{22}$ Mx and $\theta_0 = 5^\circ$ N.

CHAPTER 3
DYNAMICS OF SINGLE EMERGING FLUX LOOPS

Abstract

The buoyant rise of a magnetic flux loop arising from a single perturbed segment of a toroidal flux ring lying slightly beneath the base of the convection zone is studied by way of numerical simulations. We have considered flux loop evolution assuming both solid-body rotation, and differential rotation consistent with recent results from helioseismology. Our major conclusions are the following:

1) The latitudes of loop emergence are consistent with the observed butterfly diagram, assuming a dynamo wave propagating from 30° latitude to the equator at the base of the convection zone. In the case of solid-body rotation, we require toroidal field strength $B_0 \geq 60$ kG to avoid a significant equatorial gap, but if differential rotation is included, $B_0 \geq 30$ kG leads to an acceptable butterfly diagram.

2) The Coriolis force induced by the diverging east-west velocity near the loop apex acts to twist the loop as it rises and produces a tilt angle upon emergence, with the leading leg of the loop closer to the equator than the following. For physically reasonable choices of toroidal field strength $30 \text{ kG} \leq B_0 \leq 90 \text{ kG}$, we find that the computed tilt angles are consistent with both the magnitude and the latitudinal variation of observed active region tilt angles. In particular, the relationship

between the tilt angle α and the active region latitude θ : $\sin \alpha = 0.48 \sin \theta$, resulting from the observation by Wang & Sheeley, is closely matched by our simulation results for $B_0 = 50$ kG and flux $\Phi = 10^{22}$ Mx.

3) From a simple force balance analysis, we derive a scaling law for the tilt angle α in terms of the characteristic field strength B , latitude θ , and the total flux Φ of the loop: $\alpha \propto \sin \theta B^{-5/4} \Phi^{1/4}$. We find that this scaling relation describes most of our simulations reasonably well.

4) We find that for toroidal field strengths $B_0 \leq 20$ kG, loops become inversely tilted upon emergence. In particular, for $B_0 \sim 10$ kG, the magnitude of the inverse tilt angles at emergence can be higher than 90° , i.e. violating the Hale's polarity laws. The cause of the inverse tilt for weak flux loops is a strong converging parallel flow that sets in when the loop apices reach the upper layers of the convection zone.

5) We still find, as we did in the multi-loop studies in Fan, Fisher and DeLuca, that the magnetic field in the leading leg of an emerging loop is approximately twice that in the following leg. We argue that this field strength asymmetry is the origin of morphological asymmetries in bipolar active regions.

3.1. Introduction

In Chapter 2, we developed a numerical model to follow the evolution of a thin, closed magnetic flux tube moving in three dimensions in the solar interior. We then applied this model to study the evolution of a closed toroidal magnetic flux ring, lying initially at the base of the convection zone, and perturbed with a periodic wave pattern. Segments that are perturbed above the base of the convection zone eventually develop into multiple emerging flux loops, while the innermost portions of the toroidal ring remain anchored beneath the base of the convection zone by the subadiabatic temperature stratification there. From that study, we found the important result that each emerging loop develops a magnetic field strength asymmetry, in the sense that the field strength of the leading leg (leading in the direction of rotation) of each loop is approximately twice that in the following leg at any chosen depth in the convection zone. This field strength asymmetry, as argued in Chapter 2, provides a natural explanation for the observed morphological asymmetries of bipolar active regions, namely that the leading polarity of each region is generally more compact and less fragmented when compared to the following polarity.

In this Chapter, we continue our study of the nonlinear emergence of anchored magnetic flux loops using the numerical thin flux tube model described in Chapter 2. A major change in the model we have made for this work is the nature of the flux eruption pattern. All previous simulations of flux tube motions in a 3D spherical geometry (e.g. Choudhuri 1989; D'Silva 1992; D'Silva & Choudhuri

1993) have assumed that the toroidal ring is initially perturbed by a periodic wave pattern, so that multiple loops rise simultaneously in the convection zone. However, it is unlikely that nature would conspire to perturb the toroidal ring in such a coherent way. The more likely scenario is that only one segment of the toroidal ring is perturbed into an unstable configuration at any given time, and a single emerging loop arises from that segment. Thus, the focus of this Chapter is the evolution of a toroidal flux ring originally lying slightly beneath the base of the convection zone, of which one segment is displaced upward into the convection zone. We will let the length of the perturbed segment be a variable parameter in the numerical simulations. In §3.2, we present an overview of the basic physics and the general features of the numerical simulations. We show that the change from the multiple loop case assumed in Chapter 2 to the single loop case does not alter the result of field strength asymmetry. The magnitude of the field strength asymmetry remains unchanged, strengthening our original conclusions regarding the origin of morphological asymmetries of bipolar active regions. In §3.3, we discuss the critical condition regarding the length scale of the perturbed segment of the toroidal ring, for flux emergence to take place. We show that a perturbed segment will not develop into an emerging loop unless its length scale exceeds a certain critical value.

Previous studies have shown that the Coriolis force causes the latitude of flux emergence at the photosphere to be greater than the initial "injection" latitude of the toroidal ring (Choudhuri & Gilman 1987; Choudhuri 1989; also Chapter 2). If we

adopt as a working hypothesis that the toroidal magnetic flux originates from a dynamo operating in the overshoot layer beneath the convection zone, then it is important to know whether an equatorward propagating dynamo wave can, through flux eruption, lead to the observed butterfly diagram (e.g. Maunder 1922; Wang & Sheeley 1989) for active regions at the solar surface. In §3.4, we show that the emerging latitude of the flux loop for the single loop case is reduced significantly compared to the multiple loop case, and that the latitude of flux emergence reflects more closely the initial latitude of the toroidal flux tube.

A major topic we address in this Chapter is the tilt of emerging active region flux tubes with respect to the azimuthal (east-west) direction. Observations show that the axis connecting the leading and the following polarities of each active region generally shows a tilt relative to the east-west direction, with the leading polarity equatorward of the following polarity. The magnitude and variation of the measured tilt angles with latitude of the regions are summarized by the well-known "Joy's Law" (Hale et. al 1919). More recent observational studies of active region tilt angles have been carried out by Wang & Sheeley (1989, 1991) and Howard (1991a,b). Although many suggestions have been made regarding the origin of these tilt angles (see e.g. Babcock 1961, Wang & Sheeley 1991, D'Silva 1992; D'Silva & Choudhuri 1993), only one set of dynamic calculations of the tilt angles of emerging flux loops has been done (D'Silva 1992, D'Silva & Choudhuri 1993), in which the multiple loop case was used. In §3.5, we discuss the results of loop tilt angles from our single loop calculations and compare them with observations.

In §3.6, we present the results of simulations which include differential rotation in the convection and radiative zones, as inferred from helioseismic inversions (see, e.g., Dziembowski, Goode, & Libbrecht 1989; Brown et al. 1989; Goode et al. 1991). A comparison of these results with those which assume solid-body rotation (§§3.4-3.5) quantitatively determines the amount of distortion of a rising flux loop produced by differential rotation, and sheds light on the role of differential rotation in the dynamics of flux emergence.

Finally, we summarize the major conclusions of our flux loop calculations in §3.7.

3.2. Description of the Numerical Simulations

The numerical model used to solve the time evolution of a thin, closed magnetic flux tube moving in 3 dimensions in the solar interior is presented in detail in Chapter 2. Here we simply recall the equation of motion for the magnetic flux tube in the rotating frame (with angular velocity ω) of the Sun:

$$\frac{d\mathbf{v}}{dt} = -2\omega \times \mathbf{v} + \frac{\rho - \rho_e}{2\rho} \mathbf{g} + \frac{B^2}{8\pi\rho} \mathbf{k} + \left[\frac{\rho - \rho_e}{2\rho} g_l + \frac{1}{\rho} \frac{\partial}{\partial s} \left(\frac{B^2}{8\pi} \right) \right] \mathbf{l} - \frac{C_D}{2\sqrt{\pi\Phi}} \frac{\rho_e \sqrt{B}}{\rho} |\mathbf{v}_\perp| \mathbf{v}_\perp, \quad (3.1)$$

where, \mathbf{v} is velocity of each point of the tube, \mathbf{v}_\perp is the component of \mathbf{v} perpendicular to the flux tube, s is arclength along the tube, measured in the direction of rotation from some predefined origin, ρ and ρ_e are respectively the density of plasma inside and outside the flux tube, \mathbf{g} is the gravitational

acceleration, g_t is the component of \mathbf{g} parallel to the tube, Φ is the total magnetic flux of the tube, B is the magnetic field strength inside the flux tube, ω is the angular velocity of the frame co-rotating with the Sun, and C_D is the drag coefficient which is generally of order unity (see e.g. Batchelor 1967; Parker 1979b) and is set to 1 in this chapter. The unit tangent vector and the curvature vector of the flux tube are given respectively by $\mathbf{l} = \partial\mathbf{r}/\partial s$ and $\mathbf{k} = \partial\mathbf{l}/\partial s = \partial^2\mathbf{r}/\partial s^2$.

On the right hand side of equation (3.1), the first three terms correspond to the accelerations due to, respectively, the Coriolis force, the buoyancy, and the magnetic tension. The fourth term, when combined with the parallel component (parallel to the tube) of the buoyancy term, represents the acceleration parallel to the flux tube arising from the imbalance between the pressure gradient and gravity in the \mathbf{l} (parallel) direction. The last term is the acceleration from the aerodynamic drag force. We ignore forces from turbulent convective motions because the high regularity of active region orientations suggests that turbulent motions in the convection zone are unimportant in the emergence of magnetic flux tubes (van Ballegoijen 1982).

Equation 3.1 assumes that the Sun rotates rigidly and ignores the differential rotation of the Sun. In §3.6 we discuss how the model can be modified to include the effect of the large scale velocity field corresponds to solar differential rotation.

Unlike previous simulations which assumed that the ring at the base of the convection zone was perturbed with a periodic wave pattern, we assume here that only one segment of the toroidal ring, which lies slightly beneath the base of the

convection zone, is perturbed upward into the convection zone. The initial configuration of the toroidal ring is expressed as

$$r = r_0 + \Delta r_0 \exp\left[-\left(\frac{2(\phi - \phi_0)}{\Delta\phi}\right)^2\right], \quad (3.2)$$

$$\theta = \theta_0, \quad (3.3)$$

where r is distance from the center of the Sun, θ is latitude, ϕ is longitude, r_0 is the radius of the unperturbed toroidal ring (which is located at 1×10^9 cm below the base of the convection zone), and $\Delta r_0 = 1.1 \times 10^9$ cm and $\lambda \equiv r_0 \Delta\phi$ give respectively the amplitude and length scale of the perturbed segment of the toroidal ring.

Figure 3.1(a) shows an example of the initial configuration of the ring, as viewed from the north pole of the Sun. In this example, $\lambda = 4 \times 10^{10}$ cm and $\theta_0 = 5^\circ$ N. The segment centered at ϕ_0 is being perturbed into the convection zone. Other initial conditions are the same as those assumed in Chapter 2 and Choudhuri (1989): The ring is initially in thermal equilibrium with its surroundings and $\beta \equiv P_e/p_b$ is assumed constant along the ring, where P_e is the external pressure and $p_b \equiv B^2/8\pi$ is the magnetic pressure inside the flux tube. Thus, in the direction parallel to the flux tube, the plasma inside the tube is initially in hydrostatic equilibrium; however in the direction perpendicular to the flux tube, the forces do not balance, i.e. the flux tube is buoyant. Under the initial conditions stated above, the initial field strength is not uniform along the ring because β is assumed uniform, although the variation of field strength along the initial toroidal ring is small (less than 10%). One can prescribe B_0 , the field strength of the ring at the base of the

convection zone, and then the field strength at each point along the initial ring is determined. In the example given here, $B_0 = 30$ kG. The total magnetic flux of the ring $\Phi = 10^{22}$ Mx.

The subsequent evolution of the ring is shown in Figure 3.1(b)-(c), where the configurations of the ring at 5 instants during its evolution are given (solid curves), as they are viewed from (b) the north pole, and (c) 5° above the equator. The perturbed segment develops into an emerging loop of flux, while the remainder of the initial toroidal flux ring quickly loses its buoyancy (because of the subadiabatic gradient of the overshoot region) and reaches an equilibrium depth beneath the base of the convection zone. In Figure 3.1(c), one can see the development of a tilt of the loop (the relative lowering in latitude of the leading leg compared to the following leg), as it rises. The direction of this tilt is consistent with the observed tilt angle of active regions (e.g. Hale et al. 1919).

To investigate the robustness of the result on the magnetic field strength asymmetry described in Chapter 2, Figure 3.2 shows the variation of field strength along the emerging loop. The magnetic field strength in the leading leg of the emerging loop is approximately twice that in the following leg at any chosen depth in the convection zone, in agreement with the result from Chapter 2. We therefore stand by the conclusion of Chapter 2 that the asymmetry in the field strength can account for the origin of morphological asymmetries in bipolar active regions.

In this Chapter, we investigate the latitude of emergence and the tilt angle of an active region, using our simulations of single emerging loops as that described in

Figure 3.1. In §3.4 and §3.5, we present and discuss the results on latitudes of emergence and tilt angles from simulations assuming solid-body rotation of the Sun with $\omega = 2.73 \times 10^{-6}$ rad s⁻¹. The influence of differential rotation on the dynamics of rising flux loops is studied in §3.6 by incorporating a large scale velocity field into our numerical model. We present in detail simulations that span physically reasonable ranges of toroidal field strength B_0 , flux Φ , initial latitude θ_0 and the length scale of perturbation λ : $30 \text{ kG} \leq B_0 \leq 90 \text{ kG}$, $10^{20} \text{ Mx} \leq \Phi \leq 2 \times 10^{22} \text{ Mx}$, $1^\circ \leq \theta_0 \leq 30^\circ$, and $3 \times 10^{10} \text{ cm} \leq \lambda \leq 5 \times 10^{10} \text{ cm}$. These ranges for the initial parameters of the simulations are similar to those used in Chapter 2. We chose $B_0 \geq 30 \text{ kG}$ to ensure that the drag force from turbulent motions remain negligible compared to the magnetic tension force in the bulk of the convection zone (Chapter 2). We will show in §3.5 that loops with initial field strength $B_0 \leq 20 \text{ kG}$ emerge with opposite tilts from those of active regions, suggesting that toroidal flux tubes which give rise to the majority of active regions should have field strengths higher than 20 kG. The range of Φ used here covers the observed flux range for active regions (see e.g. Wang & Sheeley 1989). We have chosen the above range for θ_0 because overshoot layer dynamo models which have the correct direction of dynamo wave propagation should operate at latitudes between $\pm 30^\circ$ (DeLuca & Gilman 1986; Gilman et al. 1989; DeLuca & Gilman 1991). In § 3.3, we discuss briefly the choice of λ , i.e. the length scale of the initially perturbed segment.

3.3. The Critical Length Scale for Flux Emergence

Previous numerical simulations of magnetic flux loops in a plane parallel convection zone (Moreno-Inertis 1986; Chou & Fisher 1989; Fisher, Chou, & McClymont 1989) have shown that there exists a critical length λ_c for the initially perturbed tube segment: for $\lambda < \lambda_c$ the flux tube reaches a stable equilibrium, while for $\lambda > \lambda_c$ an unstable eruption to the photosphere occurs. A linear stability analysis of toroidal flux rings in the equatorial plane of a non-rotating spherical stellar envelope by Spruit & van Ballegooijen (1982a,b) shows that the instability condition for a wave-like perturbation of azimuthal order m is

$$\frac{\beta\delta}{2} > (m^2 - 1)f^2 + \frac{2f}{\gamma} - \frac{1}{2\gamma}. \quad (3.4)$$

In other words, the length scale for each wave crest $\lambda \equiv \pi r_0/m$ should satisfy

$$\lambda > \frac{\pi r_0 f}{\left[\frac{\beta\delta}{2} - \frac{2f}{\gamma} + \frac{1}{2\gamma} + f^2 \right]^{1/2}}. \quad (3.5)$$

Here r_0 is the radius of the unperturbed toroidal ring, $\beta \equiv P_e/p_b$, $\delta \equiv \nabla - \nabla_{ad}$, $\gamma \equiv c_p/c_v$ is the ratio of specific heats, and $f \equiv H_p/r_0$, with H_p being the local pressure scale height.

The existence of the critical length scale is a result of competition between the buoyancy force and the restoring magnetic tension force. The buoyancy force causes the perturbed tube segment to rise, while magnetic tension tries to pull it back. The fate of the perturbed segment depends on the rates of increase of the two forces with height. The rate of increase of the buoyancy force with height is

determined by the stratification of the external atmosphere and also the thermodynamic properties of the tube plasma. The rate of increase of the tension force with height varies inversely with the horizontal length scale of the perturbed segment; thus shorter length scales result in faster growth of the tension force with height. Unstable flux loop eruption to the photosphere occurs only if the rate of increase of the buoyancy force is greater than that of the tension force. Based on this principle, we have evaluated the critical length scale taking into account only the buoyancy and tension forces at the apex of the perturbed segment. We carried out a Taylor expansion of the two forces in terms of the radial displacement of the apex around the mechanical equilibrium state in which buoyancy balances the tension force. In our calculation, we assumed that the tube plasma remains in hydrostatic equilibrium in the direction parallel to the flux tube. By equating the rates of increase of the two forces with height, we obtain the critical length scale:

$$\lambda_c = \frac{\sqrt{8}r_0f}{\left[\frac{\beta\delta}{2} - \frac{2f}{\gamma} + \frac{1}{2\gamma} + f^2\right]^{1/2}}. \quad (3.6)$$

This expression for λ_c agrees very well with the result given by Spruit & van Ballegooijen (1982a,b) as shown in equation (3.5), except for the numerical factor of $\sqrt{8}$ vs. π . This difference arises because we assumed a Gaussian profile for the perturbed segment (eq. [3.2]), instead of the sinusoidal one used in Spruit & van Ballegooijen (1982a,b). Evaluating the above expression at the base of the convection zone, we obtain $\lambda_c \approx 3.8 \times 10^{10}$ cm. Furthermore, the inclusion of the solid-body rotation of the Sun will affect the stability condition of the flux rings,

and the analysis by van Ballegoijen (1983) shows that it results in an increase of the critical wavelength for unstable perturbations.

The above linear stability analyses help to explain the existence of a minimum length scale for flux loops to overcome the stabilizing effect of the tension force. However, these results are not directly applicable to our simulations for the following reasons. First, we are studying the evolution of perturbed toroidal rings at non-zero initial latitudes, whereas the above stability analyses (e.g. Spruit & van Ballegoijen 1982a,b; van Ballegoijen 1983) were done for toroidal flux rings in the equatorial plane of the Sun only. As pointed out by Moreno-Insertis (1991), a toroidal ring lying at non-zero latitudes has a component of the tension force in the θ (latitudinal) direction that can not be balanced by the buoyancy force, thus driving a slow poleward slipping of the ring. Second, we have assumed thermal equilibrium as the initial condition of our simulations, instead of the mechanical equilibrium condition from which the above stability analysis is carried out. In other words, in our simulations, both the perturbed segment and the rest of the toroidal ring are initially buoyant, although the rest of the toroidal ring beneath the convection zone quickly loses its buoyancy and evolves to a mechanical equilibrium state with tension balancing buoyancy in the radial direction.

From our simulations we find that the perturbed segment of a toroidal ring will not develop into a loop of flux that emerges to the surface unless its length scale exceeds a certain critical value λ_c . The simulations indicate that λ_c increases with decreasing field strength B_0 , and if $\lambda \geq 2.1 \times 10^{10}$ cm, all perturbed toroidal rings

with $B_0 \geq 30$ kG will give rise to emerging flux loops. This significantly smaller value of "critical length", compared to that obtained from equation (3.6), arises because we have assumed an initially buoyant toroidal ring in our simulations; the length scale of the perturbed segment increases by a significant amount as the remainder of the ring ascends and evolves toward the mechanical equilibrium beneath the base of the convection zone.

Figure 3.3 shows an example of the evolution of a perturbed toroidal ring with λ less than the critical value. In this case $\lambda = 2.0 \times 10^{10}$ cm, $\theta_0 = 1^\circ$, $B_0 = 30$ kG, and $\Phi = 10^{22}$ Mx. The configurations of the ring at seven uniformly spaced consecutive times during a total period of roughly 2.5 years is displayed in Figure 3, as viewed from (a) the north pole and (b) 10° above the equator. During the first few months, the loop is rising under the buoyancy force, and in the meantime, the entire ring moves toward higher latitude (see Fig. 3.3(b)). The driving forces of this northward motion of the ring are (1) the θ (latitudinal) component of the tension force and (2) the θ component of the Coriolis force which arises from the counter-rotating flow of the tube plasma induced by the rising motion of the loop. However, as the loop rises, the tension force, which tries to pull the loop back, increases. The rate at which the curvature of the loop apex grows is proportional to λ^{-2} . In this case, the length scale of the loop is sufficiently short to cause the tension force to grow faster than the buoyancy force and therefore, after the first few months, the rising motion subsides. As the loop stops rising, the northward motion of the ring also stops. Because the toroidal ring has moved to a higher

latitude, and the rising motion has subsided, the ring is overall closer to the rotational axis. Conservation of angular momentum, therefore, builds up a motion of the entire toroidal ring in the direction of rotation, i.e. the positive ϕ direction. The Coriolis force induced from this positive ϕ motion of the toroidal ring has a θ component that counteracts the θ component of the tension force, and hence stops the northward slippage of the ring. The toroidal ring as a whole thus reaches a nearly steady state after the second time step shown in Figure 3.3. The loop apex remains at the same depth, except for some small oscillations, and the average latitude of the toroidal ring remains at approximately 7° without further change. As can be seen from Figure 3.3, the toroidal ring as a whole (including the loop) rotates in the positive ϕ direction at a steady speed of roughly 2.2° per month. After about 2.5 years, the loop apex is still about 3.4×10^9 cm above the base of the convection zone, and the longitude of the apex has advanced from $\phi = 0^\circ$ to $\phi = 56^\circ$. Thus, in this case, the loop apex remains at a constant depth without rising to the surface.

Our goal in this paper is to model the nonlinear process of flux loop emergence and its implications for the formation and properties of bipolar magnetic active regions. We will therefore now focus on those cases where the perturbed segment directly develops into an emerging loop and reaches the surface layer within a reasonably short time scale (≤ 1 yr.). Thus our choices for the values of λ need to be greater than 2.1×10^{10} cm. We choose 3×10^{10} cm, 4×10^{10} cm and 5×10^{10} cm to be the sampled values of λ for our simulations. The loop rise times t_r

resulting from these λ values of the initially perturbed segment are presented in Figure 4. The rise time ranges from approximately 20 days to 200 days. As can be seen from the Figure, higher field strengths and higher fluxes both result in shorter rise times. In addition, as shown in Figure 3.5, the rise time also decreases with increasing λ to an asymptotic value; the asymptotic behavior implies that magnetic tension has become unimportant compared to the other forces (e.g. buoyancy and drag).

3.4. The Latitude of Flux Emergence

The emerging latitude θ_{em} of the flux loops from our simulations is shown in Figure 3.6 as a function of field strength B_0 for various cases with different θ_0 , Φ and λ . First, we can see clearly from the Figure that θ_{em} is always higher than the initial latitude θ_0 . This result has been noted in many previous studies (Choudhuri & Gilman 1987; Choudhuri 1989; D'Silva & Choudhuri 1993; also Chapter 2). As the toroidal flux ring (or a fraction of the toroidal ring) expands radially outward due to buoyancy, a counter-rotating flow is induced inside the ring as a result of the plasma in the tube attempting to conserve its angular momentum. This counter-rotating flow then induces a Coriolis force directed inward toward the rotation axis; the θ component of this Coriolis force drives the ring toward higher latitudes and thus leads to a higher θ_{em} than the initial latitude θ_0 .

To compare the values of θ_{em} we obtain here with those in Chapter 2 (from simulations of multiple [$m = 4$] emerging loops), we have plotted, in Figure 3.7, an

overlay of θ_{em} from Chapter 2 with the two panels of $\lambda = 4 \times 10^{10}$ cm in Figure 3.6. We can see that θ_{em} obtained from single emerging loop simulations (solid lines) is considerably reduced in comparison with that from Chapter 2 (dashed lines), for the weaker magnetic fields, while in the high B_0 range, the two sets of results tend to converge.

The reduction of θ_{em} for single loops compared to multiple emerging loops, can be understood qualitatively as follows. For a single emerging loop, a smaller fraction of the toroidal ring is moving outward and away from the rotation axis compared to the multiple loop case. Therefore, conserving angular momentum induces a weaker counter-rotating flow in the toroidal ring of the single emerging loop than in the ring of multiple emerging loops, and hence, a weaker Coriolis force arises to drive the poleward motion of the ring. The result is a lower value of θ_{em} for the single loop case. For the same reason, θ_{em} is lower when λ is smaller, as indicated in Figure 3.6.

Figure 3.6 also shows that θ_{em} generally decreases with increased field strength B_0 , except for those cases with high initial latitudes θ_0 , where θ_{em} varies very little with B_0 . The general decrease of θ_{em} with B_0 can be understood by noting that the buoyancy force scales as B_0^2 while the Coriolis force scales as $B_0^{3/4}$ (see Chapter 2). Thus increasing B_0 will make the buoyancy force relatively more dominant and cause the trajectory of the emerging loop to be more radial. However, as θ_0 increases, the θ component of the ring's tension force which drives the poleward slippage of the ring becomes increasingly significant (because it is

proportional to $\tan \theta_0$). Since the tension force scales with B_0^2 , in the same way as the buoyancy force, the increasing importance of this θ component of the tension force in determining the poleward motion of the toroidal ring causes the dependence of θ_{em} on B_0 to be flattened. In addition, the tension force is present over the entire toroidal ring, whereas the buoyancy force is confined solely to the emerging section of the ring. At high latitudes, therefore, the increase in the θ component of the tension force as a result of increasing B_0 , overall has a stronger effect than the increase of the buoyancy force, leading to even a slight increase in θ_{em} with increasing B_0 as seen in a few curves with high values of θ_0 in Figure 3.6.

The dependence of θ_{em} on the total flux Φ indicated in Figure 3.6 is that θ_{em} decreases with decreasing Φ , in agreement with the results of Chapter 2. The reason for this dependence, as discussed in Chapter 2 and also noted by D'Silva & Choudhuri (1993), is that smaller Φ results in a stronger drag force which can transfer angular momentum from the external fluid to the flux tube.

An important question which must be addressed is the possibility of reproducing the observed latitudes of surface active regions described as the butterfly diagram through flux emergence of toroidal flux tubes from the base of the convection zone. If we assume, as a working hypothesis, that at the base of the convection zone there is a dynamo wave of toroidal magnetic field propagating from $\theta_0 = 30^\circ$ toward the equator (DeLuca & Gilman 1986, 1991), what then is the surface manifestation of this dynamo wave as a result of flux eruption? Figure 3.8 shows how θ_{em} varies in response to a decreasing θ_0 for toroidal flux tubes with

different initial field strengths B_0 at the bottom of the convection zone. First, we find that for all the values of B_0 considered here, the latitudes of emergence θ_{em} are all within the observed sunspot zone. In addition, θ_{em} decreases monotonically with decreasing θ_0 , i.e. an equatorward propagating dynamo wave will be seen as an equatorward migrating band of active region emergence. If the toroidal flux tubes have a field strength of $B_0 = 30$ kG, then we can see from Figure 3.8 that θ_{em} remains above θ_0 by over 5° as θ_0 approaches 0° , meaning that there exists an equatorial gap which is devoid of active region emergence. However, if B_0 for the toroidal flux tubes is equal to or greater than 60 kG, the difference between θ_{em} and θ_0 essentially decreases to zero in the limit of θ_0 approaching 0° , and the equatorial gap disappears. From the butterfly diagram of active regions with $\Phi \geq 5 \times 10^{21}$ Mx given in Wang & Sheeley (1989), we see that the active region population extends from about 40° latitude all the way to the equator. This suggests that toroidal flux tubes with field strength $B_0 \geq 60$ kG must exist, in order to explain the presence of emerging active regions very close to the equator. This, however, does not exclude the presence of toroidal flux tubes of $B_0 \approx 30$ kG, and in fact, the decrease of active region populations within a few degrees of the equator may be attributable to a fraction of the active region flux tubes having initial field strength $B_0 \approx 30$ kG. To summarize, the comparison between the results of our simulations and the observed active region latitudes suggests that an equatorward propagating dynamo wave (from $\theta_0 = 30^\circ$ to the equator), can reproduce the observed butterfly diagram at the surface through flux eruption, if some toroidal flux

tubes with a field strength as strong as approximately 60 kG exist near the equator in the dynamo layer.

The above conclusions are based on calculations assuming solid-body rotation of the Sun. We will show that if effects of differential rotation are included in the flux tube equation of motion, the need for such high field strengths may be ameliorated (see §3.6).

3.5. Tilt Angles

3.5.1 *Overview of Results from Simulations*

D'Silva (1992) and D'Silva & Choudhuri (1993) found that emerging flux loops develop a tilt as a result of the Coriolis force acting on the rising loops. We find similar results in our present simulations: the leading leg of each emerging loop is at a lower latitude than the following leg at any depth in the convection zone. This is clearly illustrated in Figure 3.9 which shows the variation of latitude along the loop as a function of depth. The direction of this tilt is consistent with the observed tilt angles of active regions. In order to quantitatively compare the tilts of the emerging loops from our simulations with observed tilt angles of active regions, we define the tilt angle α of an emerging loop as the angle between the tangent vector ($\mathbf{l} \equiv \partial \mathbf{r} / \partial s$) at the apex of the loop and the positive ϕ direction (i.e. the direction of rotation). If the tangent vector at the apex is tilted equatorward relative to the positive ϕ direction, then the tilt angle α is assigned to be positive, or "correctly" tilted. If, on the other hand, the tangent vector is tilted poleward

relative to the positive ϕ direction, then α is assigned to be negative, or "inversely" tilted.

Figure 3.10 shows the computed α of emerging loops as a function of the emerging latitude θ_{em} of the loops. The six panels of Figure 3.10 correspond to cases with different total flux and length scale of the initially perturbed segment. Generally we find that α increases with the latitude of emergence θ_{em} , in agreement with "Joy's law". The increase of α with θ_{em} is not strictly linear, being steeper for smaller θ_{em} . In a few cases with weak field strength, α begins to fall off at high latitudes. However, if we disregard the high latitude portions of the curves with $B_0 = 30$ kG, we can see from Figure 3.10 that α decreases with increasing field strength B_0 . It is also evident that α increases with increasing total magnetic flux Φ , and appears to decrease with increasing λ .

3.5.2 A Simple Analysis of the Origin and Variations of Tilt

As noted by D'Silva & Choudhuri (1993), magnetic buoyancy stretches the rising flux loop and makes particles at the top of the loop move away from each other. The Coriolis force acting on this diverging velocity twists the loop to produce a tilt. In spherical coordinates, the Coriolis force is

$$\mathbf{f}_c = -2v_\theta\omega_\theta\mathbf{e}_r + 2v_\phi\omega_r\mathbf{e}_\theta + (2v_r\omega_\theta - 2v_\theta\omega_r)\mathbf{e}_\phi, \quad (3.7)$$

where $\omega_\theta = \omega \cos \theta$ and $\omega_r = \omega \sin \theta$ are respectively the θ and the r components of the angular velocity. Note that although we use θ to denote latitude, rather than the polar angle, \mathbf{e}_θ points toward the equator in the northern hemisphere as normal in a spherical coordinate system. To understand the origin of the tilt, we consider

an untilted, radially rising flux loop whose leading and following legs are symmetric, and whose tangent vector \mathbf{l} at the apex is parallel to the positive ϕ direction. It is then clear that the θ component of the Coriolis force $f_{c\theta}$ is primarily responsible for generating the tilt. More precisely, it is the *difference* between $f_{c\theta}$ in the leading and the following sides of the apex, as measured by the *gradient*:

$$\left. \frac{\partial f_{c\theta}}{\partial s} \right|_{apex} = 2 \omega \sin \theta \left. \frac{\partial v_\phi}{\partial s} \right|_{apex}, \quad (3.8)$$

that directly causes the tilting of the loop. If $\partial v_\phi / \partial s|_{apex} > 0$, i.e. v_ϕ is divergent at the apex, then equation (3.8) indicates that a gradient of $f_{c\theta}$ will arise that pushes the leading side of the loop equatorward relative to the following side. To determine the sign of $\partial v_\phi / \partial s|_{apex}$, we decompose v_ϕ into the sum of $v_{\perp\phi} \equiv \mathbf{v}_\perp \cdot \mathbf{e}_\phi$ and $v_{\parallel\phi} \equiv v_{\parallel}(\mathbf{l} \cdot \mathbf{e}_\phi)$, where \mathbf{v}_\perp and v_{\parallel} are respectively the components of the velocity that are perpendicular and parallel to the flux tube. Thus,

$$\begin{aligned} \left. \frac{\partial v_\phi}{\partial s} \right|_{apex} &= \left. \frac{\partial v_{\perp\phi}}{\partial s} \right|_{apex} + \left. \frac{\partial v_{\parallel\phi}}{\partial s} \right|_{apex} + v_{\parallel\phi} \left. \frac{\partial l_\phi}{\partial s} \right|_{apex} \\ &= \left. \frac{\partial v_{\perp\phi}}{\partial s} \right|_{apex} + \left. \frac{\partial v_{\parallel\phi}}{\partial s} \right|_{apex}. \end{aligned} \quad (3.9)$$

At the second step, we have used $l_\phi|_{apex} = 1$, $\partial l_\phi / \partial s|_{apex} = 0$, for the untilted flux loop. We find that as the loop rises, the perpendicular component of the buoyancy force stretches the loop and causes its two legs to move apart into the $\pm\phi$ directions, therefore resulting in a diverging $v_{\perp\phi}$ at the apex, i.e. $\partial v_{\perp\phi} / \partial s|_{apex} > 0$. The sign of $\partial v_{\parallel\phi} / \partial s|_{apex}$, on the other hand, is determined by the flow of plasma along the tube,

attempting to reach hydrostatic equilibrium in the parallel direction (see Appendix B). In the deep convection zone, $\partial v_l / \partial s |_{apex}$ is also positive (diverging). However, as the loop enters the *upper* convection zone, where the external temperature gradient becomes significantly superadiabatic, $\partial v_l / \partial s |_{apex}$ becomes negative, i.e. a converging flow sets in. We will show in §3.5.5 that for flux loops with weak field strengths ($B_0 \leq 20$ kG), this converging flow becomes dominant so early in the evolution that the loops emerge with inverse tilts. For loops with $B_0 \geq 30$ kG, the converging flow plays a less significant role and $\partial v_\phi / \partial s |_{apex} > 0$ through most of the convection zone so that the loops emerge with correct tilts. Figure 3.11 shows the variation of v_ϕ along a rising loop (with $B_0 = 30$ kG) at one instant during its evolution. It can be seen that $\partial v_\phi / \partial s |_{apex} > 0$, and that the two legs of the loop are moving apart relative to each other in the $\pm\phi$ directions.

As the loop begins to twist under the influence of the torque produced by the Coriolis force gradient $\partial f_{c\theta} / \partial s |_{apex}$, corresponding gradients of the drag and tension forces, $\partial f_{d\theta} / \partial s |_{apex}$ and $\partial f_{t\theta} / \partial s |_{apex}$ arise to counteract the tilt. (For brevity, we will refer to $\partial f_{c\theta} / \partial s |_{apex}$, $\partial f_{d\theta} / \partial s |_{apex}$, and $\partial f_{t\theta} / \partial s |_{apex}$ as forces for the remainder of §3.5.2, although they are really force gradients.) From examining the simulations, we find that these opposing forces evolve to become comparable to the driving Coriolis force and are therefore important in determining the final tilt angle α of the loop. For those cases where the rise time is relatively short (roughly less than the solar rotation period), the opposing drag force is relatively more important than the tension. On the other hand, when the rise time is very long (a

few times the solar rotation period), the tension is more important than the drag in opposing the Coriolis force. In the following, we carry out a rough estimate of the dependence of the individual forces on field strength, total flux, and the latitude of the loop, in order to understand the variation of the tilt angle with these quantities.

The opposing force from the drag can be estimated as the following:

$$\left. \frac{\partial f_{d\theta}}{\partial s} \right|_{apex} \approx - C_D \frac{v_r}{(\pi\Phi/B)^{1/2}} \frac{\langle v_\theta \rangle_l - \langle v_\theta \rangle_f}{\Delta s}, \quad (3.10)$$

where $\langle v_\theta \rangle_l$ and $\langle v_\theta \rangle_f$ are the averaged v_θ for the leading and the following legs of the loop, Δs can be estimated as half of the total length of the loop, and v_r is the rise speed of the loop. In addition, the growth rate of the tilt angle α is estimated to be

$$\frac{d\alpha}{dt} \approx \frac{\langle v_\theta \rangle_l - \langle v_\theta \rangle_f}{\Delta s}. \quad (3.11)$$

To determine how the tension force responds to the twisting of the loop, we use a very simplified model: consider a straight thin flux tube being deformed in the way illustrated in Figure 3.12. The arrows in the Figure show the direction of the restoring tension forces T_1 and T_2 . At point P, there exists a gradient of the tension force, $\partial T / \partial s|_p$, which tries to reduce the angle α . One can estimate this gradient:

$$\left. \frac{\partial T}{\partial s} \right|_p \approx \frac{T_1 - T_2}{\Delta s} \approx - \frac{B^2}{8\pi\rho} \frac{4\alpha}{\Delta s L}. \quad (3.12)$$

This $\partial T / \partial s|_p$ approximates the opposing tension force, $\partial f_{t\theta} / \partial s|_{apex}$, that arises in response to the tilt angle α of the loop. Here, ρ is the plasma density inside the tube, and L corresponds to the length of one leg of the loop, $L \approx \Delta s$.

Finally, we need to estimate the driving Coriolis force. From equation (3.8), we have

$$\left. \frac{\partial f_{c\theta}}{\partial s} \right|_{apex} \sim 2 \omega \sin \theta \frac{\langle v_\phi \rangle_l - \langle v_\phi \rangle_f}{\Delta s}, \quad (3.13)$$

where $\langle v_\phi \rangle_l$ and $\langle v_\phi \rangle_f$ are the averaged v_ϕ for the leading and the following legs of the loop.

Now consider a balance between the Coriolis force and the drag force. This is a good approximation in the limit of "fast evolution" (rise time less than the solar rotation period). Using equations (3.10), (3.11) and (3.13), the balance between the two forces yields

$$2 \omega \sin \theta \frac{\langle v_\phi \rangle_l - \langle v_\phi \rangle_f}{\Delta s} \sim C_D \frac{v_r}{(\pi\Phi/B)^{1/2}} \frac{d\alpha}{dt}. \quad (3.14)$$

The speed of separation of the two legs, $\langle v_\phi \rangle_l - \langle v_\phi \rangle_f$, should be roughly proportional to the rising speed of the loop v_r :

$$\langle v_\phi \rangle_l - \langle v_\phi \rangle_f \propto v_r. \quad (3.15)$$

Thus, from equations (3.14) and (3.15) we have

$$\frac{d\alpha}{dt} \propto \sin \theta \Phi^{1/2} B^{-1/2}. \quad (3.16)$$

Furthermore, since

$$\frac{d\alpha}{dt} \sim \frac{\alpha}{t_r}, \quad (3.17)$$

equation (3.16) yields

$$\alpha \propto \sin \theta \Phi^{1/2} B^{-1/2} t_r. \quad (3.18)$$

Since $t_r \propto v_r^{-1}$, and we can estimate v_r by considering the balance between the buoyancy and drag forces (see Chapter 2): $B_0^2/(8\pi H_p) = C_D \rho_e v_r^2/(\pi\Phi/B_0)^{1/2}$, we

obtain

$$v_r \propto B^{3/4} \Phi^{1/4}, \quad (3.19)$$

implying

$$\alpha \propto \sin \theta B^{-5/4} \Phi^{1/4}. \quad (3.20)$$

If we approximate θ and B by θ_{em} and B_0 , equation (3.20) gives roughly the correct dependence of the final tilt angle on B_0 , θ_{em} , and Φ , as determined from our simulations.

In the limit of "slow evolution" (i.e. the rise time is much greater than the solar rotation period), our simulations indicate that the opposing tension force is more important than the drag. We therefore consider a balance between the Coriolis and the tension forces:

$$2 \omega \sin \theta \frac{\langle v_\phi \rangle_i - \langle v_\phi \rangle_f}{\Delta s} = \frac{B^2}{8\pi\rho} \frac{4\alpha}{\Delta s L}. \quad (3.21)$$

The separation speed of the legs $\langle v_\phi \rangle_i - \langle v_\phi \rangle_f$ is again given by relations (3.15) and (3.19). Thus, equation (3.21) yields

$$\alpha \propto \sin \theta B^{-5/4} \Phi^{1/4}. \quad (3.22)$$

Coincidentally, the above equation gives the same predicted variation of tilt angle α with B , Φ and θ as does equation (3.20)!

Again, we can approximate B and θ by B_0 and θ_{em} , although we should bear in mind that θ and B in the above scaling relation really represent the effective mean values of latitude and field strength of the loop during its passage through the convection zone. Therefore, for both fast and slow evolution cases,

$$\alpha \propto \sin \theta_{em} B_0^{-5/4} \Phi^{1/4}. \quad (3.23)$$

Although the above analysis is highly simplified and has the nature of a rough dimensional analysis, it gives us insight into why the tilt angle increases with increasing latitude, total flux, and decreases with increasing field strength, as we found from the simulations. For example, consider the variation of α with Φ . In the limit of fast evolution, increasing total flux will (a) increase the growth rate of α , because of a weaker opposing drag force, and (b) reduce the rise time t_r . However, the growth rate $d\alpha/dt$ scales with $\Phi^{1/2}$ (eq. [3.16]), whereas the rise time $t_r \propto v_r^{-1}$ scales with $\Phi^{-1/4}$ (eq. [3.19]); therefore the final tilt angle α scales with $\Phi^{1/4}$, i.e. it increases with Φ . On the other hand, in the limit of slow evolution, where the final tilt angle is mainly determined by the balance between the Coriolis and the tension forces, increasing total flux will increase the rising speed (eq. [3.19]) and hence increases the driving Coriolis force (eq. [3.13] and [3.15]). However, increasing flux does not affect the opposing tension force. Therefore, a larger tilt angle again results from increasing the total flux Φ . In the same fashion, we can understand the dependence of α on B_0 and θ_{em} : Increasing the field strength B_0 results in a faster rising loop and therefore increases the driving Coriolis force. However, it also leads to a stronger opposing drag as well as a stronger opposing tension. The net result is that α decreases with increasing B_0 , as shown in equation (3.23). The tilt angle increases with θ_{em} , simply because the driving Coriolis force is proportional to $\sin \theta$ (see eq. [3.13]).

3.5.3 Comparison of Simple Analysis with Simulations

In this section, we compare the predicted dependence of α on θ_{em} , Φ and B_0 given in the scaling relation (3.23) with the results of simulations. First, we find that if we convert Figure 3.10 into plots of α (in radians) vs. $\sin \theta_{em}$, the resulting curves behave nearly identically to those in Figure 3.10: α generally increases with $\sin \theta_{em}$, as predicted by the simple analysis, although the increase of α with $\sin \theta_{em}$ is not strictly linear.

Second, to compare the $B_0^{-5/4}$ and $\Phi^{1/4}$ dependences given in equation (3.23) with the simulation results, we plot in Figure 3.13(a)-(b) on a log-log scale, $\alpha/\sin \bar{\theta}$ as a function of B_0 and Φ respectively, based on the results of the simulations. Although θ_0 is held fixed in the simulations, θ_{em} varies with both B_0 and Φ . Thus, we divide α by $\sin \bar{\theta}$, with $\bar{\theta} = (\theta_0 + \theta_{em})/2$ approximating the mean latitude of the loop during its passage through the convection zone, in an attempt to remove the effect of varying θ_{em} on the variation of α . The simulation results shown in Figure 3.13 clearly have a more complex dependence on B_0 and Φ than the simple power law of equation (3.23) represented by the straight lines. Nevertheless, we can see that the scaling relation (3.23) provides a good qualitative prediction of the general trend of the variation of α .

One thing worth noting in Figure 3.13(a) is that, at the low field strength end, we begin to see a tendency for the curves of tilt angle to turn downward instead of continuing to go up with decreasing field strength. We will discuss the nature of this tendency in §3.5.5.

Regarding the dependence of α on λ , the simulations indicate that α generally decreases with increasing λ (see Figure 3.10). From the point of view of equation (3.21), increasing λ can lead to an increase of the tilt angle because it reduces the opposing tension force, if L in equation (3.21) is somewhat related to the initial length scale λ . On the other hand, increasing λ reduces the rise time and also increases Δs , and according to equation (3.14), both of these cause the final tilt angle to be smaller. So the simple force balance analysis fails to give an unambiguous answer regarding the dependence of α on λ . It appears that the decrease of rise time and the increase of Δs , which can reduce the growth rate of α (eq. [3.14]), together have the more significant effect, and thus lead to the decrease of tilt angle with increasing λ .

3.5.4 Comparison of Simulations with Observations

A comparison between the tilt angles of emerging loops from our simulations (Figure 3.10) and the observed tilt angles of bipolar active regions shows a fairly good agreement. The magnitude of the computed tilt angles of the loops is certainly within the right range (about 0° to 20°). In addition, the general increase of tilt angle with latitude is consistent with Joy's law, although there exist significant differences among different observational results on how steeply the tilt grows with latitude. For example, the study of Wang & Sheeley (1989, 1991) shows that the average tilt angle increases to about 18° at approximately 35° latitude. A linear least-squares fit to their mean observed tilt angles gives $\sin \alpha = 0.48 \sin \theta_{em}$ (Wang & Sheeley 1991), which is shown as dashed lines in

Figure 3.10. Other studies, however, have shown less steep increases of tilt with latitude. The original measurement of sunspot group tilt angles by Hale et al. (1919) found a mean tilt angle of about 12° near 35° latitude. A recent study by Howard (1991b) of sunspot groups gives an average tilt of only 8° at around 35° latitude. Another study of active regions by Howard (1991a) shows a more complicated behavior, with the tilt angle increasing steadily to a maximum of about 13° near 25° latitude and then falling back to about 5° at roughly 35° latitude. If we are to fit $\sin \alpha = b \sin \theta_{em}$ to these observational results, they translate to values of b that are lower than 0.48, with a minimum of approximately 0.2. Thus we have also plotted (dotted lines) $\sin \alpha = 0.2 \sin \theta_{em}$ in Figure 3.10 to indicate roughly the lower limit of the observed slope of tilt increase with active region latitude.

Overall, we find that our simulation results shown in Figure 3.10 resemble the variation of tilt with latitude presented by Howard (1991a, cf. Fig. 5), in the sense that tilt increases more steeply at lower latitudes, while at higher latitudes, the tilt angle shows a tendency to level off or even decrease. In detailed comparison, Figure 3.10 shows that the curves corresponding to $B_0 = 50$ kG, $\Phi = 10^{22}$ Mx, and $\lambda = 3 \times 10^{10}, 4 \times 10^{10}$ cm agree very well with the dashed lines corresponding to $\sin \alpha = 0.48 \sin \theta_{em}$ of Wang & Sheeley (1991). However, we certainly can not conclude from this that all the toroidal flux tubes at the base of the convection zone have a field strength of $B_0 = 50$ kG. The differences between different observations of the variation of tilt with latitude are sufficiently large to enclose the

simulation results for nearly the entire field strength range $30 \text{ kG} \leq B_0 \leq 90 \text{ kG}$. We do find, however, that the results for $B_0 = 30 \text{ kG}$ deviate most strongly from a linear increase of α with θ_{em} , and in some cases become incompatible with the observations.

The dependence of α on Φ predicted by the scaling relation (23) can be tested by observations. However, the observational results on the relationship between region tilt angles and fluxes are still very uncertain. In Figure 3.6a of Wang & Sheeley (1989), the average tilt angles for strong ($\Phi \geq 5.0 \times 10^{21} \text{ Mx}$), medium ($5.0 \times 10^{21} \text{ Mx} \geq \Phi \geq 2.0 \times 10^{21} \text{ Mx}$), and weak ($\Phi \leq 2.0 \times 10^{21} \text{ Mx}$) bipolar magnetic regions (BMRs) are shown as a function of latitude. It can be seen from their Figure that there are no significant differences between the average tilt angles of BMRs with different fluxes, inconsistent with the increase of average tilt with increasing flux suggested by our simulations. In addition, the observed tilt angles of weaker BMRs tend to have a wider scatter than those of stronger BMRs, and thus lead to larger r.m.s tilts for weaker BMRs, as shown in Figure 6b of Wang & Sheeley (1989). The larger scatter of tilt angle values for lower flux active regions can be explained by the drag force from convective motions, which acts more strongly on tubes with smaller Φ than those with larger Φ . Howard (1991a) also studied the relation between the active region flux and tilt angle. He plotted (Figure 6 of Howard 1991a) the average magnetic flux per region as a function of tilt angle and concluded that the larger regions have the smallest tilt angles, which is opposite to the prediction of our simulations. However, some recent indirect measurements

seem to support our simulation result on the Φ dependence of α . Howard (1993) found that active regions with larger polarity separations have larger tilt angles. In the meantime, another observation by Howard (1992) showed that total flux and polarity separation of active regions are correlated, with flux increasing almost linearly with polarity separation. These two observations together suggest that tilt angles are larger for regions with larger total fluxes, consistent with our prediction. Thus, there is conflicting evidence concerning the correlation between active region tilt angles and fluxes, and further observational tests are needed.

The multiple loop simulations carried out by D'Silva & Choudhuri (1993) found that the computed tilt angles match the observations only if the initial toroidal field strength lies in the range between 60 kG and 160 kG, with 100 kG fitting the observational result of Wang & Sheeley (1989, 1991) most closely. Field strengths stronger than 160 kG lead to tilts too small in magnitude compared to observations, while field strengths smaller than 60 kG result in loops emerging at very high latitudes and tilt angles that disobey the Joy's law. Our single emerging loop simulations, however, find that tilts from loops with B_0 ranging from 30 kG to 90 kG are all consistent with observations. The high field strengths (~ 100 kG) recommended by D'Silva & Choudhuri (1993) seem to give tilt angles that are too small according to our calculations.

3.5.5 Inverse Tilts of Weak Field Strength Flux Loops

It is interesting to note how the tilt angle changes as the toroidal field strength B_0 drops below 30 kG, as shown in Figure 3.14. We find that the tilt angle begins to drop sharply with decreasing B_0 when $B_0 \leq 30$ kG, and when $B_0 \leq 20$ kG, loops become inversely tilted. Figure 3.15 shows the variation of latitude with depth, along an emerging loop with initial field $B_0 = 10$ kG. In the deeper portion of the convection zone, the leading leg is still closer to the equator than the following leg, but above a certain depth the tilt is reversed. The magnitude of the inverse tilt angle at emergence can be greater than 90° for loops with $B_0 = 10$ kG (Figure 3.14), meaning active regions which violate the Hale's polarity laws may be formed from these loops.

The inverse tilts for weak flux loops can be understood by considering the $\partial v_l / \partial s |_{apex}$ term in equation (3.9), which corresponds to the parallel flow inside the tube as a result of the tube plasma trying to reach hydrostatic equilibrium (hereafter HE). We know that due to the perpendicular component (perpendicular to the tube) of the buoyancy force stretching the flux loop and separating the leading and following legs, the term $\partial v_{\perp\phi} / \partial s |_{apex}$ in equation (3.9) is always positive, and therefore contributes to a divergence of v_ϕ at the apex of the loop. The Coriolis force resulting from this divergence of v_ϕ twists the loop into the correct tilt (see eq. [3.8]). In the meantime, as discussed in the Appendix, the parallel velocity v_l induced to establish HE along the tube is also divergent at the apex ($\partial v_l / \partial s |_{apex} > 0$) when the loop is in the deep convection zone, where the

temperature stratification is nearly adiabatic. This diverging flow therefore adds to the divergence of v_ϕ at the apex. However, when the loop enters the upper convection zone, where the external plasma becomes significantly superadiabatic, a strong converging parallel flow ($\partial v_l / \partial s|_{apex} < 0$) sets in to establish HE, which contributes to a converging v_ϕ at the apex. We find from the simulations, as well as the analytical calculation of $\partial v_l / \partial s|_{apex}$ given in the Appendix, that for flux loops with weaker field strengths, the converging parallel flow becomes dominant earlier (at greater depths). For loops with $B_0 \leq 20$ kG, the converging flow reverses the direction of the twisting Coriolis force at such substantial depths that this reversed force significantly reduces the tilt of the loop developed earlier in its evolution, and can even generate an inverse tilt angle upon emergence. For stronger flux loops ($B_0 \geq 30$ kG), however, the converging parallel flow becomes dominant only when the loop is much closer to the photosphere, so that the tilt angles developed earlier in its evolution are not significantly altered upon emergence. The inverse tilts for weak field strength ($B_0 \leq 20$ kG) loops suggest that the toroidal flux tubes which give rise to the great majority of active regions probably have field strength $B_0 \geq 30$ kG.

3.6. The Effects of Differential Rotation

To determine the effects of differential rotation on the dynamics of emerging flux loops, we carry out simulations incorporating the helioseismologically inferred differential rotation rate in the convection and radiative zones. In our simulations,

the differential rotation acts as a large scale external velocity field which affects the motions of flux tubes through the drag force. Thus the modification of the model required is to replace the drag force term in the equation of motion (the last term in eq. [3.1]) by

$$-\frac{C_D}{2\sqrt{\pi}\Phi} \frac{\rho_e \sqrt{B} |(\mathbf{v} - \mathbf{v}_e)_\perp| (\mathbf{v} - \mathbf{v}_e)_\perp}{\rho}, \quad (3.24)$$

where \mathbf{v} is the velocity of the flux tube and \mathbf{v}_e is the velocity of the external flow due to differential rotation. Both \mathbf{v} and \mathbf{v}_e are determined with respect to the reference frame rotating at an angular velocity ω_0 , whose magnitude is $\omega_0 = 2.73 \times 10^{-6} \text{ rad s}^{-1}$, which is the approximate rotation rate of the radiative interior of the Sun (see e.g. Dziembowski, Goode, & Libbrecht 1989; Brown et al. 1989; Goode et al. 1991). Thus, the Coriolis force term in the equation of motion (the first term on the right hand side of eq. [3.1]) becomes $-2\omega_0 \times \mathbf{v}$, and the external velocity field \mathbf{v}_e can be expressed as:

$$\mathbf{v}_e = r \cos\theta (\omega - \omega_0) \mathbf{e}_\phi, \quad (3.25)$$

where ω is the solar rotation rate.

According to the prevailing interpretation of rotational splitting data from helioseismology (see e.g. Dziembowski, Goode, & Libbrecht 1989; Brown et al. 1989; Goode et al. 1991), the rotation rate ω in the bulk of the convection zone does not vary with depth, but depends on latitude only (except perhaps in a very thin layer near the top of the convection zone; Korzennik 1990). In other words, the latitudinal differential rotation rate at the surface of the Sun persists essentially all the way to the base of the convection zone. The radiative interior, on the other

hand, appears to rotate nearly rigidly at a constant rate ω_0 , which equals the rate at approximately 35° latitude in the convection zone. Using the result of Brown et al. (1989) as a guide, we adopt the following to approximate the solar rotation rate ω :

$$\omega = \begin{cases} \omega_1 - \omega_2 \sin^2 \theta - \omega_3 \sin^4 \theta & r > r_c, \\ \omega_0 & r < r_c - \delta r, \end{cases} \quad (3.26)$$

where $\omega_1 = 2.88 \times 10^{-6} \text{ rad s}^{-1}$, $\omega_2 = 3.61 \times 10^{-7} \text{ rad s}^{-1}$, $\omega_3 = 4.34 \times 10^{-7} \text{ rad s}^{-1}$, and r_c is the radius of the base of the convection zone. Immediately beneath the base of the convection zone, we add a transition layer of thickness $\delta r = 10^9 \text{ cm}$, in which ω is computed through a linear interpolation in radius between the upper and lower boundaries. The initial conditions and parameters for the perturbed toroidal flux rings remain the same as those described in §3.2. The toroidal rings are assumed to be initially co-rotating with the radiative core.

Figure 3.16(a) shows (solid curves) the evolution of a perturbed toroidal flux ring in the presence of differential rotation, as viewed from the north pole. In this example, $B_0 = 30 \text{ kG}$, $\theta_0 = 5^\circ$, $\Phi = 10^{22} \text{ Mx}$, and $\lambda = 4 \times 10^{10} \text{ cm}$. An emerging flux loop arises from the perturbed segment of the toroidal ring, as in the solid-body case. For comparison, we show in the same Figure the evolution of the perturbed toroidal ring (dash-dotted curves) assuming solid-body rotation; a comparison of the two cases indicates the amount of distortion that differential rotation produces in the final emerging loop. The comparison shows that the distortion is not great. The emerging loop in the differential rotation case is slanted toward the direction of rotation relative to the loop in the solid-body case.

According to the differential rotation profile described in equation (3.26), the perturbed segment of a toroidal ring with $\theta_0 \leq 30^\circ$ experiences a rapid increase of rotation rate of the surrounding fluid as it enters the convection zone from below. This increase imparts an additional drag force on the rising loop in the direction of rotation, so that the final emerging loop slants more toward the direction of rotation. Furthermore, the rising flux loop gains additional angular momentum because of the increased drag force it experiences toward the direction of rotation. We therefore expect a decrease of the emerging latitude of the loop in comparison with that in the solid-body case. Indeed we see in Figure 3.16(b), which shows the trajectories of the loop apex in the meridional plane for both cases, that the emerging latitude is lower with differential rotation.

Figure 3.17 shows an extensive comparison of the latitude of emergence by overlaying θ_{em} obtained from simulations assuming solid-body rotation (dashed lines) with those obtained from simulations with differential rotation included (solid lines). In all cases studied, differential rotation reduces the emerging latitude θ_{em} so that it reflects more closely the initial latitude θ_0 . The difference in θ_{em} between the solid-body and differential rotation cases is more significant for smaller θ_0 , and decreases with increasing θ_0 . As θ_0 increases to 30° , we find that θ_{em} with differential rotation essentially converges with the solid-body case. This variation is easily understood because as θ_0 increases from 0° to 30° , the rotation rate of the convection zone becomes closer to that of the radiative interior, and therefore loops entering the convection zone experience a smaller increase of the drag force.

In §3.4 we discussed the possibility of reproducing all the active region latitudes seen in the observed butterfly diagram. We found that flux eruption of toroidal magnetic field with 30 kG field strength would produce a noticeable equatorial gap (extending from the equator to at least $\pm 5^\circ$ latitude) devoid of active region emergence. However, the further reduction of θ_{em} as a result of including differential rotation causes this gap to be reduced and become negligible. Therefore, it becomes possible for an equatorward propagating dynamo wave of toroidal magnetic field as weak as 30 kG to reproduce the observed butterfly diagram at the surface through flux eruption.

The effect of differential rotation on tilt angles of emerging flux loops is also studied by comparing α from simulations of both the solid-body and differential rotation cases. Figure 3.18 shows α as a function of θ_{em} computed from simulations including differential rotation. When compared with Figure 3.10, we find that although the individual values of α may differ by a few degrees from the solid-body case, overall, the qualitative behaviors of the tilt angles remain unchanged. The values of α are still within the range of the observed active region tilt angles, and the variation of α with θ_{em} , B_0 and Φ are in general the same as was found in the solid-body case. Therefore, differential rotation does not seem to play a significant role in determining the tilt angles of emerging flux loops.

Overall, we find that the changes induced by including differential rotation are not substantial and in most cases can be described as "small perturbations" on the solid-body results. Furthermore, it is worth noting that in the presence of

differential rotation, the field strength asymmetry between the leading and the following legs of the final emerging loop remains essentially the same as in the solid-body case, and that the distortion on the final emerging loop produced by the differential rotation is small, as can be seen from Figure 3.16(a). This confirms the conclusion reached in Chapter 2 concerning the origin of the observed morphological asymmetries in bipolar active regions.

3.7. Summary of Emerging Loop Dynamics

We have applied the numerical model of flux tube dynamics described in Chapter 2 to study the nonlinear evolution of single emerging magnetic flux loops. Each emerging loop arises from a small radial perturbation of one segment (with length scale λ) of a toroidal flux ring lying just beneath the solar convection zone. In contrast, previous numerical simulations imposed a periodic wave pattern on the initial toroidal ring, so that multiple loops emerge simultaneously. We show that the emergence of single magnetic flux loops from toroidal flux rings, presumably generated by a dynamo mechanism near the base of the convection zone, can reproduce several important observed properties of active regions at the surface:

1) *The butterfly diagram*

Our simulations show that loops with an initial field strength B_0 ranging from 30 kG to 90 kG and an initial latitude less than 30° all emerge within the observed active region latitudes. Furthermore, the emerging latitude θ_{em} decreases monotonically with decreasing initial latitude θ_0 , so that an equatorward propagating

dynamo wave will lead to an equatorward migrating band of flux eruption. If solid-body rotation is assumed, then in order to reproduce all the active region latitudes seen in the butterfly diagram, and in particular, to explain those few active regions that emerge within a few degrees of the equator, toroidal flux tubes with B_0 as large as 60 kG are necessary. However, with the inclusion of differential rotation, θ_{em} is further reduced, so that toroidal flux tubes with B_0 as weak as 30 kG can erupt within a few degrees of the equator.

2) The morphological asymmetry

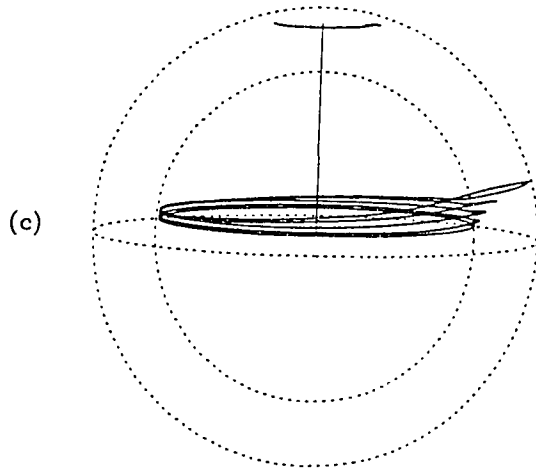
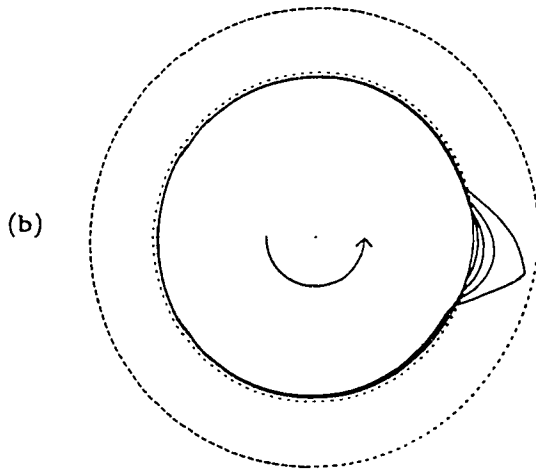
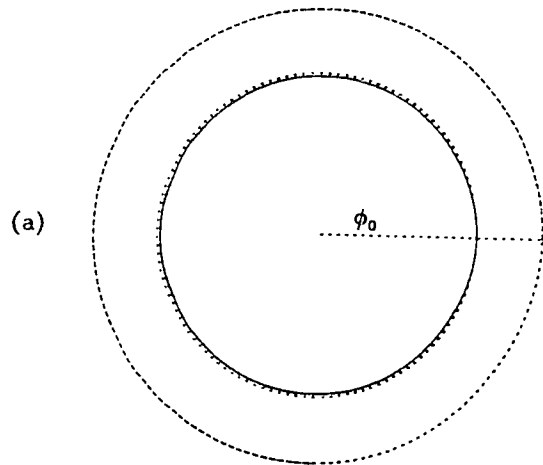
In agreement with Chapter 2, we continue to find that the field strength of the leading leg of each emerging loop is about twice that of the following leg at all depths in the convection zone. This field strength asymmetry, as discussed in Chapter 2, provides a natural explanation of the more compact and longer lived nature of the leading polarity of an active region as compared to its following polarity. Furthermore, because the field strength asymmetry is caused by a transport of mass from the leading leg to the following leg of the loop, we suggest that this flow may be observable as an asymmetry in the vertical velocities of the two polarities of an active region early in its formation, when flux emergence is still occurring.

3) The axial tilt angles of active regions

The Coriolis force originating from the diverging v_ϕ at the apex of a rising loop acts to twist the loop and causes a tilt relative to the azimuthal (east-west) direction as the loop emerges. The tilt angles α computed from our simulations can

reproduce the sign, magnitude, and the latitudinal variation of the observed active region tilt angles. For example, the parameters $B_0 = 50$ kG and $\Phi = 10^{22}$ Mx seem to do a good job of reproducing the least-squares fit to the observational data by Wang & Sheeley (1991). The high field strengths (~ 100 kG) suggested by D'Silva & Choudhuri (1993) seem to give tilt angles that are too small in our own calculations. The increase of α with Φ predicted by our simulations can be tested by observations. However, existing observational results regarding the correlation between active region tilt angles and fluxes are still uncertain. Inclusion of differential rotation in our simulations does not alter the qualitative behavior of the tilt angle of emerging loops. Finally, loops with initial toroidal field strengths $B_0 \leq 20$ kG emerge with tilt angles that are opposite from those of most active regions, suggesting that toroidal flux tubes which give rise to the great majority of active regions probably have a field strength $B_0 \geq 30$ kG.

Figure 3.1 The emergence of a single magnetic flux loop from a perturbed toroidal flux ring. (a) The initial configuration of the perturbed toroidal ring lying slightly beneath the base of the convection zone, at 5° latitude, viewed from the north pole of the Sun. A segment of the ring centered at $\phi_0 = 0^\circ$ is displaced upward into the convection zone. The length of the perturbed segment is $\lambda = 4 \times 10^{10}$ cm. The flux ring has a total flux $\Phi = 10^{22}$ Mx and a field strength $B_0 = 30$ kG. The subsequent evolution of the perturbed toroidal ring is shown in (b) and (c), as viewed from the north pole, and from 5° above the equator, respectively. The configurations of the ring at 5 instants during its evolution are shown as solid curves. The arrow shows the direction of solar rotation. The inner and the outer dotted circles mark, respectively, the base of the convection zone and the photosphere.



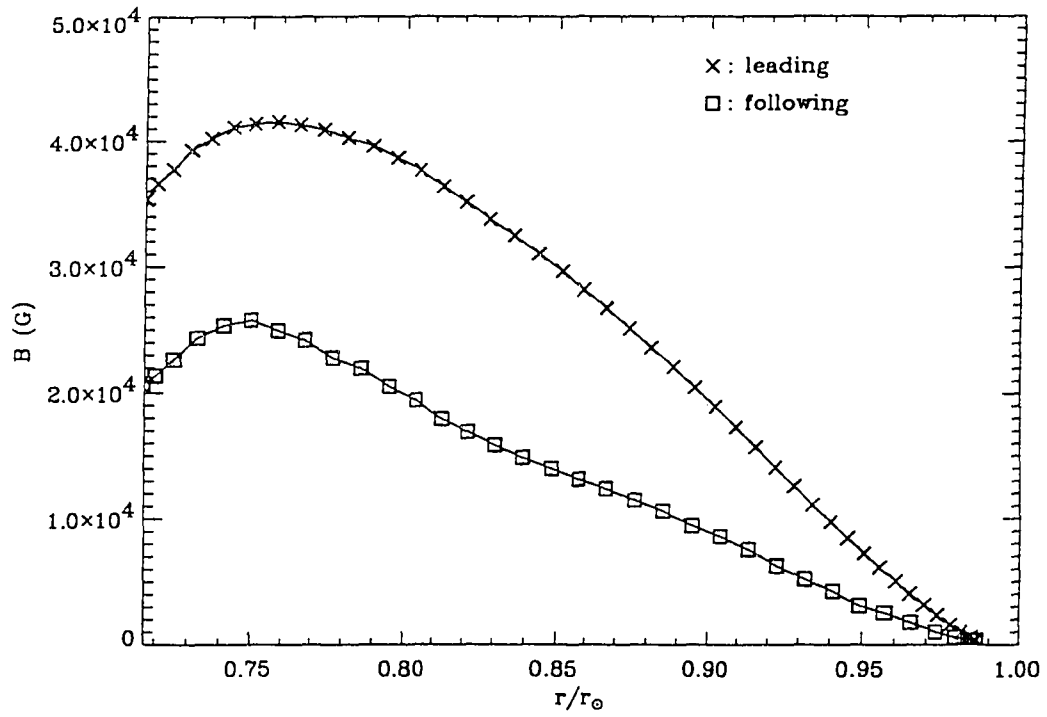
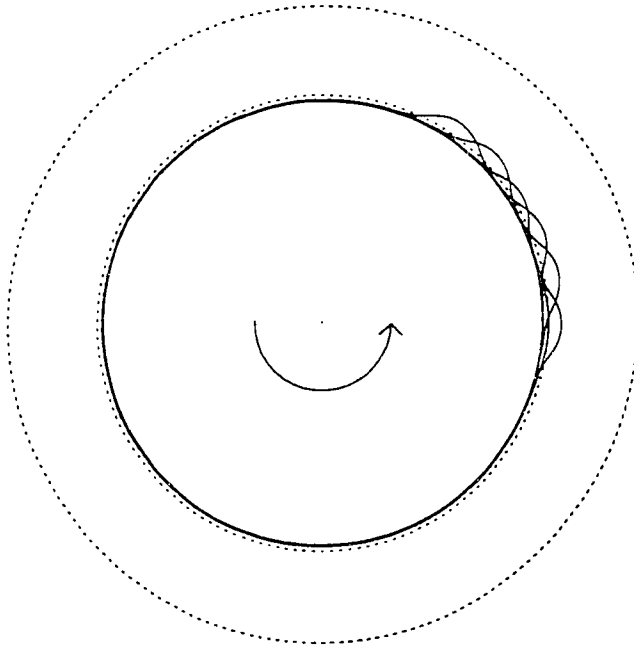


Figure 3.2 The variation of magnetic field strength along the emerging loop, as a function of depth throughout the convection zone. The field strength of the leading leg of the loop is approximately twice that of the following leg at any chosen depth.

Figure 3.3 Evolution of a perturbed toroidal ring with the length scale of the perturbed segment λ less than the critical value λ_c . The configuration of the ring at 7 uniformly spaced, consecutive instants during a total period of 2.5 years is shown in solid curves, as viewed from (a) the north pole, and from (b) 10° above the equatorial plane. In this example, $\lambda = 2 \times 10^{10}$ cm, $\theta_0 = 1^\circ$, $B_0 = 30$ kG, and $\Phi = 10^{22}$ Mx.

(a)



(b)

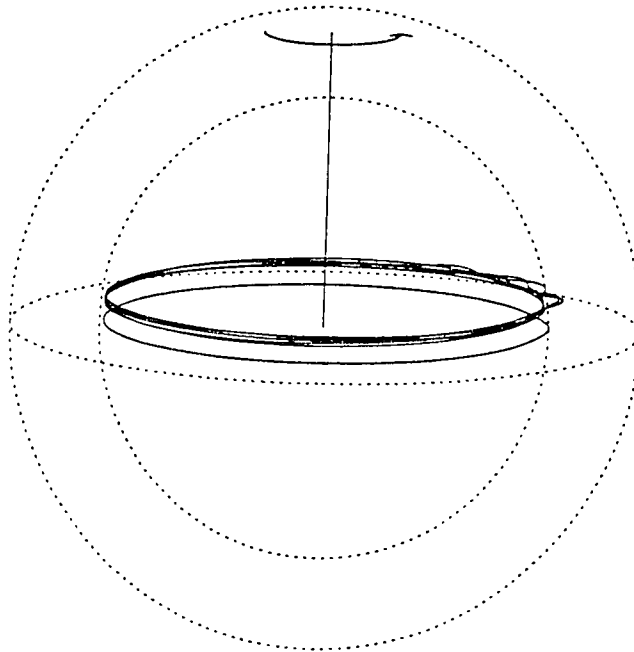
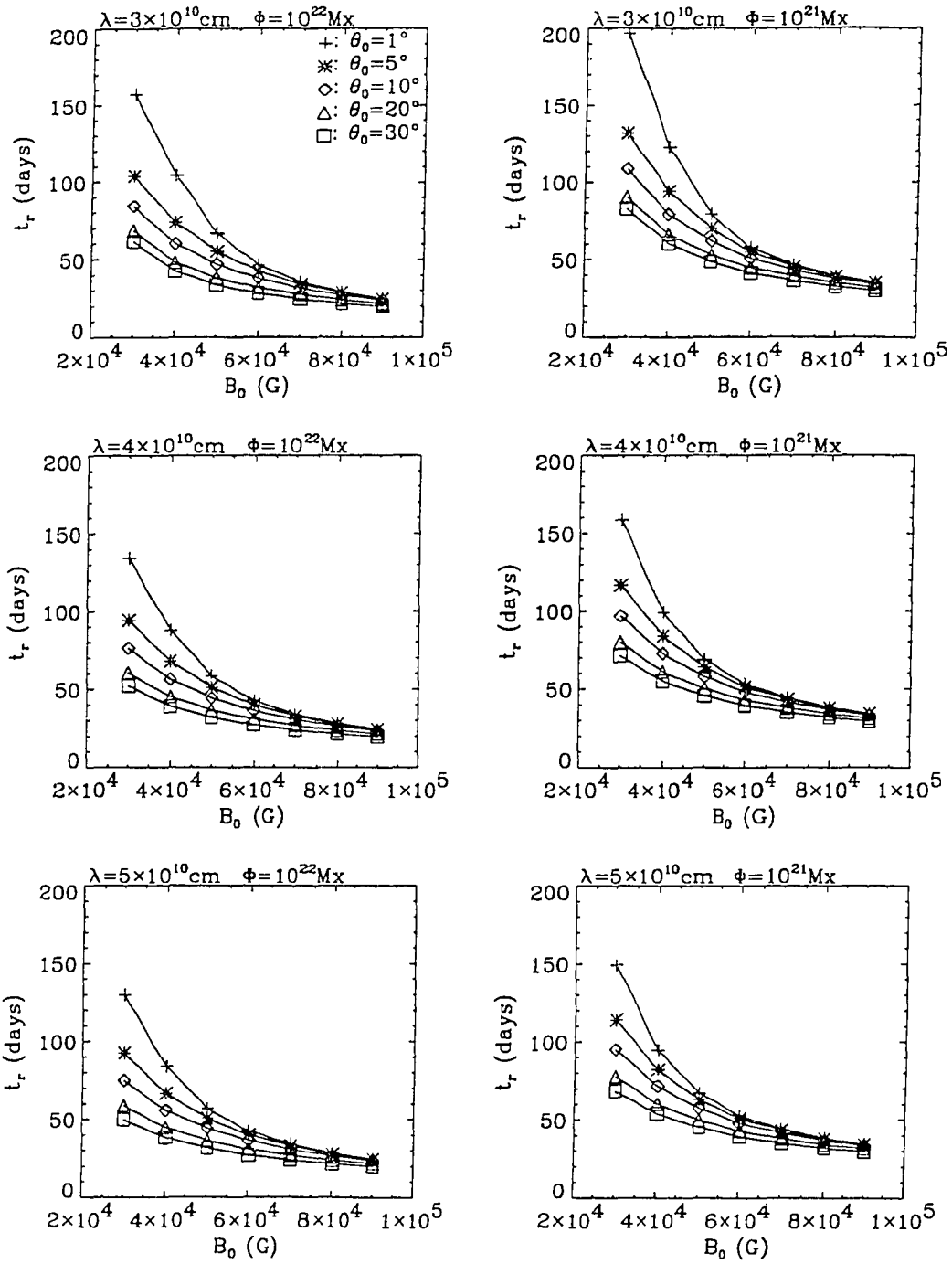


Figure 3.4 The rise time t_r of emerging flux loops with different initial parameters B_0 , θ_0 , Φ , and λ .



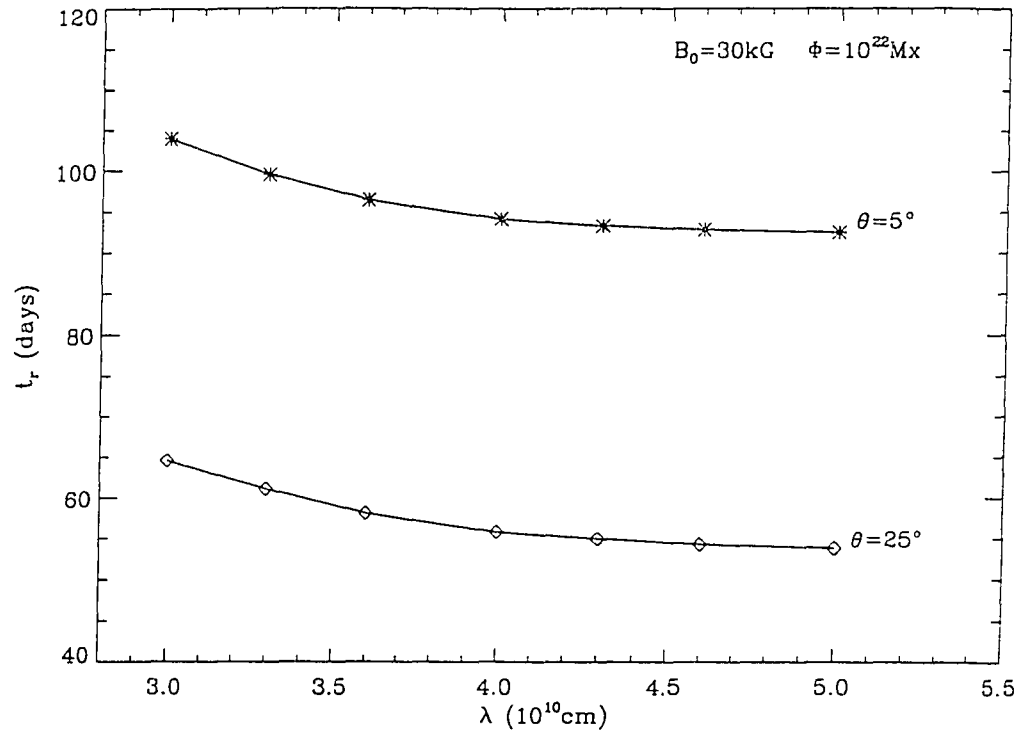


Figure 3.5 The variation of rise time t_r with the length of the perturbed segment λ , for loops with fixed values of B_0 , θ_0 , and Φ .

Figure 3.6 The latitude of emergence θ_{em} for loops with different initial parameters B_0 , θ_0 , Φ and λ , obtained from simulations assuming solid-body rotation.

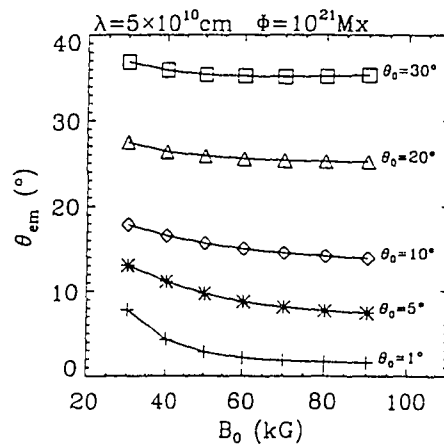
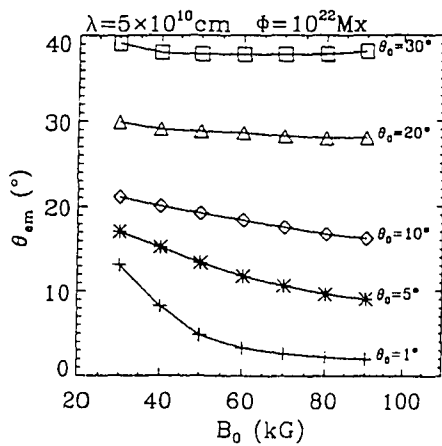
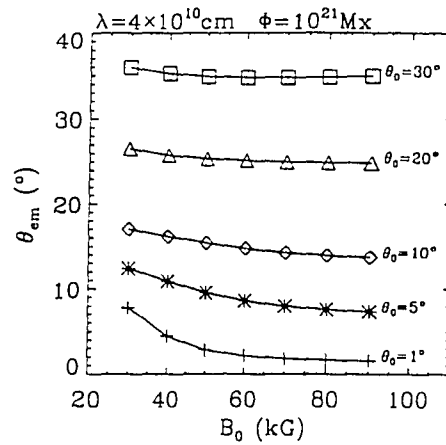
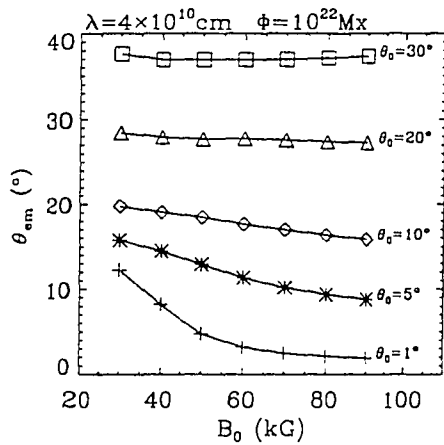
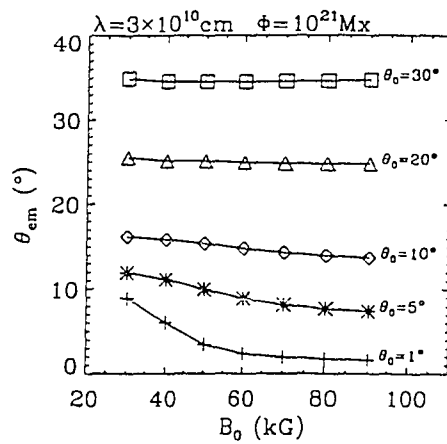
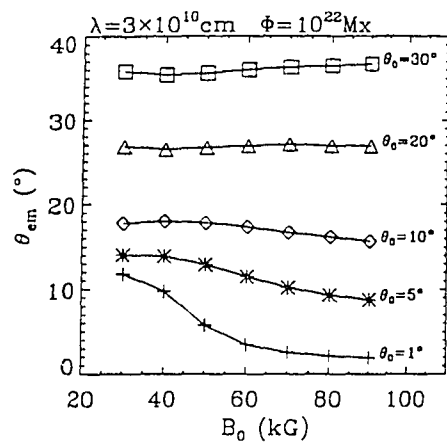


Figure 3.7 The emerging latitude θ_{em} obtained in Chapter 2 (dashed lines) from simulations of multiple ($m = 4$) emerging loops in comparison with θ_{em} obtained in this Chapter (solid lines) from simulations of single emerging loops with $\lambda = 4 \times 10^{10}$ cm. The length scale for each of the upward perturbed segments in the multiple loop case in Chapter 2 is $\lambda = \pi r_c \cos \theta_0 / m = 3.4 \times 10^{10}$ cm to 3.9×10^{10} cm, for $\theta_0 = 1^\circ$ to 30° . Here $r_c = 4.99 \times 10^{10}$ cm is the radius of the base of the convection zone.

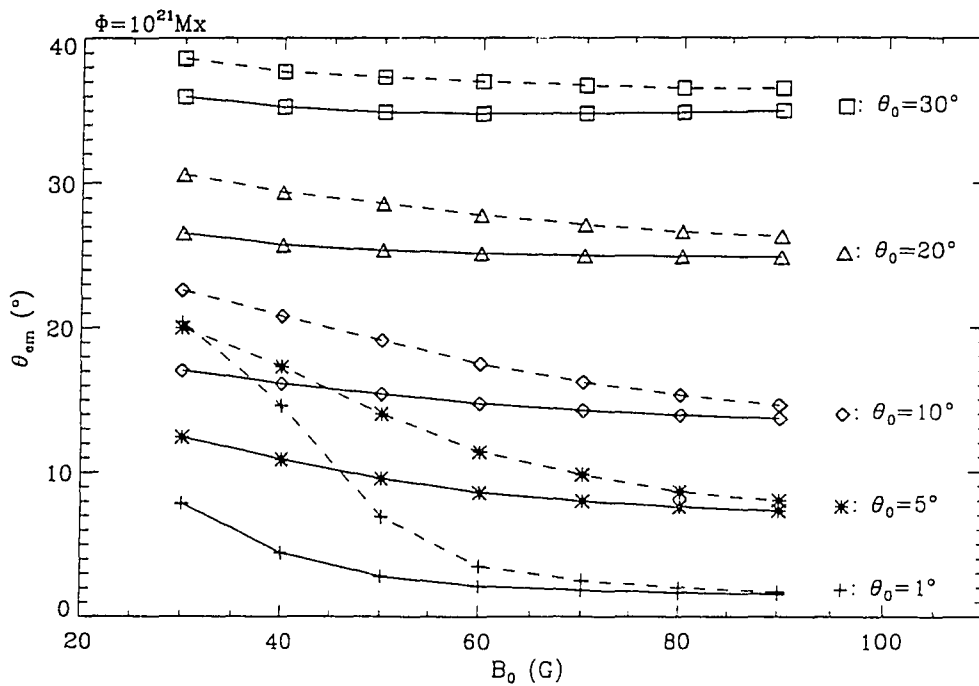
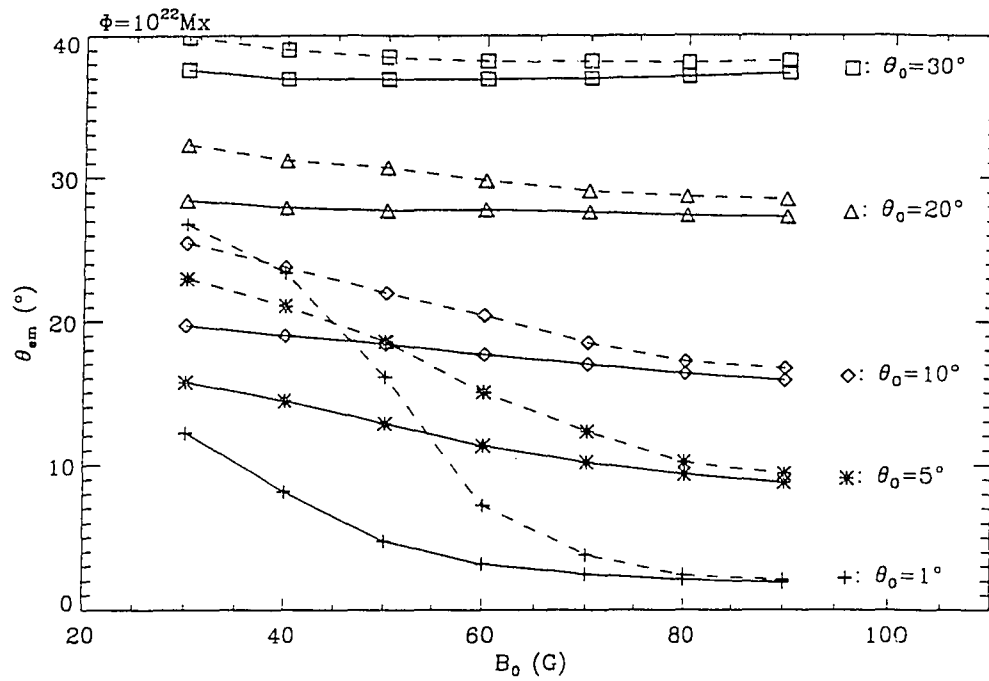
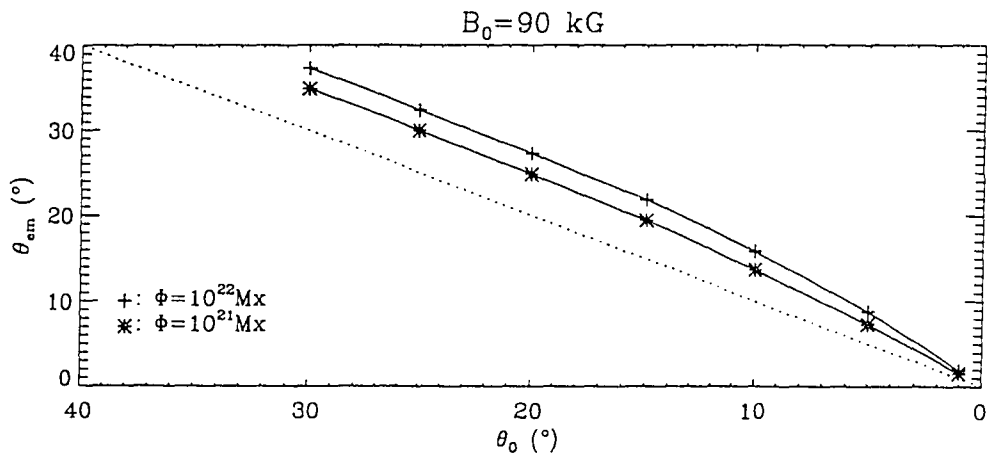
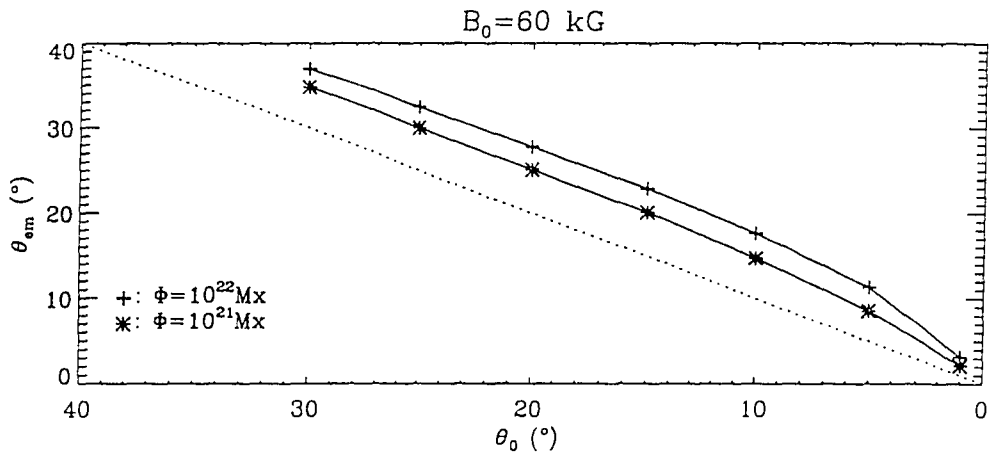
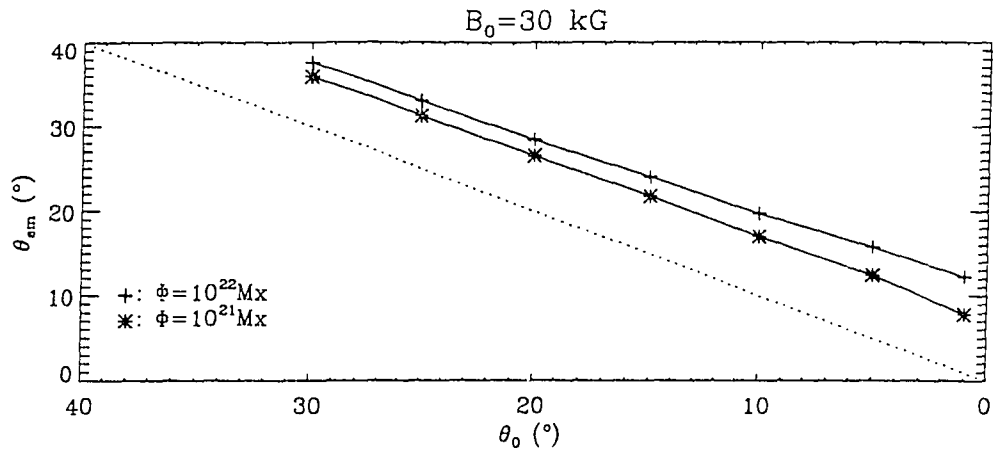


Figure 3.8 The variation of the emerging latitude θ_{em} as a function of the initial latitude θ_0 for loops with various initial field strengths B_0 and total flux Φ , based on results from simulations assuming solid-body rotation.



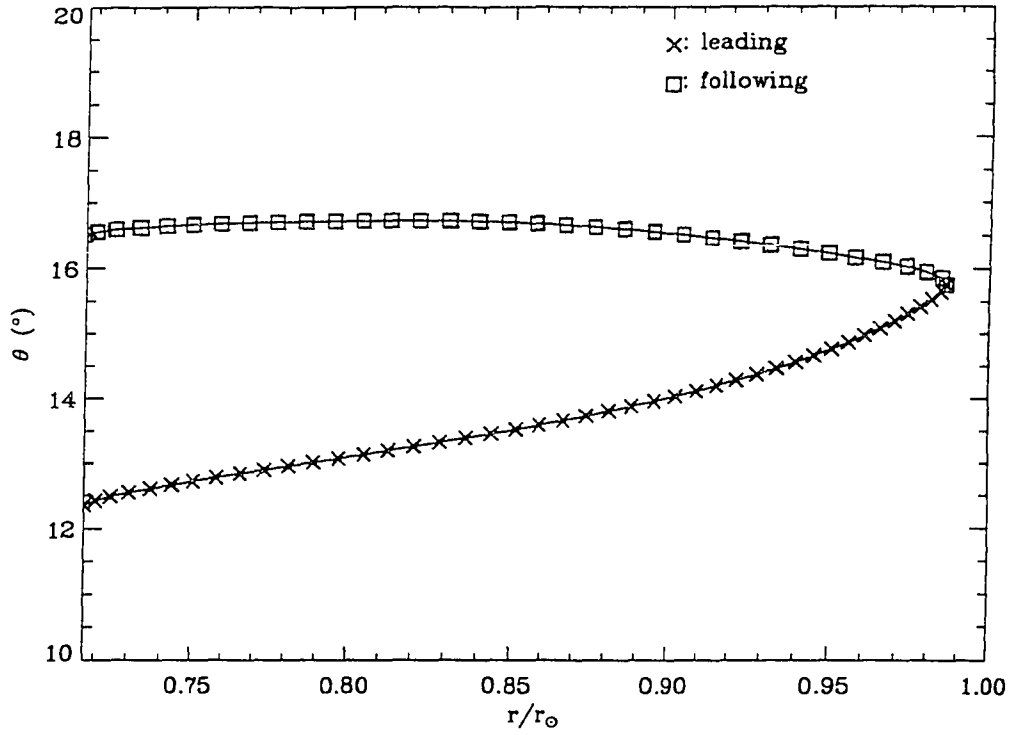
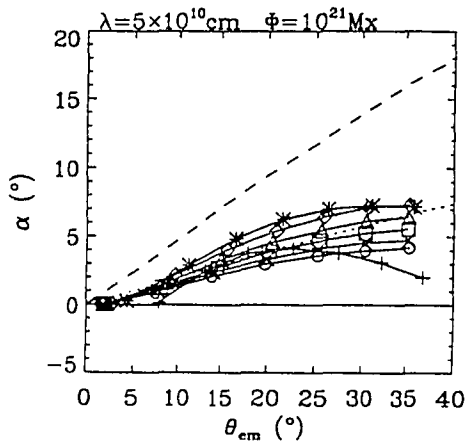
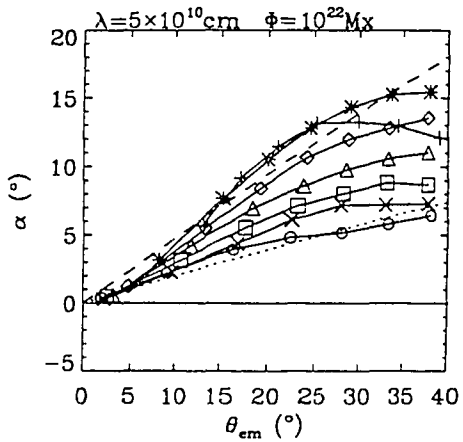
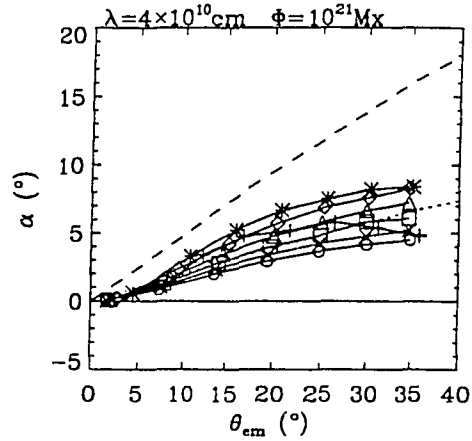
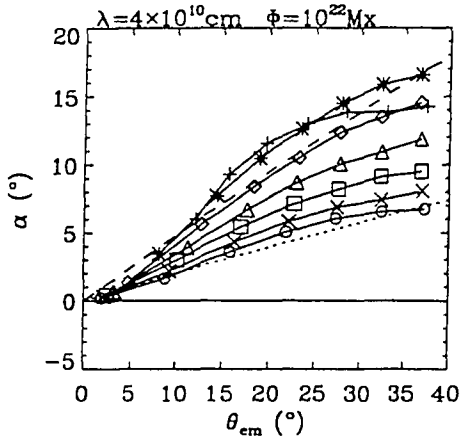
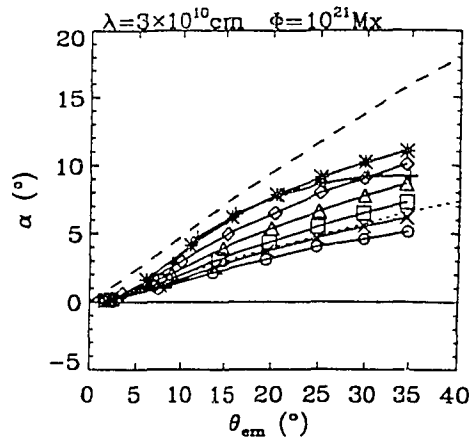
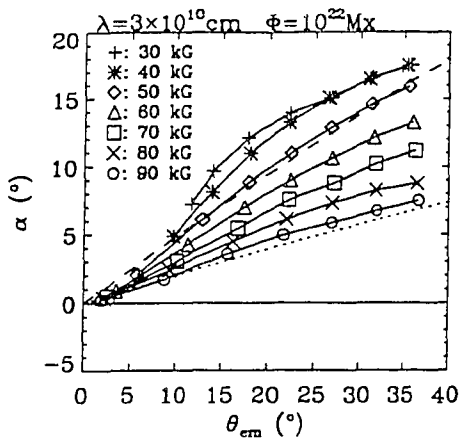


Figure 3.9 The variation of latitude θ along an emerging loop as a function of depth, resulting from the simulation with $B_0 = 30$ kG, $\Phi = 10^{22}$ Mx, $\theta_0 = 5^\circ$ and $\lambda = 4 \times 10^{10}$ cm. It shows that the leading leg of the emerging loop is tilted equatorward relative to the following leg.

Figure 3.10 The tilt angle α of emerging loops as a function of the emerging latitude θ_{em} , computed from simulations with different initial parameters B_0 , Φ and λ , and assuming solid-body rotation of the Sun. The dashed lines correspond to $\sin \alpha = 0.48 \sin \theta_{em}$, which is the linear least square fit to the mean observed tilt angles of active regions, from Wang and Sheeley (1991). The dotted lines correspond to $\sin \alpha = 0.2 \sin \theta_{em}$, which indicates roughly the lower limit of the observed slope of tilt increase with active region latitude.



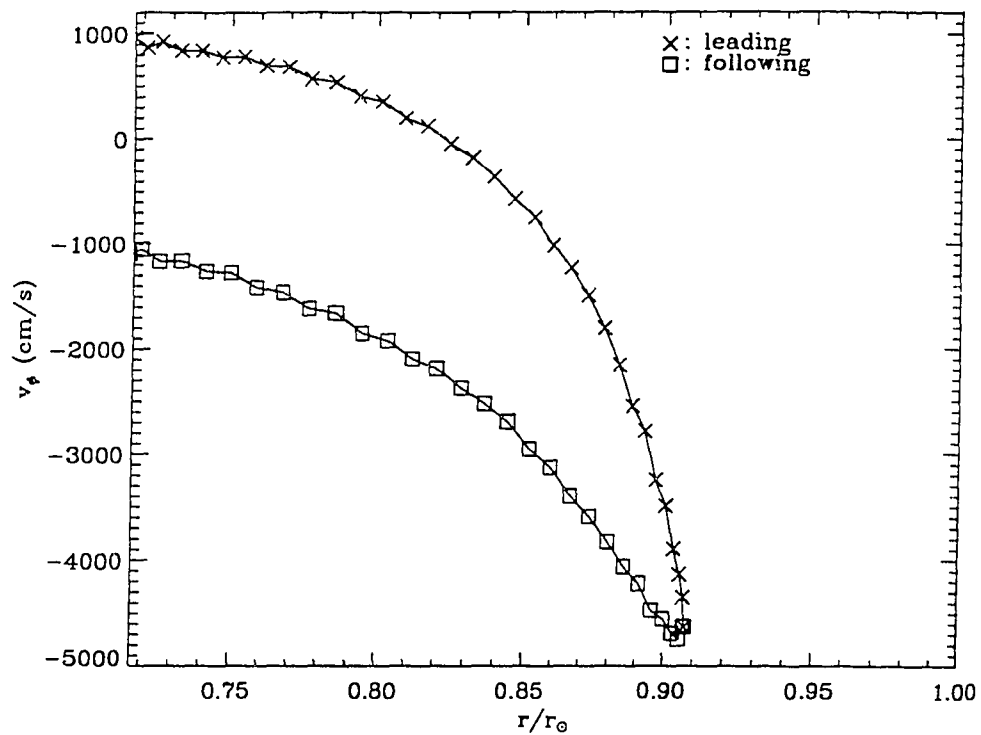


Figure 3.11 The variation of v_ϕ along a rising loop as a function of depth, showing that the ϕ velocity at the apex of the loop is divergent, i.e. $\partial v_\phi / \partial s|_{apex} > 0$.

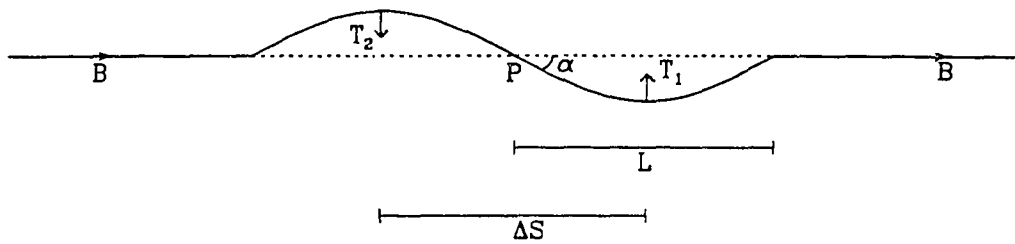
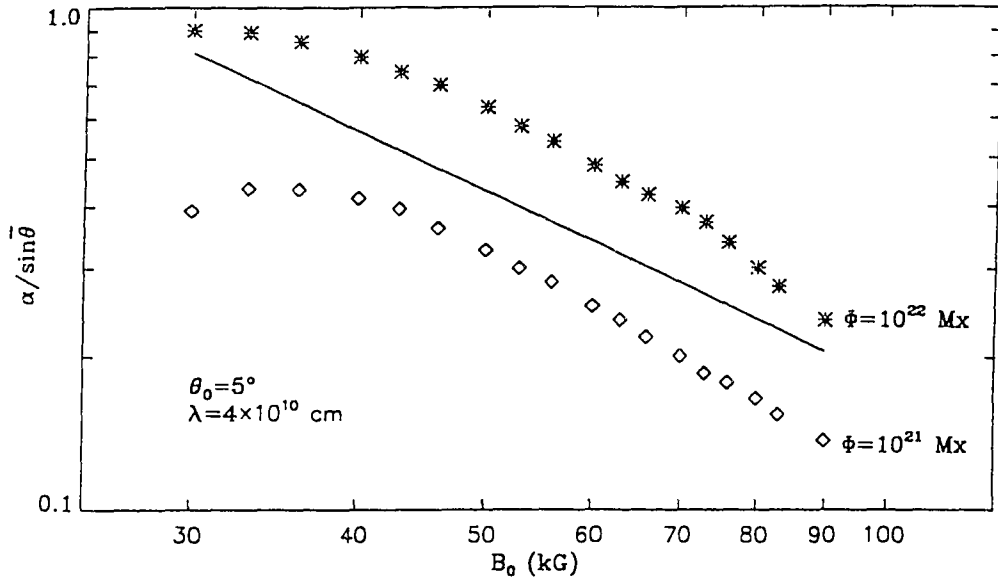
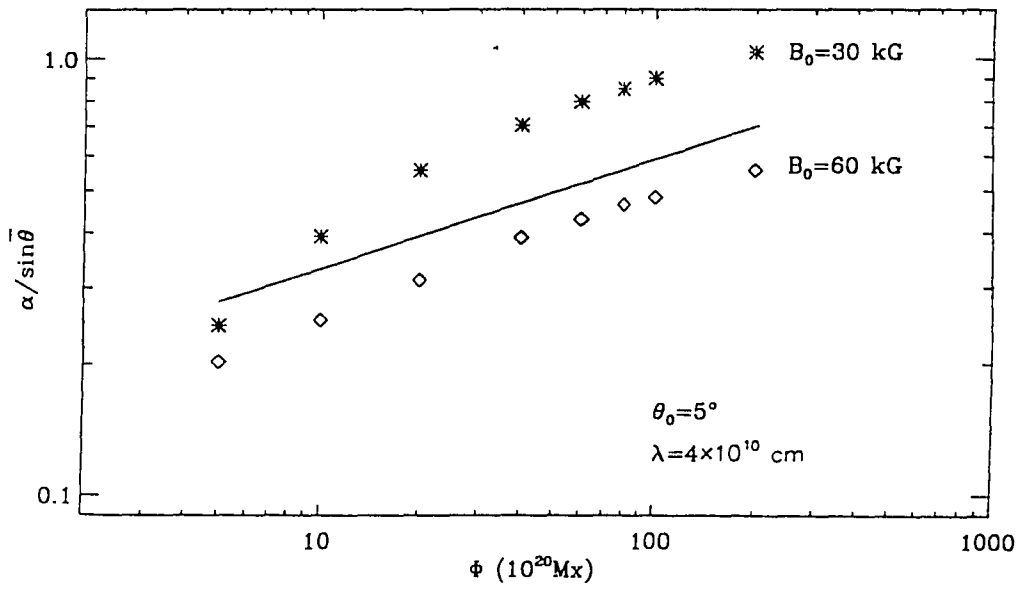


Figure 3.12 A straight magnetic thin flux tube is deformed as shown. Restoring tension forces (force per unit mass) T_1 , T_2 arise in response to the deformation. When α is small, $|T_1| = |T_2| \sim (B^2/8\pi\rho) 2\alpha/L$, where B is the field strength, and ρ is the tube plasma density. At point P, the effect of the tension forces T_1 and T_2 is to reduce the angle α .

Figure 3.13 The variation of $\alpha/\sin\bar{\theta}$ with (a) B_0 and (b) Φ , obtained from the simulations, in comparison with the scaling relations (the straight lines) $\alpha/\sin\bar{\theta} \propto B_0^{-5/4}$ and $\alpha/\sin\bar{\theta} \propto \Phi^{1/4}$. Here $\bar{\theta} = (\theta_{em} + \theta_0)/2$ approximates the mean latitude of the loop apex during its passage through the convection zone.



(a)



(b)

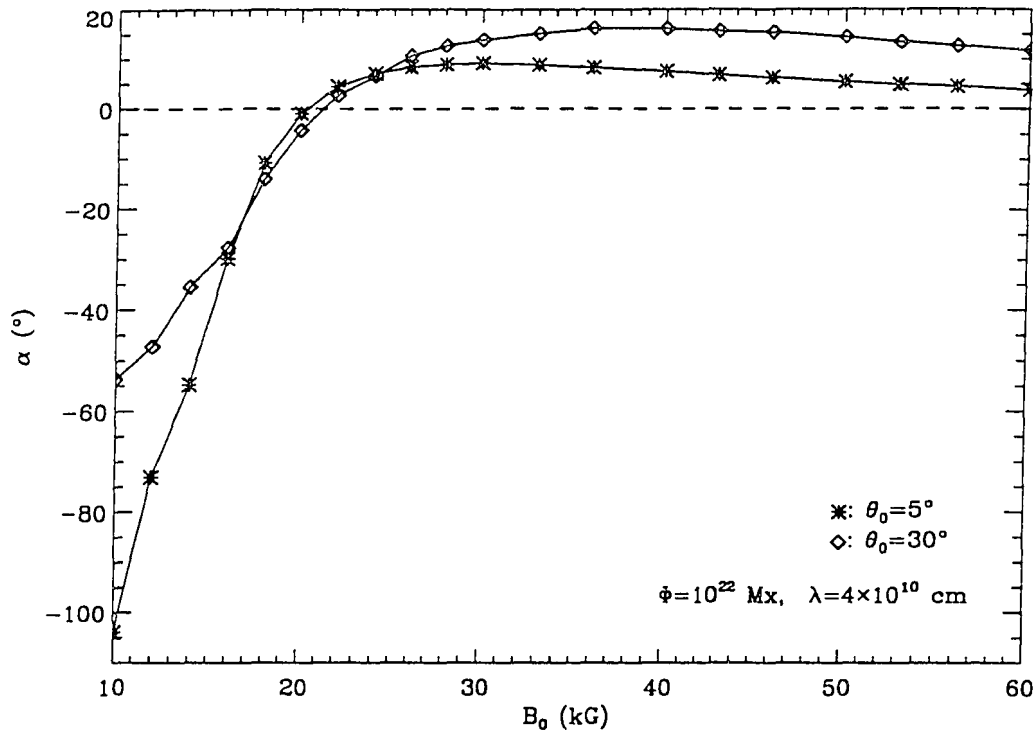


Figure 3.14 The variation of tilt angle α with field strength B_0 , showing that as B_0 drops below 30 kG, α begins to decrease sharply with decreasing B_0 , and when $B \leq 20$ kG, α becomes negative, i.e. loops emerge with inverse tilts.

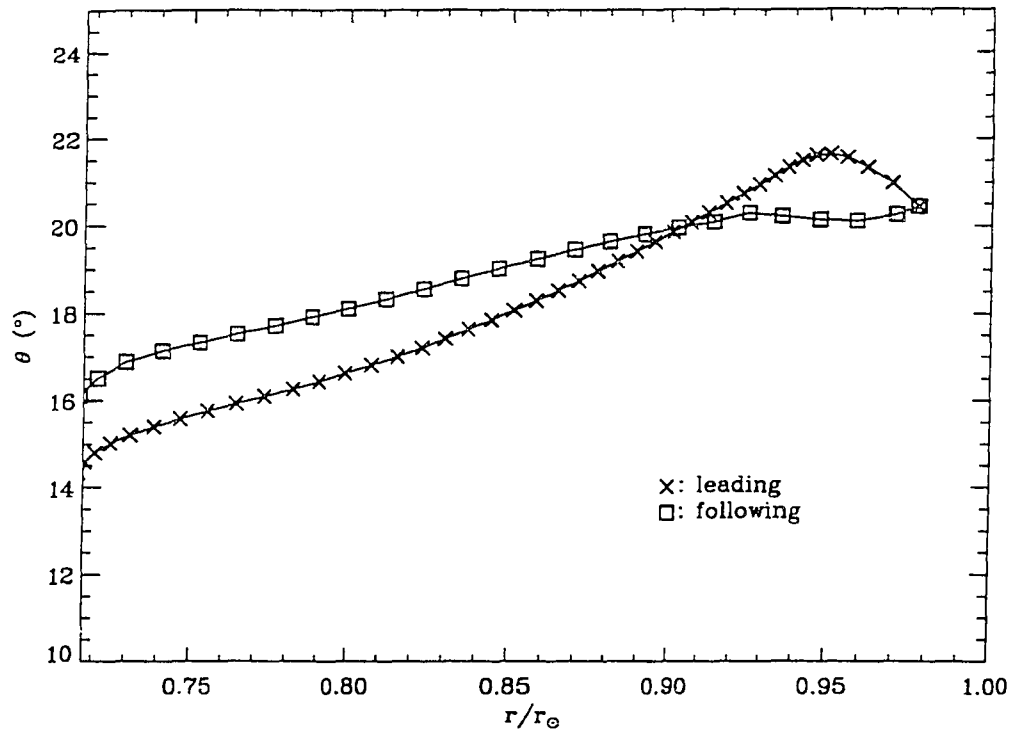
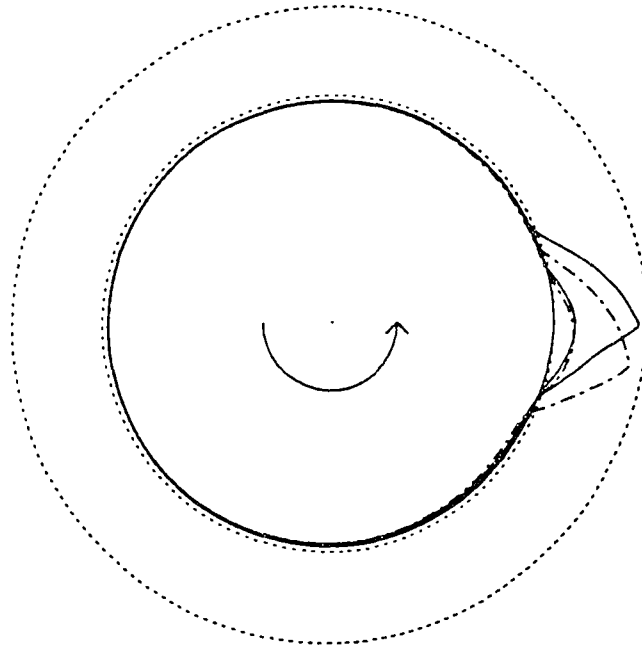


Figure 3.15 The variation of latitude with depth, along an emerging loop with initial field strength $B_0 = 10$ kG. Above a certain depth, the tilt of the loop is reversed, with the leading leg being higher in latitude than the following leg. Other initial parameters for this example are: $\Phi = 10^{22}$ Mx, $\theta_0 = 5^\circ$, and $\lambda = 3 \times 10^{10}$ cm.

Figure 3.16 The evolution of a perturbed toroidal ring assuming differential rotation (solid curves), in comparison with that assuming solid-body rotation of the Sun (dash-dotted curves). In (a) the configurations of the toroidal ring, as viewed from the north pole of the Sun, are compared at 3 consecutive instants during its evolution. In (b) the trajectories of the loop apex in the meridional plane are compared. We can see from (a) that the final emerging loop in the differential rotation case is slanted toward the direction of rotation relative to the loop in the solid-body case, and from (b) that differential rotation causes the emergence to be more radial. The initial parameters of the toroidal ring are: $B_0 = 30$ kG, $\Phi = 10^{22}$ Mx, $\theta_0 = 5^\circ$, and $\lambda = 4 \times 10^{10}$ cm. The inner and outer dotted circles mark, respectively, the base of the convection zone and the photosphere.

(a)



(b)

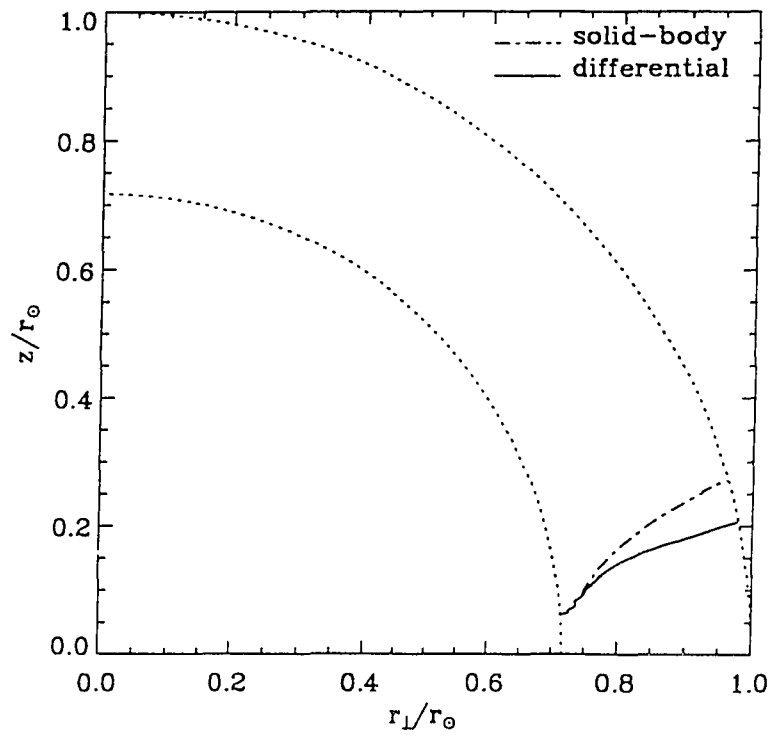


Figure 3.17 A comparison of θ_{em} obtained from simulations including differential rotation (solid lines) with those assuming solid-body rotation (dashed lines). Differential rotation reduces θ_{em} significantly in the weak field and low θ_0 ranges.

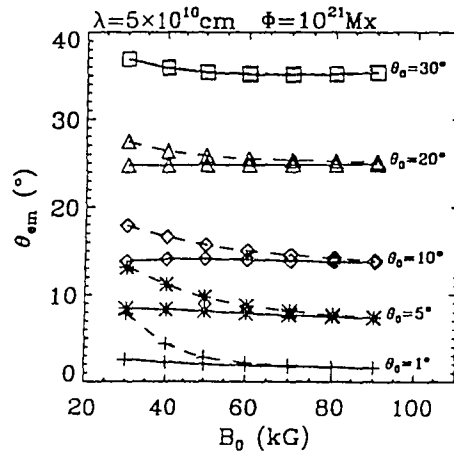
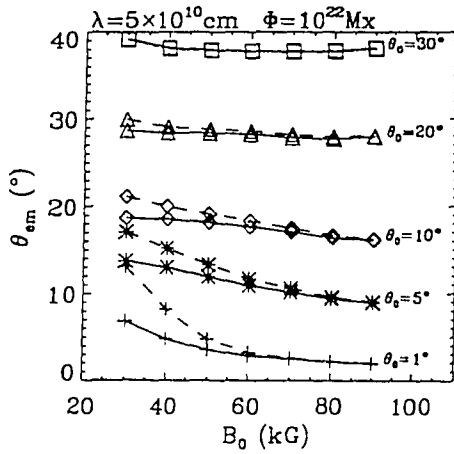
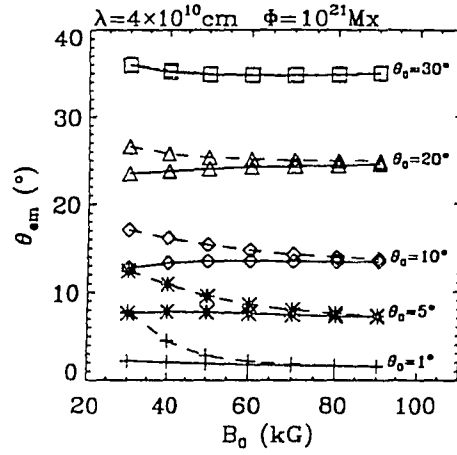
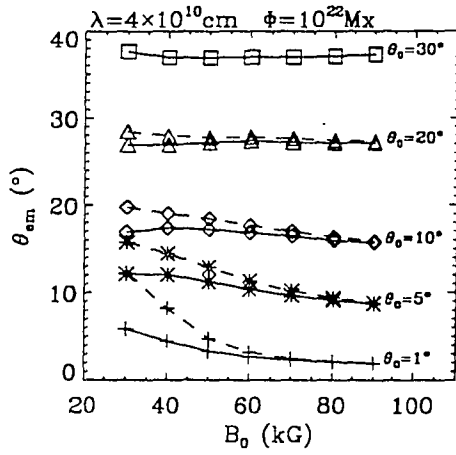
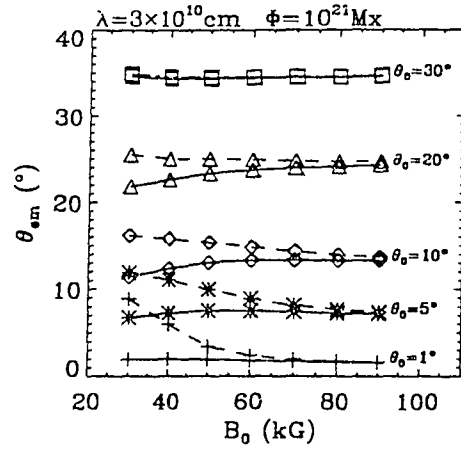
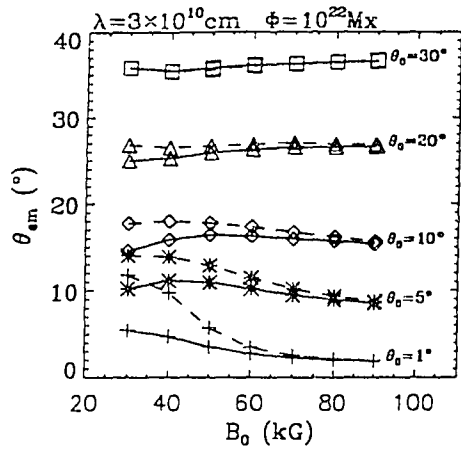
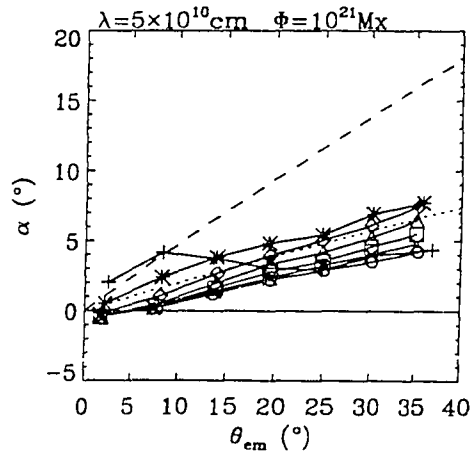
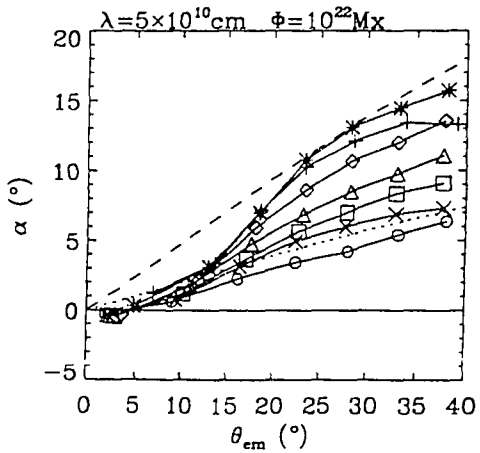
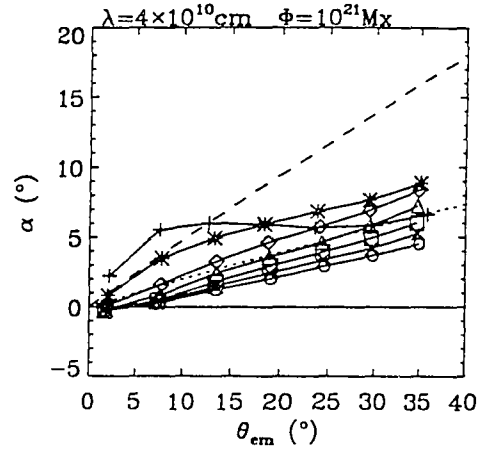
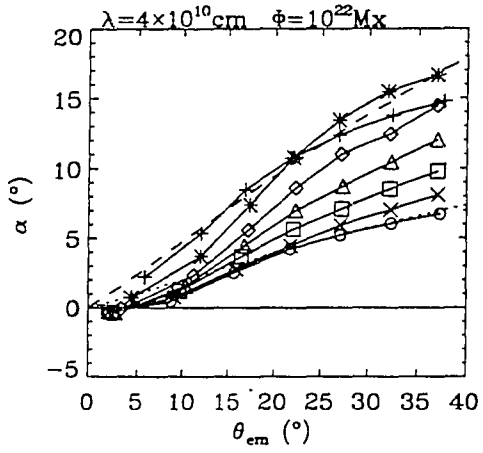
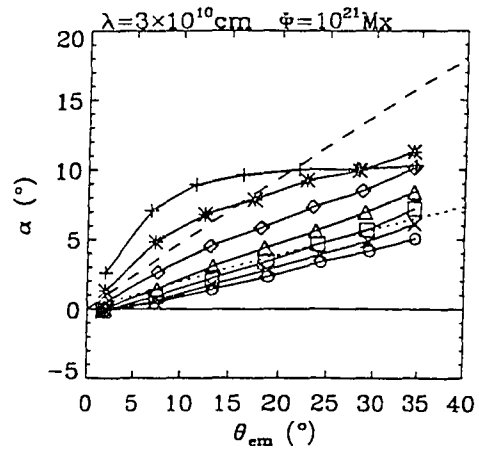
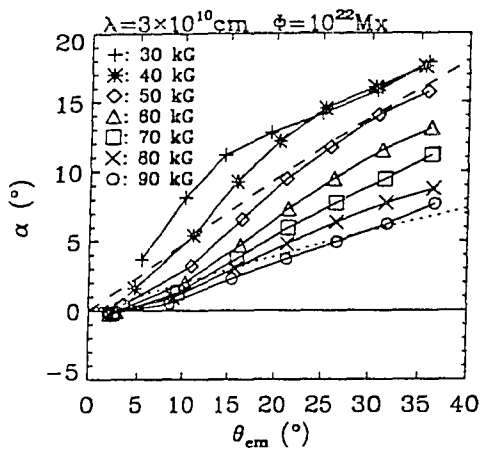


Figure 3.18 The tilt angle α as a function of emerging latitude θ_{em} , for different initial parameters B_0 , Φ , and λ , computed from simulations including differential rotation. The dashed lines correspond to $\sin \alpha = 0.48 \sin \theta_{em}$, which is the linear least square fit to the mean observed tilt angles of active regions, from Wang and Sheeley (1991). The dotted lines correspond to $\sin \alpha = 0.2 \sin \theta_{em}$, which indicates roughly the lower limit of the observed slope of tilt increase with active region latitude.



CHAPTER 4

CONCLUSIONS

Recent progress in helioseismology and in the study of the solar dynamo have revealed fundamental difficulties associated with operating the solar cycle dynamo mechanism in the bulk of the convection zone. These difficulties have led to the consensus that the dynamo responsible for the solar cycle does not operate in the bulk of the convection zone, but rather in a thin "overshoot layer" between the convection zone and the radiative interior. Thus, toroidal magnetic flux generated in the dynamo layer must traverse the entire convection zone before it can emerge to the surface to form the observed active regions. This dissertation was therefore motivated by a need to understand the process of transporting magnetic flux from the base of the convection zone to the photosphere. Based on the fundamental equations of thin flux tube dynamics derived by Spruit (1981) and Choudhuri (1989), we have developed (in Chapter 2) a numerical model to follow the dynamic evolution of a thin, closed magnetic flux tube moving in three-dimensions in the solar interior. Using this numerical model, we have performed simulations of the emergence of toroidal flux tubes in the form of loop-like structures through the solar convection zone. By analyzing the simulation results, we investigated the subsurface origins of various well-known properties of bipolar active regions and how flux tube emergence and active region formation should vary with the initial conditions of the toroidal flux tubes generated by the solar dynamo. As a result, this research has greatly improved our understanding of the roles various forces

(buoyancy, magnetic tension, aerodynamic drag, and Coriolis force) play in the dynamics of flux loop emergence and the formation of bipolar active regions.

Consistent with previous two-dimensional and three-dimensional calculations of the buoyant rise of magnetic flux loops (Moreno-Insertis 1986; Chou & Fisher 1989; Choudhuri 1989; D'Silva & Choudhuri 1993), we found that the buoyancy force can bring segments of toroidal flux tubes to the surface in the form of emerging loops in a time scale of months, provided that the length of the perturbed segment is greater than a critical value. The loop rise time is found to vary with the initial field strength and the total flux of the tube (see e.g. Figure 3.4). Knowing the time scale of active region formation (a few days from its appearance to the end of its growth), we can infer that an active region is formed through the eruption of *one* flux loop carrying the total flux of the entire region, rather than the successive eruptions of many flux loops carrying different fractions of the total flux from the base of the convection zone to the surface. If the latter were true, due to the differences in rise times among loops with different fluxes, the time scale for the formation of an active region can easily last for weeks rather than the observed time scale of a few days (e.g. Zwaan 1985).

Most importantly, our study has revealed that the Coriolis force, which results from the rotation of the Sun, is responsible for producing the well-known morphological asymmetries one sees between the leading and following polarities of an active region. Observations show that the flux of the leading polarity of an active region is mostly concentrated in large and coherent sunspots, whereas the

flux of the following polarity tends to be more dispersed and fragmented, and that the leading spots of an active region tend to be larger in area, fewer in numbers and have longer lifetimes than the following spots (Bray & Loughhead 1979, pp. 226-236). From our simulations, we have discovered (Chapter 2) that as each flux loop approaches the photosphere, the magnetic field strength of the leading leg of the emerging loop is about twice as large as that of the following leg at any chosen depth in the convection zone. This field strength asymmetry is caused by the combined action of the Coriolis force and the anchoring of the innermost portions of the loop beneath the base of the convection zone. As each loop rises due to buoyancy, the Coriolis force induces a counter-rotating flow within the loop that evacuates plasma out of the leading leg through the apex and deposits it in the following leg. This evacuation of plasma "deflates" the leading leg and results in an enhanced magnetic field strength there compared to the following leg. With a greater field strength, the leading leg of the emerging loop is less susceptible to disturbances from turbulent motions and hence, is less fragmented upon emergence. This naturally explains the origin of the more compact and longer lasting leading polarity of an active region as compared to the following.

As a possible observational test, we suggest that the counter-rotating flow of plasma from the leading leg to the following, induced by the Coriolis force as the loop rises, may be observable as an asymmetry in the vertical velocities of the two polarities of an active region early in its formation. Based on our simulations, we estimate the magnitude of the flow to be on the order of a few tenths of a

kilometers per second, and the flow should persist as long as the flux emergence is occurring.

In addition, it has been suggested (Leighton 1969; Wang & Sheeley 1991, D'Silva & Choudhuri 1993) that the Coriolis force is also the cause of the observed axial tilt angles of bipolar active regions (Hale et. al 1919, Wang & Sheeley 1989,1991; Howard 1991a,b). Similar to the findings of previous dynamic calculations (D'Silva & Choudhuri 1993), our study (Chapter 3) shows that the Coriolis force originating from the diverging east-west velocity at the top of a rising loop acts to twist the loop, producing a tilt upon emergence that is the same sense as the observed tilt angles of active regions. To quantify the tilt of emerging loops and compare it with the observed active region tilt angles, we compute the tilt angle of an emerging loop defined as the angle made by the tangent vector of the loop apex relative to the east-west direction. For physically reasonable choices of toroidal field strength $3 \times 10^4 \text{ G} \leq B_0 \leq 9 \times 10^4 \text{ G}$, the computed tilt angles of the emerging loops are consistent with the sign, the magnitude and the latitudinal variation of active region tilt angles (i.e. Joy's law, see e.g. Hale et. al [1919]). In particular, the linear least-square fit to the observed tilt angle variation with latitude obtained by Wang & Sheeley (1989,1991) is closely matched by the result of our simulations with initial toroidal field $B_0 = 5 \times 10^4 \text{ G}$ and total flux $\Phi = 10^{22} \text{ Mx}$.

From a simple force balance analysis, we have obtained a scaling law which describes the dependence of the tilt angle α on the characteristic field strength B , latitude θ , and the total flux Φ of the loop: $\alpha \propto \sin \theta B^{-5/4} \Phi^{1/4}$. This scaling law

provides a good description of the behavior of the computed tilt angles from most of our simulations. There exists some observational results (Howard 1992, 1993) which support the increase of tilt angle α with increasing Φ as predicted by the scaling relation, although there is also conflicting evidence (Howard 1991a; Wang & Sheeley 1989).

We found from our simulations that loops with initial toroidal field strength $B_0 \leq 2 \times 10^4$ G emerge with inverse tilt angles which are opposite to those of active regions, with the leading side more poleward than the following. In particular, for $B_0 \sim 1 \times 10^4$ G, the magnitude of the inverse tilt at emergence can be greater than 90° , i.e. violating Hale's polarity laws. This result suggests that the toroidal flux tubes which give rise to the great majority of active regions should have a field strength $B_0 \geq 3 \times 10^4$ G. The cause of the reversed tilt angles for weak field strength flux loops is a strong converging parallel flow that sets in at the top of the loop, in an attempt to establish hydrostatic equilibrium when the loop reaches the upper layers of the convection zone.

There has been much discussion (e.g. Choudhuri & Gilman 1987; Choudhuri 1989; Choudhuri & D'Silva 1990; D'Silva & Choudhuri 1991, 1993) about the problem of the non-radial trajectory of flux tube emergence: the Coriolis force deflects the rising flux tubes poleward and causes them to emerge at high latitudes inconsistent with the observed sunspot zones, unless the initial field strength of the tubes is very high ($\sim 10^5$ G). This dilemma was first discovered by Choudhuri & Gilman (1987) who studied the axisymmetric eruption of toroidal flux rings through

the convective envelope of the Sun. They found that as each toroidal ring begins expanding radially outward due to buoyancy, the Coriolis force, or the tendency for tube plasma to conserve angular momentum, induces a counter-rotating flow inside the ring. This counter-rotating flow then induces a Coriolis force directed inward toward the rotation axis; the θ component of this Coriolis force drives the ring to very high latitudes. In Chapter 2, we demonstrated that in the case of non-axisymmetric eruption of a toroidal ring in the form of emerging flux loops, the azimuthal (east-west) component of the drag force exerted on the loops from the ambient fluid can transfer angular momentum to the tube plasma and hence produces a more radial emergence, i.e. reduces the latitude of emergence. The more radial trajectory of emergence in the presence of the drag force has also been noted in the calculations of D'Silva & Choudhuri (1993). Furthermore, we found (in Chapter 3) that if the fraction of the total length of the toroidal ring that emerges to the surface is made smaller, the latitude of emergence is lower. Our simulations showed that the buoyant rise of a single flux loop from a toroidal ring lead to a latitude of emergence significantly lower than that of the simultaneous eruption of multiple loops from the ring, and much lower than that of the axisymmetric eruption of the entire toroidal ring. The reason is that if a smaller fraction of the toroidal ring is moving outward away from the rotation axis, angular momentum conservation will induce a weaker counter-rotating flow in the ring, and hence a weaker Coriolis force arises to drive the poleward motion of the rising loop. We found from our simulations of single emerging flux loops that the

emerging latitudes are consistent with the observed butterfly diagram, assuming a dynamo wave propagating from 30° latitude to the equator at the base of the convection zone. In the case of solid-body rotation, a toroidal field strength $B_0 \geq 6 \times 10^4$ G is required to avoid a significant equatorial gap and explain the presence of active regions within a few degrees of the equator. However, if differential rotation is included, the requirement of high field strength stated above is ameliorated and $B \geq 3 \times 10^4$ G can lead to an acceptable butterfly diagram.

The effect of solar differential rotation on the dynamics of flux loop emergence was studied in Chapter 3 by incorporating a large scale external velocity field into our numerical model. The external velocity field affects the motions of flux tubes through the drag force. We found that the final emerging loop in the case of differential rotation inclines more toward the direction of rotation than in the case of solid body rotation. In addition, for loops with initial latitude $\theta_0 \leq 30^\circ$, differential rotation causes the trajectory of emergence to be more radial, and hence results in lower emerging latitudes. Assuming a solar differential rotation profile obtained from helioseismology (e.g. Brown et. al 1989), a rising flux loop entering the convection zone from latitude $\theta_0 \leq 30^\circ$ should experience a rapid increase of rotation rate of the surrounding fluid. This increased rotation imparts an additional drag force on the rising loop in the direction of rotation, and causes the final emerging loop to slant more toward the direction of rotation. Furthermore, because of the increased drag force it experiences, the rising flux loop gains additional angular momentum and emerges at a lower latitude. Our simulations

also showed that the inclusion of differential rotation does not change the qualitative behavior of loop tilt angles, nor does it alter the result of field strength asymmetry between the leading and the following legs of an emerging flux loop. Overall, we have found that the changes induced by including differential rotation are not substantial and in most cases can be described as "small perturbations" of the results obtained assuming solid-body rotation.

In summary, this dissertation adds strong support to the current consensus of solar cycle dynamo operating in the overshoot layer, by showing that the emergence of anchored flux loops from toroidal flux tubes beneath the base of the convection zone can reproduce several important features of active regions observed at the surface, i.e. the latitude of emergence described by the butterfly diagram, the morphological asymmetry, and the tilt angles of active regions. The results of our simulations also help to constrain the toroidal field strength generated by the dynamo. It has been argued that the toroidal field must be at least 10^4 G to avoid complete distortion of rising flux tubes by convective motions and to explain the storage of flux erupted during a cycle in the overshoot layer (Zwaan 1978; van Ballegoijen 1982; Parker 1987c; Durney, DeYoung & Passot 1990). Our simulations show that the tilt angles of emerging loops only become consistent with the observed active region tilt angles described by the Joy's law when the toroidal field strength $B_0 \geq 3 \times 10^4$ G. Loops with $B_0 \leq 2 \times 10^4$ G are found to emerge with opposite tilts from those of active regions. This suggests a lower limit for the toroidal field strength of around 3×10^4 G in the dynamo layer. On the other hand,

we are less certain about the maximum field strength of the toroidal field based on our simulations. The emerging latitudes for loops with $B_0 \geq 3 \times 10^4$ G are shown to be consistent with the butterfly diagram, and the emergence becomes more radial as the field strength increases. The magnitude of the tilt angle α is shown to decrease with increasing field strength roughly as $\alpha \propto B_0^{-5/4}$, and we find it becomes too small in comparison with observations when $B_0 \sim 10^5$ G.

The numerical model used in this dissertation has incorporated several simplifying assumptions (such as the thin flux tube approximation and the adiabatic evolution of tube plasma) which limited the scope of our investigation to flux transport *within* the solar interior. At the time an active region flux tube breaks through the photosphere, these assumptions have become invalid, and we are unable to follow the subsequent formation and evolution of the active region within the framework of our simulations. Although we can infer some important characteristics of the newly formed active region based on the knowledge of the final emerging loop from our simulations, the detailed physics of active region evolution and decaying is still not understood. To study the post-emergence evolution of active region flux tubes beneath the surface, it is necessary to develop a more sophisticated dynamic model which takes into account both the flaring of tube diameter and the radiative heat loss of tube plasma near the surface.

APPENDIX A

The Numerical Algorithm

The equations of flux tube dynamics derived in Chapter 2 (eq. [2.22-2.25]) are a set of non-linear, partial differential equations (PDE's), for the dependent variables \mathbf{r} , \mathbf{v} , $\Delta\rho$, and B , which are regarded as functions of the 2 independent variables, u and t . Note that all derivatives with respect to s in equations (2.22-2.25) can be converted to derivatives in u by using the relation $\partial/\partial s = (1/L)\partial/\partial u$, where L is the total length of the tube. Since the dependent variables are given as functions of u at $t = 0$, the problem of flux tube dynamics may be formally regarded as an initial value problem.

Let the set of dependent variables $\{ \mathbf{r}, \mathbf{v}, \Delta\rho, B \} = \{ x, y, z, v_x, v_y, v_z, \Delta\rho, B \}$, be represented by the vector $\mathbf{A}(u,t)$, where each component A_k corresponds to one of the 8 dependent variables. Each of the 8 equations (2.22-2.25) (note that each vector equation has 3 components) can be schematically written in the form

$$\left. \frac{\partial A_i}{\partial t} \right|_u = f_i(A_k, \left. \frac{\partial A_k}{\partial u} \right|_t, \left. \frac{\partial^2 A_k}{\partial u^2} \right|_t; k = 1,2,\dots,8), \quad (\text{A.1})$$

for $i \in \{1,2,\dots,8\}$.

The PDE's in equation (A.1) can be discretized by assuming that each dependent variable $A_k(u,t)$ is defined on a uniform mesh of N points in u :

$$A_{k,j}(t) = A_k(u_j,t), \quad (\text{A.2})$$

where $u_j = (j - 1)/(N - 1)$, for $j = 1,2,\dots,N$. All 1st and 2nd derivatives are then replaced by the corresponding 2nd order accurate finite difference approximations:

$$\left. \frac{\partial A_{k,j}}{\partial u} \right|_t = \frac{A_{k,j+1}(t) - A_{k,j-1}(t)}{2\Delta u}, \quad (\text{A.3})$$

and

$$\left. \frac{\partial^2 A_{k,j}}{\partial u^2} \right|_t = \frac{A_{k,j+1}(t) + A_{k,j-1}(t) - 2A_{k,j}(t)}{\Delta u^2}, \quad (\text{A.4})$$

where $\Delta u = 1/(N-1)$.

Before discussing the equations themselves any further, we first digress to discuss the computation of the \mathbf{l} and \mathbf{k} vectors using the approximations (A.3-A.4).

Mathematically, because

$$\mathbf{k} \equiv \frac{\partial \mathbf{l}}{\partial s} = \frac{1}{L} \frac{\partial \mathbf{l}}{\partial u},$$

$\mathbf{k} \cdot \mathbf{l}$ must be exactly zero:

$$\mathbf{l} \cdot \frac{\partial \mathbf{l}}{\partial s} = \frac{\partial}{\partial s} \left[\frac{1}{2} \mathbf{l} \cdot \mathbf{l} \right] = 0.$$

However, because \mathbf{l}_j and \mathbf{k}_j are computed using the finite difference approximation (A.3-A.4), the inner product of the two vectors can deviate slightly from 0. If this error is not corrected, one can obtain significant Lorentz forces parallel to the flux tube, which is unphysical. Therefore, after first computing a trial value of \mathbf{k}_j using equation (A.4), we then make the correction $\mathbf{k}_j \rightarrow \mathbf{k}_j - (\mathbf{l}_j \cdot \mathbf{k}_j)\mathbf{l}_j$.

Using approximations (A.3-A.4) with the corrections noted above, equation (A.1) becomes converted to a system of $8N$ coupled first order nonlinear ordinary differential equations (ODE's).

$$\frac{\partial A_{i,j}}{\partial t} = f_{i,j}(A_{k,j-1}, A_{k,j}, A_{k,j+1}; k = 1,2,\dots,8), \quad (\text{A.5})$$

for $i \in \{1,2,\dots,8\}$, $j \in \{1,2,\dots,N\}$. The set of equations (A.5) can be solved using

any one of several standard methods (we use the 4th order Runge-Kutta method with adaptive step size control [Press et. al. 1989] with an additional Alfvén speed Courant limit.)

There is one additional modification to the standard ODE solution methods described above that we have found necessary. The left hand sides of equations (2.22-2.25) are written as time derivatives at constant u . When the equations are discretized, small high-order error terms are introduced which eventually (after several hundred time steps) cause the mesh points to drift away from their uniform spacing along the flux tube, unless some feedback or correction terms are introduced. Therefore, after each successful integration of equations (A.5), we first compute the quantity $u'_j = s'_j/L$, where L is the total length of the tube and s'_j is the length of the tube up to mesh point j from the origin mesh point. We then define $\delta u_j \equiv u'_j - u_j$, where $u_j = (j - 1)/(N - 1)$. Then all variables $A_{i,j}$ are corrected by subtracting from them the term $(\partial A_{i,j}/\partial u)\delta u_j$, where $\partial A_{i,j}/\partial u$ is computed from equation (A.3-A.4). We have found that these corrections are always very small, and that they keep the mesh points uniform to an accuracy of better than 10^{-4} .

APPENDIX B

Parallel Flow near the Loop Apex - Diverging or Converging ?

Our goal in this Appendix is to analyze the parallel flow induced in the loop as a result of tube plasma attempting to establish hydrostatic equilibrium (HE) in the parallel direction. In carrying out this analysis, we ignore the flow of plasma from the leading leg to the following leg generated by the Coriolis force. We consider only the diverging or converging flow symmetric about the apex generated by maintaining HE along the loop. We want to determine the circumstances under which the flow is diverging (i.e. a "down flow") or converging (i.e. an "up flow") at the loop apex. To this end, we start from equation (2.7) (see also Spruit 1981):

$$\frac{d}{dt} \left[\frac{B}{\rho} \right] = \frac{B}{\rho} \left[\frac{\partial v_l}{\partial s} - \mathbf{v} \cdot \mathbf{k} \right], \quad (\text{B.1})$$

which is derived from the ideal MHD induction equation and mass conservation. Here, v_l represents the parallel component of the velocity, s is arclength along the loop, ρ is the density of tube plasma and the vector $\mathbf{k} = \partial l / \partial s = \partial^2 \mathbf{r} / \partial s^2$ is the curvature vector of the tube. Based on equation (B.1), the divergence of v_l at the loop apex is:

$$\frac{\partial v_l}{\partial s} = \frac{d}{dt} \left[\ln \frac{B}{\rho} \right] - \frac{v_r}{R}, \quad (\text{B.2})$$

where v_r is the rising speed of the apex and R is the radius of curvature at the apex of the loop. Since $d/dt = v_r d/dr$ where r is the radial distance of the loop apex to the center of the Sun, equation (B.2) can be rewritten as:

$$\frac{\partial v_l}{\partial s} = v_r \frac{d}{dr} \left[\ln \frac{B}{\rho} \right] - \frac{v_r}{R} = v_r \left[\frac{1}{2p_b} \frac{dp_b}{dr} - \frac{1}{\rho} \frac{d\rho}{dr} - \frac{1}{R} \right], \quad (\text{B.3})$$

where $p_b \equiv B^2/8\pi$ is the magnetic pressure. We define $\beta \equiv P_e/p_b$, with P_e being the external pressure, then the internal gas pressure $P = (1 - 1/\beta)P_e$. Furthermore,

$$\frac{d\rho}{dr} = \frac{d\rho}{dP} \frac{dP}{dr} = \frac{1}{\gamma} \frac{\rho}{P} \frac{dP}{dr}, \quad (\text{B.4})$$

because the gas inside the tube evolves adiabatically. Here $\gamma \equiv c_p/c_v$ is the ratio of specific heats. Therefore, equation (B.3) becomes

$$\begin{aligned} \frac{\partial v_l}{\partial s} &= v_r \left\{ \frac{1}{2} \frac{\beta}{P_e} \frac{d}{dr} \left[\frac{P_e}{\beta} \right] - \frac{1}{\gamma} \frac{1}{(1 - 1/\beta)P_e} \frac{d}{dr} \left[\left[1 - \frac{1}{\beta} \right] P_e \right] - \frac{1}{R} \right\} \\ &= v_r \left\{ \left[\frac{1}{\gamma} - \frac{1}{2} \right] \frac{1}{H_p} + \left[\frac{\beta}{2} + \frac{1}{\gamma(1 - 1/\beta)} \right] \frac{d}{dr} \left[\frac{1}{\beta} \right] - \frac{1}{R} \right\}, \quad (\text{B.5}) \end{aligned}$$

where H_p is the external pressure scale height.

To maintain HE along the loop, the height variation of β must satisfy the following equation (see e.g. Chou & Fisher 1989; Fisher, Chou & McClymont 1989):

$$\frac{1}{\beta(\beta - 1)} \frac{d\beta}{dr} = - \frac{1}{H_p} \frac{\delta T/T_e}{1 - \delta T/T_e}, \quad (\text{B.6})$$

where T_e is the external temperature, T is the temperature inside the tube, and $\delta T \equiv T_e - T$. Since $\beta \gg 1$ and $|\delta T/T_e| \ll 1$ are true throughout the evolution of the rising loop, (B.6) can be simplified to

$$\frac{d}{dr} \left[\frac{1}{\beta} \right] = \frac{1}{H_p} \frac{\delta T}{T_e}. \quad (\text{B.7})$$

Substituting equation (B.7) into equation (B.5) we obtain

$$\begin{aligned}\frac{\partial v_l}{\partial s} &= \frac{v_r}{H_p} \left[\frac{1}{\gamma} - \frac{1}{2} + \left(\frac{\beta}{2} + \frac{1}{\gamma} + \frac{1}{\gamma \beta} \right) \frac{\delta T}{T_e} - \frac{H_p}{R} \right] \\ &\approx \frac{v_r}{H_p} \left[\frac{1}{\gamma} - \frac{1}{2} + \frac{\beta}{2} \frac{\delta T}{T_e} - \frac{H_p}{R} \right].\end{aligned}\quad (\text{B.8})$$

We can see that $1/\gamma - 1/2 \approx 0.1$ which is always positive. To simplify the problem, we assume that $H_p/R \ll 0.1$ and thus can be ignored (which is not always true). We then find from equation (B.8) that the flow at the apex is always diverging ($\partial v_l / \partial s > 0$), if the tube plasma is colder than the external plasma, i.e. $\delta T \equiv T_e - T > 0$. For converging parallel flow, the temperature inside the tube has to be sufficiently higher than the external temperature so that $|(\beta/2)\delta T / T_e|$ is greater than $1/\gamma - 1/2$.

In our simulations, $\delta T = 0$ initially. As the loop rises, δT becomes negative because the external temperature gradient is superadiabatic, whereas the tube plasma evolves adiabatically. In the deep convection zone, the magnitude of $(\beta/2)\delta T / T_e$ remains very close to zero because the external temperature is nearly adiabatic. Thus, $\partial v_l / \partial s$ remains positive (divergent). When the loop reaches the upper convection zone where the temperature stratification becomes significantly superadiabatic, the negative term $(\beta/2)\delta T / T_e$ becomes substantial ($|(\beta/2)\delta T / T_e| \gg 0.1$) and a strong converging parallel flow sets in. We find that $\delta T / T_e$ is essentially determined by the external stratification, while $\beta \propto B^{-2}$. Therefore, for loops with weaker field strength, the converging flow sets in earlier at greater depths and is relatively stronger.

REFERENCES

- Babcock, H. W. 1961, *Ap. J.*, **133**, 573
- Batchelor, G. K. 1967, *Fluid Dynamics* (Cambridge: Cambridge University Press),
p. 339
- Bray, R. J., & Loughhead, R. E. 1979, *Sunspots* (New York: Dover)
- Brown, T. M., Christensen-Dalsgaard, J., Dziembowski, W. A., Goode, P., Gough,
D. O., & Morrow, C. A., 1989: *Ap. J.*, **343**, 526
- Chou, D.-Y., & Fisher, G. H. 1989, *Ap. J.*, **341**, 533
- Choudhuri, A. R. 1989, *Solar Phys.*, **123**, 217
- Choudhuri, A. R., & D'Silva, S. 1990, *Astron. Astrophys.*, **239**, 326
- Choudhuri, A. R., & Gilman, P. A. 1987, *Ap. J.*, **316**, 788
- Cowling, T. G. 1981, *Ann. Rev. Astron. Astrophys.*, **19**, 115
- DeLuca, E. E., & Gilman, P. A. 1986, *Geophys. Astrophys. Fluid Dyn.*, **37**, 85
- DeLuca, E. E., & Gilman, P. A. 1991, in *Solar Interior and Atmosphere*, ed. A. N.
Cox, W. C. Livingston, & M.S. Matthews (Tucson: Univ. Arizona Press),
275
- D'Silva, S. 1992, in *The Solar Cycle*, ed. K. Harvey (ASP Conf. Ser.; San
Francisco: ASP), p. 168
- D'Silva, S., & Choudhuri, A. R. 1991, *Solar Phys.*, **136**, 201
- D'Silva, S., & Choudhuri, A. R. 1993, *Astron. Astrophys.*, **272**, 621
- Durney, B. R., DeYoung, D. S., & Passot, T. P. 1990, *Ap. J.*, **362**, 709
- Dziembowski, W. A., Goode, P. R., & Libbrecht K. G. 1989, *Ap. J.*, **337**, L53

- Fisher, G. H., Chou, D.-Y., & McClymont, A. N. 1989, in *Solar System Plasma Physics, Geophysical Monograph 54*, ed. J. H. Jr. Waite, J. L. Burch, R. L. Moore, p. 47
- Fisher, G. H., DeLuca, E. E., & Patten, B. M. 1992, in *The Solar Cycle*, ed. K. Harvey, (ASP Conf. Ser.; San Francisco: ASP), 173
- Fisher, G. H., McClymont, A. N., & Chou, D.-Y. 1991, *Ap. J.*, **374**, 766
- Galloway, D. J., & Proctor M. R. E. 1983, *Geophys. Astrophys. Fluid Dyn.*, **24**, 109
- Galloway, D. J., & Weiss, N. O. 1981, *Ap. J.*, **243**, 945
- Gilman, P. A. 1983, *Ap. J. Suppl.*, **53**, 243
- Gilman, P. A., Morrow, C. A., & DeLuca, E. E. 1989, *Ap. J.*, **338**, 528
- Glatzmaier, G. A. 1985, *Geophys. Astrophys. Fluid Dyn.*, **31**, 137
- Golub, L., Rosner, R., Vaiana, G. S., & Weiss, N. O. 1981, *Ap. J.*, **243**, 309
- Goode, P. R., Dziembowski, W. A., Korzennik, S., & Rhodes, E. J. 1991, *Ap. J.*, **367**, 649
- Hale, G. E. 1908, *Ap. J.*, **28**, 315
- Hale, G. E. 1924, *Nature*, **113**, 105
- Hale, G. E., Ellerman, F., Nicholson, S. B., & Joy, A. H. 1919, *Ap. J.*, **49**, 153
- Howard, R. F. 1991a, *Solar Phys.*, **132**, 49
- Howard, R. F. 1991b, *Solar Phys.*, **136**, 251
- Howard, R. F. 1992, *Solar Phys.*, **142**, 233
- Howard, R. F. 1993, *Solar Phys.*, **145**, 105
- Leighton, R. B. 1964, *Ap. J.*, **140**, 1547

- Leighton, R. B. 1969, *Ap. J.*, **156**, 1
- Maunder, E. W. 1922, *M. N. R. A. S.*, **82**, 534
- Meyer, F., Schmidt, H. U. & Weiss, N. O. 1977, *M. N. R. A. S.*, **179**, 741
- Moreno-Insertis, F. 1986, *Astron. Astrophys.*, **166**, 291
- Moreno-Insertis, F. 1992, in *Sunspots: Theory and Observations*, eds. J. H. Thomas and N. O. Weiss (Netherlands: Kluwer Academic Publishers), 385.
- Nordlund, Å., Brandenburg, A., Jennings, R. L., Rieutord, M., Ruokolainen, J., Stein, R. F., & Tuominen, I. 1992, *Ap. J.*, **392**, 647
- Parker, E. N. 1955, *Ap. J.*, **122**, 293
- Parker, E. N. 1975, *Ap. J.*, **198**, 205
- Parker, E. N. 1978, *Ap. J.*, **221**, 368
- Parker, E. N. 1979a, *Cosmical Magnetic Fields* (Oxford: Clarendon Press)
- Parker, E. N. 1979b, *Ap. J.*, **230**, 914
- Parker, E. N. 1984, *Ap. J.*, **283**, 343
- Parker, E. N. 1987a, *Ap. J.*, **312**, 868
- Parker, E. N. 1987b, *Ap. J.*, **321**, 984
- Parker, E. N. 1987c, *Solar Phys.*, **110**, 11
- Petrovay, K., Brown, J. C., van Driel-Gesztelyi, L., Fletcher, L., Marik, M., & Stewart, G. 1990, *Solar Phys.*, **127**, 51
- Press, W. H., Flannery, B. P., Teukolsky, S. A., & Vetterling, W. T. 1989, *Numerical Recipes* (Cambridge: Cambridge University Press), p. 554

- Priest, E. R. 1982, *Solar Magnetohydrodynamics*, (Dordrecht: D. Reidel Publishing Company)
- Roberts, P. H. & Stix, M. 1971, *The turbulent dynamo, a translation of a series of papers by M. Steenbeck, F. Krause, & K. H. Rädler*, NCAR-TN/IA-60
- Rosner, R. 1980, in *Cool Stars, Stellar Systems, and the Sun*, ed, A. K. Dupree (SAO Report No. 389), 79
- Schmitt, J. H. M. M. & Rosner, R. 1983, *Ap. J.*, **265**, 901
- Spiegel, E. A., & Weiss, N. O. 1980, *Nature*, **287**, 616
- Spruit, H. C. 1974, *Solar Phys.*, **34**, 277
- Spruit, H. C. 1979, *Solar Phys.*, **61**, 363
- Spruit, H. C. 1981, *Astron. Astrophys.*, **98**, 155
- Spruit, H. C., & van Ballegooijen, A. A. 1982a, *Astron. Astrophys.*, **106**, 58
- Spruit, H. C., & van Ballegooijen, A. A. 1982b, *Astron. Astrophys.*, **113**, 350
- Stenflo, J. O. 1989, *Astron. Astrophys. Rev.*, **1**, 3
- Stix, M. 1981, *Solar Phys.*, **74**, 79
- van Ballegooijen, A. A. 1982, *Astron. Astrophys.*, **113**, 99
- van Driel-Gesztelyi, L. & Petrovay, K. 1990, *Solar Phys.*, **126**, 285
- Wang, Y.-M. & Sheeley, N. R. 1989, *Solar Phys.*, **124**, 81
- Wang, Y.-M. & Sheeley, N. R. 1991, *Ap. J.*, **375**, 761
- Zwaan, C. 1978, *Solar Phys.*, **60**, 213
- Zwaan, C. 1985, *Solar Phys.*, **100**, 397
- Zwaan, C. 1987, *Ann. Rev. Astron. Astrophys.*, **25**, 83